DOCTORAATSPROEFSCHRIFT

2012 | Faculteit Wetenschappen

Macroscopic & nanoscale charge transport in poly(3-alkylthiophene)s: from single nanofiber to semi-crystalline thin films

Proefschrift voorgelegd tot het behalen van de graad van
Doctor in de Wetenschappen, Fysica, te verdedigen door:

Jean-Christophe BOLSÉE

Promotor: prof. dr. Jean Manca
Copromotor: prof. dr. Milos Nesladek

D/2012/2451/4

universiteit hasselt

Chairman	Prof. dr. Marc D'Olieslaeger, UHasselt
Promotor	Prof. dr. Jean Manca, UHasselt
Copromotor	Prof. dr. Milos Nesladek, UHasselt-IMEC
Members of the jury	Prof. dr. Ellen Moons, Karlstads Universitet (Sweden)
	Prof. dr. Wilfried Vandervorst, KULeuven-IMEC
	Prof. dr. Dirk Vanderzande, UHasselt
	Dr. Wibren D. Oosterbaan, UHasselt
	Dr. Olivier Douhéret, Materia Nova-Université de Mons

Nederlandse samenvatting

Tegenwoordig is elektronica gebaseerd op silicium. De componenten (diodes, transistors, zonnecellen) zijn van hoge kwaliteit maar helaas zijn ze heel duur. Dit komt door de hoge materiaalkosten van de silicium-wafers en de hoge productiekosten (gebruik van hoge temperatuurstappen voor oxidatie en een cleanroom).

Organische halfgeleiders bieden de mogelijkheid om de materiaalkosten te verlagen. Bovendien zijn zij oplosbaar in verschillende solventen. Dat betekent dat deze materialen kunnen aangebracht worden met goedkope printtechnieken. Daarenboven zijn polymeren plooibaar waardoor ze op verschillende gevormde oppervlakten aangebracht kunnen worden. Sinds enkele jaren bestaan er commerciële toepassingen in het veld van displays gebaseerd op organische lampen (zogenaamde OLEDs). Ook binnen het domein van organische zonnecellen gaat het snel vooruit: efficiënties van om en nabij de 10% zijn al realiteit. Al die toepassingen horen bij wat men noemt “organische elektronica”.

Om het rendement van organische toepassingen te verhogen, is het belangrijk om te begrijpen hoe ze werken. Een cruciale eigenschap van organische halfgeleiders is de elektrische mobiliteit. Deze parameter beschrijft hoe gemakkelijk het is voor een elektron (of een gat) om te bewegen binnen een materiaal wanneer daarover een elektrisch veld is gezet. Natuurlijk geldt hierbij, hoe groter de mobiliteit, hoe beter het polymeer. De doelstelling van deze thesis is de studie van elektrische transporteigenschappen (m.a.w. de mobiliteit) voor de geconjugeerde polymeren uit de klasse van de poly(3-alkylthiofen)en (P3*A*T) met poly(3-hexylthiofeen) (P3HT) als bekendste exponent. In deze thesis wordt de mobiliteit onderzocht op twee verschillende lengteschalen: 1/ macroscopische studie op dunne filmen met behulp van veldeffecttransistors en 2/ nanoschaal elektrische karakterisatie op nanovezels, uitgevoerd met behulp van een atomaire kracht microscoop (AFM).

In hoofdstuk 1 worden de kristalstructuur en morfologische eigenschappen van de nanovezels uitvoerig uitgelegd. Veldeffecttransistors als techniek om de mobiliteit van een materiaal te bepalen worden besproken in hoofdstuk 2. Belangrijke effecten zoals de trapping van elektronen en gaten komen eveneens aan bod. Deze methoden worden gebruikt in de rest van de thesis om de elektrische transporteigenschappen te bestuderen. Meer bepaald in hoofdstuk 3, waar wordt aangetoond dat de moleculaire oriëntatie aan het halfgeleider/diëlektricum grensvlak een cruciale rol speelt. Daarna wordt de mobiliteit bij lage temperaturen onderzocht om een beter inzicht te krijgen in het transportmechanisme (hoofdstuk 4). Gebruikmakende van een transportmodel (bekend als “Mobility Edge model”) worden de materiaaleigenschappen van dunne films bepaald. Tot zover het macroscopische deel van de studie.

Het nanoschaal deel van de thesis begint met een volledige beschrijving van de home-made glovebox gebouwd rond de AFM. De glovebox was noodzakelijke om metingen te doen onder een inerte atmosfeer (concentratie van zuurstof kleiner dan 50 ppm en concentratie van vochtigheid kleiner dan 10

ppm). Met de AFM kunnen we de potentiaal en de stroom op nanoschaal bestuderen. Kelvin Probe Force Microscopy (KPFM) biedt de mogelijkheid om lokaal de oppervlaktepotentiaal te meten. Een volledige beschrijving van de techniek is gegeven in hoofdstuk 6, gevolgd door enkele metingen op teststalen. De bedoeling met KPFM was om de elektrische potentiaal op geïsoleerd nanovezels te bestuderen wanneer ze geplaatst zijn in a FET-structuur. Door een lage laterale ruimtelijke resolutie (ongeveer 100 nm) was het onmogelijk om kwantitatieve resultaten te hebben.

Conductive AFM (CAFM) (hoofdstuk 7) maakt gebruik van een aangelegd voltage tussen tip en staal om vervolgens de lokale verschillen in stroom te meten. Hierdoor kan men simultaan topografie en elektrische eigenschappen meten. Met behulp van CAFM werd de mobiliteit op individuele nanovezels gemeten: longitudinale mobiliteit langs de lengte van de nanovezels en transversale mobiliteit langs de diameter van de nanovezels. Bovendien werd een veldeffecttransistor gebouwd met behulp van CAFM, waarmee de elektrische weerstand van intersectiepunten van twee nanovezels gemeten kon worden. Hierbij kwam men tot de conclusie dat deze weerstand verwaarloosbaar is.

Metingen gedaan op macro- en nanoschaal worden samengebracht in hoofdstuk 8. Enkele kwalitatieve transportmodellen worden voorgesteld: voor ladingstransport door een geïsoleerde nanovezel, door een netwerk van nanovezels en door een dunne film van nanovezels. Tevens worden de parameters besproken die de mobiliteit in organische dunne films beïnvloeden.

Synopsis

Actuellement, l'immense majorité des composants électroniques (diodes, transistors, cellules solaires …) comportent des semi-conducteurs inorganiques tel que le silicium. Ces matériaux sont hyper-performants mais nécessitent des procédés de fabrication extrêmement couteux (oxydation à très haute température, chambres propres, ultra basse pression).

Par contre, certains polymères, appelés « polymères conjugués », présentent l'intéressante propriété d'être des conducteurs électriques. Ces semi-conducteurs organiques sont nettement moins performants que leurs équivalents inorganiques mais offrent des avantages indiscutables : faible coût de fabrication et de traitement, légèreté et flexibilité. En conséquence, depuis plusieurs années, ils ont été commercialisés sous les formes suivantes : cellules photovoltaïque, lampes (OLEDs) et circuits logiques à base de transistors. C'est ce qu'on appelle l' « électronique organique » ou « électronique plastique ».

Une des propriétés physiques caractérisant les semi-conducteurs, qu'ils soient organiques ou inorganiques, est la mobilité électrique, μ. Ce paramètre décrit la facilité avec laquelle une charge électrique (un électron) est capable de se mouvoir à l'intérieur du polymère lorsqu'un champ électrique y est appliqué. Plus la mobilité est importante, plus le matériau est performant. L'objet de la thèse est l'étude de la mobilité dans l'une des familles de polymères les plus prometteuses, les poly(3-alkylthiophene). L'originalité du travail réside dans notre approche à double échelle: d'une part, la mobilité est étudiée pour des couches minces macroscopiques et, d'autre part, un microscope à force atomique est utilisé pour l'étude sur des fibres nanométriques.

Publications

As first author:

- **The importance of bridging points for charge transport in webs of conjugated polymer nanofibers** Jean-Christophe Bolsée, Wibren D. Oosterbaan, Laurence Lutsen, Dirk Vanderzande and Jean Manca, *Advanced Functional Materials*, ACCEPTED, 2011, 10.1002/adfm.201102078

- **CAFM on conjugated polymer nanofibers: Capable of assessing one fiber mobility** Jean-Christophe Bolsée, Wibren D. Oosterbaan, Laurence Lutsen, Dirk Vanderzande and Jean Manca, *Organic Electronics*, **2011**, 12, 2084-2089

- **Effects of hole and electron trapping on organic field-effect transistor transfer characteristic** Jean-Christophe Bolsée and Jean Manca, *Synthetic Metals*, **2011**, 161, 789-793

- **Microstructure charge transport relationship at different length scales in polythiophene transistors** Jean-Christophe Bolsée, Wibren D. Oosterbaan and Jean Manca, To be submitted to *Applied Physics Letters*

As co-author:

- **Alkyl-Chain-Length-Independent Hole Mobility via Morphological Control with Poly(3-alkylthiophene) Nanofibers** Wibren D. Oosterbaan, Jean-Christophe Bolsée, Abay Gadisa, Veerle Vrindts, Sabine Bertho, Jan D'Haen, Thomas Cleij, Laurence Lutsen, Christopher R. McNeill, Lars Thomsen, Jean Manca and Dirk Vanderzande, *Advanced Functional Materials*, **2010**, 20, 792-802

- **Opto-electrical and morphological characterization of water soluble conjugated polymers for eco-friendly hybrid solar cells** Gopala Krishna V.V. Thalluri, Jean-Christophe Bolsée, Abay Gadisa, Mikhail Parchine, Tine Boonen, Jan D'Haen, Ayse E. Boyukbayram, Joke Vandenbergh, Thomas J. Cleij, Laurence Lutsen, Dirk Vanderzande and Jean Manca, *Solar Energy Materials & Solar Cells*, **2011**, 95, 12, 3262-3268

- **Poly(3-alkylthiophene) nanofibers for photovoltaic energy conversion** Sabine Bertho, Wibren D. Oosterbaan, Veerle Vrindts, Jean-Christophe Bolsée, Fortunato Piersimoni, Donato Spoltore, Jan D'Haen, Laurence Lutsen, Dirk Vanderzande and Jean Manca, *Advanced Materials Research*, **2011**, Vol. 324, pp32-37

- **Effect of Alkyl Side-Chain Length on Photovoltaic Properties of Poly(3-alkylthiophene)/PCBM Bulk Heterojunctions** Abay Gadisa, Wibren D. Oosterbaan, Koen Vandewal, Jean-Christophe Bolsée, Sabine Bertho, Jan D'Haen, Laurence Lutsen, Dirk Vanderzande and Jean Manca, *Advanced Functional Materials*, **2009**, 19, 3300-3306

- **Thickness dependent residual stress in sputtered AlN thin films** Paulius Pobedinskas, Jean-Christophe Bolsée, Wim Dexters, Bart Ruttens, Vincent Mortet, Jan D'Haen, Jean Manca and Ken Haenen, *Journal of Applied Physics*, Submitted

- **On the relation between morphology and FET mobility of poly(3-alkylthiophene)s at the polymer-SiO_2 and polymer-air interface,** Wibren D. Oosterbaan, Jean-Christophe Bolsée, Linjun Wang, Veerle Vrindts, Laurence Lusten, Vincent Lemaur, David Beljonne, Christopher R. McNeill, Lars Thomsen, Jean Manca and Dirk Vanderzande, To be submitted

Brown coloured publications are discussed in the thesis.

Conference contributions

ORAL PRESENTATIONS

- **Electrical characterization of conjugated polymer nanofibers using SPM techniques** Jean-Christophe Bolsée, Wibren D. Oosterbaan, Laurence Lutsen, Dirk Vanderzande and Jean Manca , Seminar at Materia Nova, University of Mons, Belgium, 3 October **2011**.

- **Macroscopic & Nanoscale charge transport investigation on P3*A*T: from semi-crystalline film to single nanofiber** Jean-Christophe Bolsée, Wibren D. Oosterbaan, Laurence Lutsen, Dirk Vanderzande and Jean Manca,E-MRS spring meeting, **2011**, Nice, France, May 9th-13th

- **Influence of solvents on the performance of regioregular poly(3-butylthiophene) field-effect transistors** Jean-Christophe Bolsée, Abay Gadisa, Wibren D. Oosterbaan, Sabine Bertho, Veerle Vrindts, Jan D'Haen, Laurence Lutsen, Dirk Vanderzande and Jean Manca, 6th International Conference on Organic Electronics (ICOE), **2009**, Liverpool, UK, June 15th-17th

POSTER PRESENTATION

- **High dynamic range C-AFM measurements on organic photovoltaic blends** Jean-Christophe Bolsée, Abay Gadisa, Olivier Douhéret and Jean Manca, Veeco Conference, Seeing at the nanoscale VI, exploring the future of nanotechnology using SPM and related techniques, International conference, **2008**, Berlin, Germany, July 9th -11th

Conference Proceedings:

- **The use of nanofibers of P3HT in bulk heterojunction solar cells: the effect of order and morphology on the performance of P3HT:PCBM blends.**
  Dirk Vanderzande, Wibren D. Oosterbaan, Veerle Vrindts, Sabine Bertho, Jean-Christophe Bolsée, Abay Gadisa, Koen Vandewal, Jean Manca, Laurence Lutsen, Thomas Cleij, Jan D'Haen, Jun Zhao, Guy Van Assche & Bruno Van Mele In: Kafafi, Zakya H. & Lane, Paul A. (Ed.) **2009** Proc. SPIE: vol. 7416. p. 741605

Writing a book is an adventure. To begin with, it is a toy and an amusement; then it becomes a mistress, and then it becomes a master, and then a tyrant. The last phase is that just as you are about to be reconciled to your servitude, you kill the monster, and fling him out to the public.
- Sir Winston Churchill -

Chapter I Introduction: Conjugated polymers for organic electronics

1.1. Motivation and goal of the thesis

1.1.1. Organic electronics: historical perspective

Our modern digital life is based on solid state electronic devices which include solar cells, transistors, light-emitting diodes, memory devices, integrated circuits, microprocessors and so on. The electronic revolution started in 1947 when Bardeen, Brattain and Shockley invented the bipolar transistor[1] (Nobel prize in physics in 1956). A major breakthrough was the development of the integrated circuit in the late 50's by Kilby (common Nobel prize in Physics with Alferov and Kroemer in 2000, almost 40 years after the discovery!).The original inorganic semiconductor to fabricate diodes and transistors was germanium (Ge) but it was soon replaced by silicon (Si)[2]. The nowadays supremacy of Si compared to others inorganic semiconductors is explained by its excellent stability at high temperature and the perfect interface formed with its native oxide, SiO_2. However, the silicon technology requires ultimate processing conditions (thermal oxidation occurs at a temperature of about 1000°C) which make it very expensive and opens the way for other cost reducing technologies.

Most of organic materials are perfect electrical insulators as we have been taught and experienced since ever. Nevertheless, a category of them, known as conjugated polymers, exhibit interesting electrical properties. Due to chemical doping (oxido-reduction), their conductivity can be increased by several orders of magnitude. Organic semiconductors have been studied since the 1960s. But because of a poor chemical stability, it is only in 1977 that a major breakthrough was realized by Heeger, MacDiarmid and Shirakawa (Nobel prize in Chemistry 2000)[3]. They discovered that the electrical conductivity of polyacetylene increases by 8 orders of magnitude from 10^{-5} S cm^{-1} (undoped state) to 10^{3} S cm when doped with reducing or oxidizing agents. In the 1980s, another major discovery was that the conjugated polymer like poly(p-phenylene vinylene) (PPV) exhibited electroluminescence[4]. Since, much effort was put on the solubility of conjugated polymers in common organic solvents like chloroform and chlorobenzene.

1.1.2. Advantages and applications of organic electronics

The advantages of organic semiconductors with respect to their more usual inorganic counterparts are multiple. Low material costs, low processing costs (no high vacuum or high temperature steps or cleanroom facilities), lightweight and flexibility are indisputable arguments which guarantee a promising future. Moreover, the fact that they can be directly processed from solutions opens the road for facile

and large scale film production units. All these reasons demonstrate that organic semiconductors are candidates for flexible, low-cost and lightweight electronic applications such as: solar cells, organic field-effect transistors (OFETs), vapour sensors and organic light emitting diodes (OLEDs) for lighting and displays.

In 2010, the total market ($2.1 Billion) of printed electronics was largely dominated by OLEDs and photovoltaics, see Figure 1- 1A. The forecasts predict a total market of $56 Billion for 2020, still dominated by OLEDs and solar cells. From a scientific point of view, the publication of peer-reviewed articles has been permanently increasing for more than 20 years as seen on Figure 1- 1B. These are arguments indicating that organic electronics and printable electronics are promising technologies.

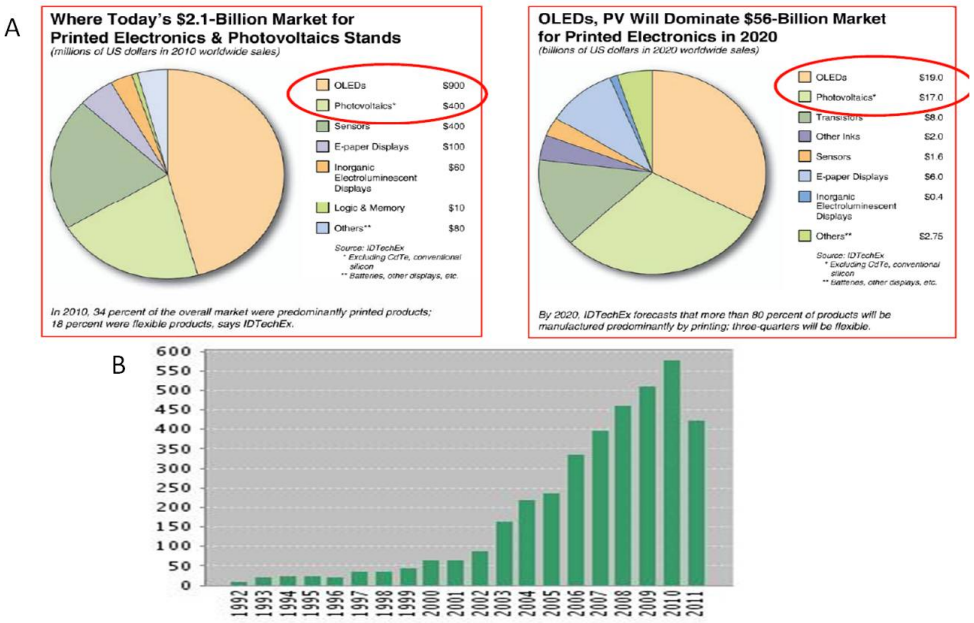

Figure 1- 1 A: Percentage of organic electronic market in 2010 and forecast for 2020, source: IDTechEX [2011]. B: Number of scientific publications per year related to "organic electronics", source: Web of Knowledge [October 2011].

1.1.3. Goal of the thesis

A key parameter influencing strongly the performance of all devices (solar cells, transistors, organic LEDs) is the easiness with which an electric charge (hole or electron) can be transported by an electric field through the polymer. Physicists quantify this material property by the charge carrier mobility, μ. The aim of this work is to explore charge transport (in term of performance, mechanism and influencing morphological factors) in poly(3-alkylthiophene)s (P3*A*T)s, a family of conjugated polymers which is frequently used as model system. We will investigate charge transport for two kinds of P3*A*T layers:

those obtained from nanofiber dispersions (model system 1) and those obtained from molecularly dissolved solution (model system 2). We will see that both systems have their own advantages and that the comparison of the two systems will allow us to conclude on which morphological factors influence in-plane charge transport in P3*A*Ts layers. Another key point of this thesis lies in the fact that we will perform a multi length scales study: a nanoscale approach on one isolated nanofiber and a macroscopic approach on semi-crystalline thin films. Considering isolated nanofibers as nanoscopic basic building blocks of macroscopic thin films, we will propose qualitative models for charge transport in organic field-effect transistors.

1.1.4. Structure of the thesis

After having presented the advantages and applications of organic electronic, **chapter I** details the goal and structure of the thesis. Then, a short theoretical background on conduction and charge transport in conjugated polymers is given. This is followed by the description of poly(3-alkylthiophene)s (P3*A*T)s, the conjugated polymers studied in this work. Finally, we present the synthesis, morphological characterization of the P3*A*T nanofibers and the motivations for using them.

Macroscopic approach (chapters II to IV):

Throughout this thesis, organic field-effect transistors (OFETs) will be used to extract information on the charge transport properties. **Chapter II** details the device structure, working principle and fitting methods for obtaining the field-effect mobility, μ. Then, in a second part of the chapter, we will focus on the undesired effects of holes and electrons traps which occur when OFETs are operated. We conclude by giving some guidelines to reduce these detrimental effects.

Chapter III presents the main OFETs results obtained on poly(3-alkylthiophene) layers. Two kinds of samples will be investigated: those obtained from nanofiber dispersions (in the form of webs and films) (model system 1) and those obtained from molecularly dissolved solution (model system 2). Using different dielectric surfaces and changing the length of the alkyl side chain, we will find that the two kinds of samples have a completely different behavior. In another section, the crucial impact of molecular orientation at the dielectric interface on charge transport will be proved.

Low temperature charge transport measurements will be discussed in **chapter IV**. These investigations are essential to have an insight on charge transport mechanisms. The results will be analyzed in the framework of the mobility edge model. Parameters such as the total concentration of trap states, width of trap states distribution and mobility in the band states will be extracted for different samples.

Nanoscale approach (chapters V to VII):

Two electrical characterization techniques at the nanoscale will be used: Conductive AFM (CAFM) and Kelvin Probe Force Microscopy (KPFM). The first measures the current at the nanoscale while the second measures the surface voltage. **Chapter V** describes the equipment necessary to perform these nanoscopic measurements in a controlled environment. In particular, we describe in detail the glovebox which was constructed around the AFM during the first part of the thesis.

Chapter VI will focus on KPFM. This technique is used to measure the surface voltage at the nanoscale. The working principle and technique limitations (namely its poor lateral resolution) will be discussed thoroughly. Then, several test samples will be used to demonstrate the technique capabilities. Finally, much time and energy will be paid for measuring the voltage profile along isolated nanofibers when they are deposited in OFETs substrates.

Chapter VII details the measurements performed with Conductive AFM (CAFM). The description and characterization of a field-effect transistor where one of the electrodes is the mobile CAFM tip will be given. The CAFM-transistor allows resolving the current distribution within a web of nanofibers. Moreover, hole mobility along two different axis in one single nanofiber is studied. Charge carrier anisotropy by four orders of magnitude will be demonstrated.

Charge transport model (chapter VIII):

Macroscopic and nanoscale charge transport results acquired through the thesis are collected in **chapter VIII** where we propose a few transport models in the different samples obtained from the nanofiber dispersion. We will also discuss the different parameters influencing the in-plane charge transport in P3*A*Ts layers.

Finally, **chapter IX** gives a summary and an outlook of the thesis.

1.2. Origin of electrical conduction in conjugated polymer

In this section, we will give a short theoretical introduction about conjugated polymers and explain how and why electrons can move over the polymer (for more information on organic chemistry see reference 5).

The main constituent of a conjugated polymer is the carbon atom. In its ground state, a carbon atom has the following configuration: $1s^2 2s^2 2p^2$ where the last four electrons participate to the chemical bonds with neighbouring electrons. To increase the overlap between orbitals, and hence increase the stability, the s and p orbitals will hybridize either in sp, sp^2 or sp^3 orbitals depending on the closest atoms. For instance, methane (CH_4) is formed of $4sp^3$ orbitals (1s electron is promoted to the p state and combined with the 2p electrons and 1s electron to form $4sp^3$ orbitals) disposed in a tetrahedral structure for symmetry reasons. For ethylene (C_2H_4), each atom is composed of $3sp^2$orbitals (given by the hybridization of 1s orbital and 2p orbitals, lying in the sample plane at 120° from each other) and an unhybridized p orbital. These two p orbitals in C_2H_4 overlap laterally and give rise to the π bond while the 3 sp^2orbitals form 3 σ bonds (2 with hydrogen atoms and 1 with neighbouring carbon). In summary, a double carbon bond is formed of 1 σ bond and 1 π bond. σ bonds are much stronger than π bonds because the overlap surface is higher. Moreover, σ bonds allow rotation of one atom with respect to the other around their axis while π bonds do not.

Conjugated polymers are characterized by alternating single and double carbon bonds along the backbone, Figure 1- 2. Double carbon bonds are formed of 1 σ bond and 1 π bond while a single one is

formed of 1 σ bond. It results in a π electron delocalized over a large part of the molecules. This delocalization is responsible for conduction mechanism within the polymer.

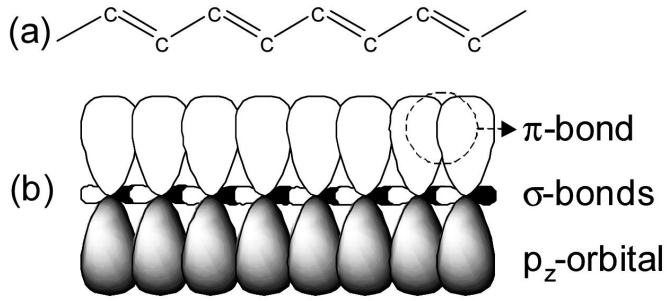

Figure 1- 2 (a) Molecular structure of polyacetylene, the simplest conjugated polymer, for clarity H atoms are not represented. (b) Electronic bonds: π electrons are delocalized along the polymer chain.

Now, we explain the reason for the semiconducting properties of conjugated polymers. Molecular orbitals (MO)s are formed from combination of atomic orbitals (AO)s seen as electron waves. Two AOs can interfere constructively (σ or π bonding MO or low energy levels) or interfere destructively (σ^* or π^* antibonding MO or high energy level). The rule is that the number of MOs is equal to the sum of AO. Of course, in the ground state, electrons first fill the lowest possible energy levels. This is very similar to what happens in inorganic semiconductor, as the number of interactions increase in the system, there are more and more energy levels leading to the ultimate case where bands are formed. Figure 1- 3 shows the effect of the conjugation length on the energy levels. That is why conjugated polymers exhibit semiconductor properties. The valence band (VB) is formed by all the filled π MO while the empty π^* MO constitutes the conduction band (CB).

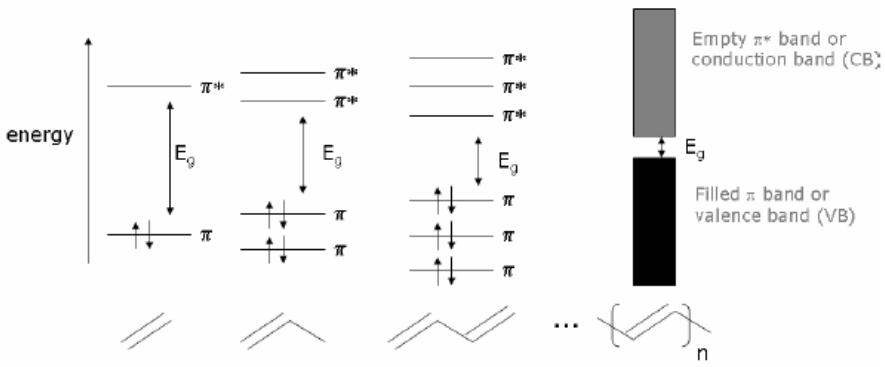

Figure 1- 3 Split of energy levels in the MO and evolution with the conjugation length. Only π orbitals are depicted.

It is common in organic electronic to define the HOMO (highest occupied molecular orbital) level as the upper limit of the VB and the LUMO (lowest unoccupied molecular orbital) level as the lower limit of the CB. The energy difference gives the energy band gap as confirmed by the Peierls distortion.

1.3. Charge carrier transport

This section describes some established charge transport models for conjugated polymers. The physical parameter to describe transport of charge carriers (holes and electrons) in any material is the mobility μ defined by $v = \mu . E$ with *v* being the speed of the charge when an electric field E is applied. The mobility says how quickly a charge can move through a material. As it will be explained below, for organic semiconductors, the mobility is function of the temperature, electric field and charge carrier concentration n in the material: $\mu(E, T, n)$.

1.3.1. Hopping transport

A classic view to describe transport in conjugated polymers is to distinguish transport along a conjugated segment or polymer chain (intramolecular transport) and transport between polymer chains (intermolecular transport). Very high mobility values (600 $cm^2\ V^{-1}\ s^{-1}$) have been measured for the intramolecular transport[6] in a ladder-type poly(p-phenylenes) because the electric charge is delocalized along the π conjugated segment. Unfortunately, the π conjugated segments are broken by structural defects (chain kinks, chain twists, chain disruptions …) or chemical defects leading to a length scale of the π conjugated segments of about 5 nm, see Figure 1- 4 (a). All these separated polymer chains are bounded by weak van der Waals forces which induces disorder. Therefore, the intramolecular transport (along one polymer chain) is orders of magnitude faster than the intermolecular transport which is the mobility that will be measured through this thesis.

Due to the high disorder, there is no two distinct band transports clearly separated by a bandgap (like for Si) but instead there are two narrow energy distributions centered on the LUMO and HOMO levels, Figure 1- 4. The shape of the energy distributions is assumed to be Gaussian as this is the case for the optical spectra[7]. Both Gaussian distributions are composed of charge transport sites which correspond to the polymer chains, see Figure 1- 4 (b). Due to the high disorder, charge carrier transport (electrons in LUMO and holes in HOMO) is a hopping process between charge transport sites being energetically or spatially separated, see Figure 1- 4 (c). Hopping has been described by Conwell [8] and Mott[9] as a phonon-assisted tunneling mechanism from site to site (reminder: a phonon is a thermally activated lattice vibration).

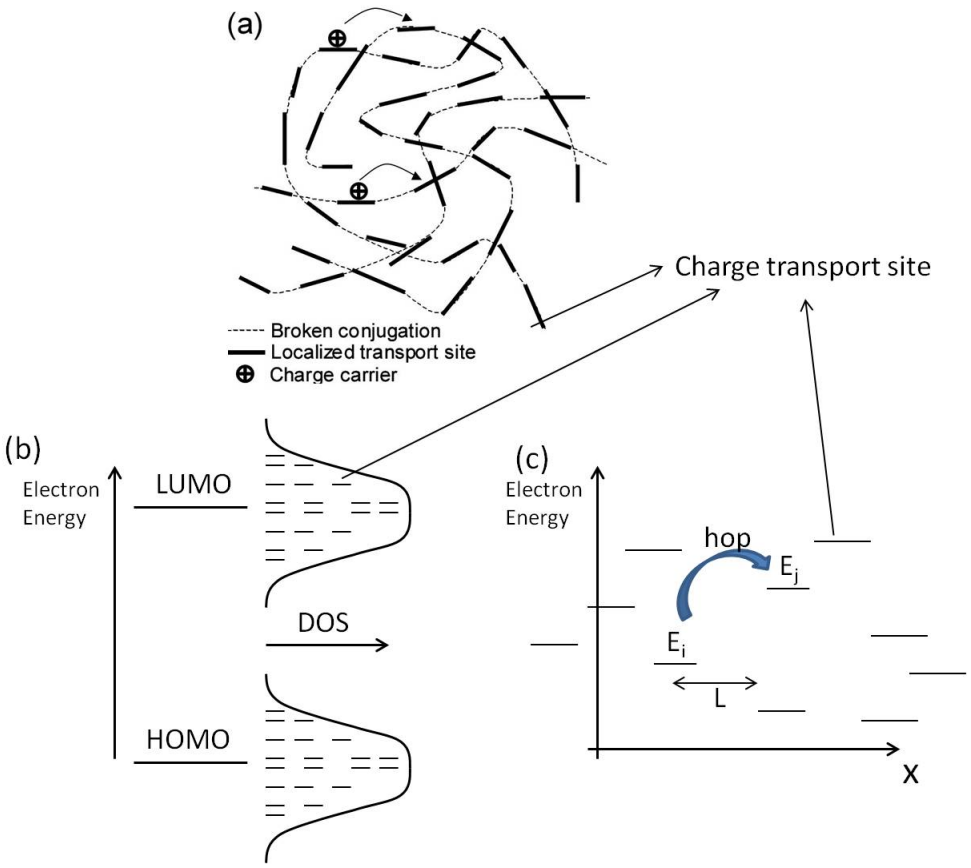

Figure 1- 4 (a) Polymer chains broken in π conjugated segments modeled as charge transport sites. (b) (electron energy-DOS space): For disordered materials, HOMO and LUMO are Gaussian distributions of localized energy levels. (c) (electron energy-x space): Hopping from energy level E_i to energy level E_j, separated by distance L, is phonon assisted. For all three pictures, the bars represent a π conjugated segment or charge transport site.

Miller and Abrahams[10]have modeled the transition rate ν_{ij} between an occupied site E_i and an unoccupied site E_j separated by a distance L. A first factor influencing the transition rate is the tunneling factor $\exp(-2\gamma L)$ with γ^{-1} the localization length, the second factor has a Boltzmann form $\exp(-\Delta E/k_B T)$:

$$\nu_{ij} \propto \exp(-2\gamma L) \begin{cases} \exp\left(-\frac{E_i - E_j}{k_B T}\right) & E_i < E_j, \\ 1 & E_i > E_j \end{cases}$$

Using this expression for the transition rate, many models[7,11] have been proposed to model charge transport in disordered organic semiconductors[12]. For instance, Mott[13,14] explained that if the energy difference between site i and adjacent site j is high enough, it can be more favorable for the charge to

hop over a longer distance. This concept is named variable range hopping (VRH). Finally, we note that Vissenberg and Matters[15] have developed a very successful model based on VRH and percolation for field-effect transistors using an exponential distribution of localized states.

Quantitatively, all the models predict that the mobility is proportional to the electric field (the so called Poole-Frenkel dependence): $\mu \propto \exp\left(\sqrt{E/E_0}\right)$ and that the mobility is thermally activated (because by nature phonon-assisted hopping is a thermally activated process): $\mu \propto \exp\left(-E_a/k_B T\right)$. Furthermore, it has been proven experimentally that the mobility is proportional to the concentration of charge carrier n in the polymer: $\mu \propto (n)^{\alpha}$. The first injected charges in the polymer occupy the electronic states in the tail of the Gaussian DOS. When the charge concentration is increased then the charges fill progressively the DOS towards the DOS center where more states are available than in the tail which means that less activation energy is required for hopping. Therefore, μ increases as n is increased.

1.3.2. Mobility edge model

The mobility edge (ME) model[16,17] is also reported as the multiple trapping and release (MTR) model[18] in the literature. This model applies for semi-crystalline polymers (hence for poly(3-hexylthiophene) (P3HT) which is a member of the P3*A*T family but does not apply for PPVs) which are composed of ordered crystalline domains surrounded by amorphous grain boundaries. The ME model stipulates that in the crystallites the charge carriers can move in delocalized bands whereas in the amorphous matrix they are trapped in localized states. The beauty of the ME model lies in the simple mobility distribution: the mobility of charge carriers is constant in the delocalized bands while this is zero in the trapped states (evident since they are trapped). Concerning the temperature dependence of the mobility: the trapped charges can be thermally activated from a localized state to a transport state (in this case the band) leading to an increasing mobility with increasing temperature: $\partial\mu/\partial T > 0$.

More quantitative information on the ME model can be found in chapter IV where temperature dependent FET measurements are discussed.

1.3.3. Comparison with inorganic semiconductor

To further clarify the charge transport mechanisms in organic semiconductors, comparison with the inorganic counterpart, for which transport theory is much more established, can be worthwhile. In Table 1, we compile and compare some charge transport parameters. For inorganic semiconductor, we have, of course, chosen Si while for organic semiconductors we have chosen the amorphous PPV and the popular semi-crystalline P3HT. PPV is more disordered and exhibits hopping transport in a Gaussian distribution while semi-crystalline P3HT is better explained by the ME model. It explains the orders of magnitude difference between the reported mobilities in the table.

Due to long range order and strong inter-atoms bonding, the charge carrier transport in inorganic semiconductors is described by a band theory where the electrons wave functions are delocalized all over the crystal. It gives a rather simple charge transport picture where, in contrast to conjugated polymers, the charge carrier mobility is not dependent on the electric field E nor on the charge carrier

concentration n (see section 1.3.1.). And, as expected, the charge carrier mobility for holes and for electrons is many orders of magnitude higher than for PPV and P3HT. Looking at the effect of temperature is also informative. For Si, carriers moving through the crystal are scattered by lattice vibration resulting from the temperature. If T increases, the frequency of scattering events will increase and therefore μ decreases. For PPV and P3HT, this is exactly the opposite which occurs: temperature stimulates hopping between localized states and therefore μ is getting higher with temperature.

	Organic semiconductors		Inorganic semiconductors[19]
Example	PPV Amorphous	P3HT Semi-crystalline	Si
Bonding force	Weak van der Waals intermolecular forces		Strong covalent bond
Charge transport type	Hopping transport between localized states	Band transport in delocalized states (see ME model)	Band transport in delocalized states
DOS shape	Gaussian	expon. in the gap unknown in the band (see ME model)	$\propto \sqrt{E}$
Origin of n/p type	Intrinsic		Doping
ε_r	3		11.8
μ_n [cm^2 V^{-1} s^{-1}][20]	$10^{-4} - 10^{-3}$	~ 0.1	1350
μ_p [cm^2 V^{-1} s^{-1}][20]	$10^{-4} - 10^{-3}$	~ 0.1	480
T dependence on μ	$\mu \propto \exp\left(-{E_a}/{k_B T}\right)$ $\rightarrow {\partial\mu}/{\partial T} > 0$		$\mu \propto T^{-3/2}$ [21] $\rightarrow {\partial\mu}/{\partial T} < 0$
E dependence on μ	$\mu \propto \exp\left(\sqrt{{E}/{E_0}}\right)$		No
n dependence on μ	$\mu \propto (n)^{\alpha}$		No[21]

Table 1 Comparison of charge transport salient points for organic and inorganic semiconductors.

1.4. Conjugated polymer nanofibers

1.4.1. Motivation for P3*A*T nanofibers

In the field of organic electronics, regioregular poly(3-alkylthiophene)s (P3*A*T)s are among the most intensively studied conjugated polymers. The chemical structure of P3*A*T is depicted in Figure 1- 5. The *A* denotes the number of carbon atoms in the *n*-alkyl side chain (*n* stands for "normal" and means that the chains are straight). For instance, P34T means 4 carbon atoms in the side chain and P35T 5 atoms. In this thesis, the number of C atoms in the alkyl side chain will vary from 4 to 9.

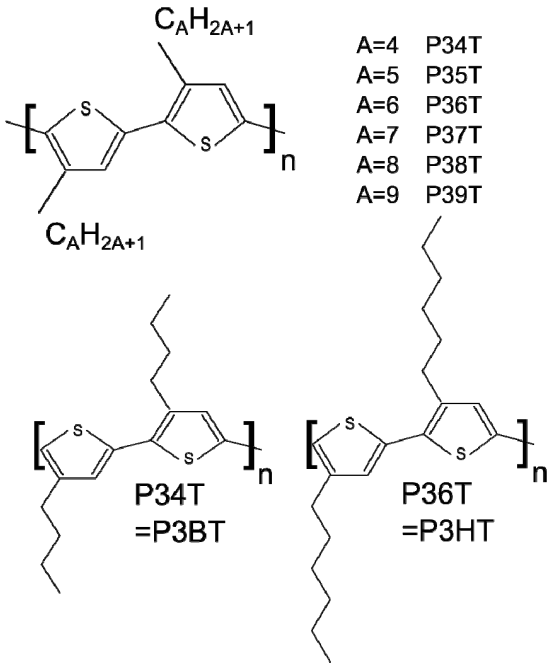

Figure 1- 5 Chemical structure of P3*A*Ts.

By far, the best known representative of P3*A*T is P36T, interchangeably called P3HT (for poly(3-hexylthiophene)). The reasons for this intense interest are that: (i) P3HT offers a good solubility in most common organic solvents which requires long alkyl side chains; (ii) P3HT has a large overlap between π orbitals delocalized along the polymer chain; (iii) P3HT has a strong tendency to crystallize in a fibrillar shape. In spite of this fact, more attention in this work has been given to P34T, interchangeably called P3BT (for poly(3-butylthiophene)). The reason is that the deposition of well-defined isolated nanofibers was much easier in the case of P3BT than for any others P3*A*Ts.

In the literature, many methods to induce P3HT crystallization into nanofibers have been reported. Fast drying deposition process, like spin-coating, has proven to produce semi-crystalline P3HT films

[22]. However, a general approach to promote crystallization is to slow down the drying speed: by using slow deposition techniques[23] (like drop casting, dip-coating), by diluting the polymers in high boiling point solvents[24] or by covering the samples with a Petri dish in order to decrease the drying speed. Another approach is to apply treatments on the dried solid film: film annealing[25] (referred to as "thermal annealing") and film exposition to solvent vapour[26] (referred to as "solvent vapour annealing") are known techniques to reorganize polymer chains into the desired nanofibrillar crystal. All these methods increase the time available for the molecule to self-organize into nanofibers.

However, all these conventional methods offer little control on the obtained morphology. An alternative approach is the production of the P3*A*T nanofibers directly in dispersion before film deposition as already performed in 1993[27]. As pointed out by Berson et al.[28] and Oosterbaan et al.[29], nanofiber dispersions offer several advantages with respect to the conventional techniques:

- It requires no thermal or solvent annealing steps and then offers a better control on the film morphology.
- It allows to study short alkyl side chains P3*A*T which have very low solubility.
- It allows to reach similar levels of crystallinity within the P3*A*T family and thus enables the comparison of devices performance as a function of *A*.
- Nanofiber formation in dispersion is expected to give more evolved and relaxed systems than those obtained by thermal annealing.
- Since no annealing is needed, it allows the use of plastic transparent substrates which have a glass transition temperature T_g (around 75 °C for PET (polyethylene terephtalate)) much lower than typical annealing temperature, around 120-140 °C.

1.4.2. P3*A*T nanofibers synthesis

P3*A*T nanofiber (NF) dispersions used in this work were prepared and characterized by Dr. Wibren Oosterbaan with the help of Ing. Veerle Vrindts, both from the organic chemistry group at University Hasselt[29]. In this paragraph, we present the highlights of the NFs synthesis. If needed, more details can be found in reference 29.

The starting materials are regioregular P3*A*Ts synthesized using the Rieke method, see Table 2 for regioregularities RR, polydispersity PD and number-average molecular weight M_n. Then, the different P3*A*Ts are dissolved in suitable solvents, annealed to a certain temperature, giving an orange coloured solution, and then the solution is slowly cooled down to room temperature to deliver dark red or purple NF dispersions. The choice of the appropriate solvent for each P3*A*T is the key element. A trade-off has to be found between good dissolving solvents for which almost all the polymer chains are perfectly dissolved giving no NFs and too bad dissolving solvent for which no homogeneous solution can be obtained. Reference 29 proved that the solvent refractive index is a rational factor to predict the NFs formation for a given polymer-solvent combination. Because P37T nanofibers crystallize in another crystal type[29], these NFs were not probed in this thesis.

The crucial influences of RR[22] and M_n [30,31,32] on charge transport has been established for a long time. We see in Table 2 that the variation in RR is small enough to have no influence on the charge transport results. Moreover the M_n values are all positioned in the high M_n region where the mobility is M_n independent[30,31,32]. Consequently, the investigations of chapter III will only be influenced by the length of the alkyl side chains, *A*.

A	Polymer name	Abbreviation	Solvent	M_n [kg mol^{-1}]	PD	RR [%]
4	Poly(3-butylthiophene)	P34T, P3BT	o-chlorotoluene	19.5	2.29	96.5
5	Poly(3-pentylthiophene)	P35T	p-xylene	16.7	1.93	94.5
6	Poly(3-hexylthiophene)	P36T, P3HT	p-xylene	23.7	1.80	94.5
8	Poly(3-octylthiophene)	P38T, P3OT	Pinane	28.0	1.66	97
9	Poly(3-nonylthiophene)	P39T	Pinane	25.9	1.46	98

Table 2 Nanofibers synthesis parameters. See references 29 and 33 for more details.

Polymer solution concentration ranges from 0.3 to 1 wt %. Smaller concentration would give spin coated films thinner than 20 nm, considered as insufficient for devices preparation, while higher concentration would lead to gelation and hence non uniform thin layers.

1.4.3. Nanofibers morphological characterization

NFs topography is measured with AFM in the standard tapping mode on very diluted dispersions (0.005 wt. % or less) drop cast on SiO_2. Height, amplitude and phase images on P34T, P36T and P38T are shown in Figure 1- 6. Typical NFs height is around 4 nm and NFs width (measured as the full width at half maximum, FWHM) is around 20 nm, consistent with previous reports[27,28,34]. Remarkably, no alkyl chain length dependence is observed for the height or the width, see Table 3. From a practical point of view, we have to point out that obtaining a well-defined web of P34T NFs was much easier than for other P3*A*Ts. All the depositions for P34T gave the well-defined webs while the big majority of other P3*A*Ts depositions produced junks contaminated samples or NFs clustering in agglomerates or, in the worst case, nothing. The explanation of this is still unclear.

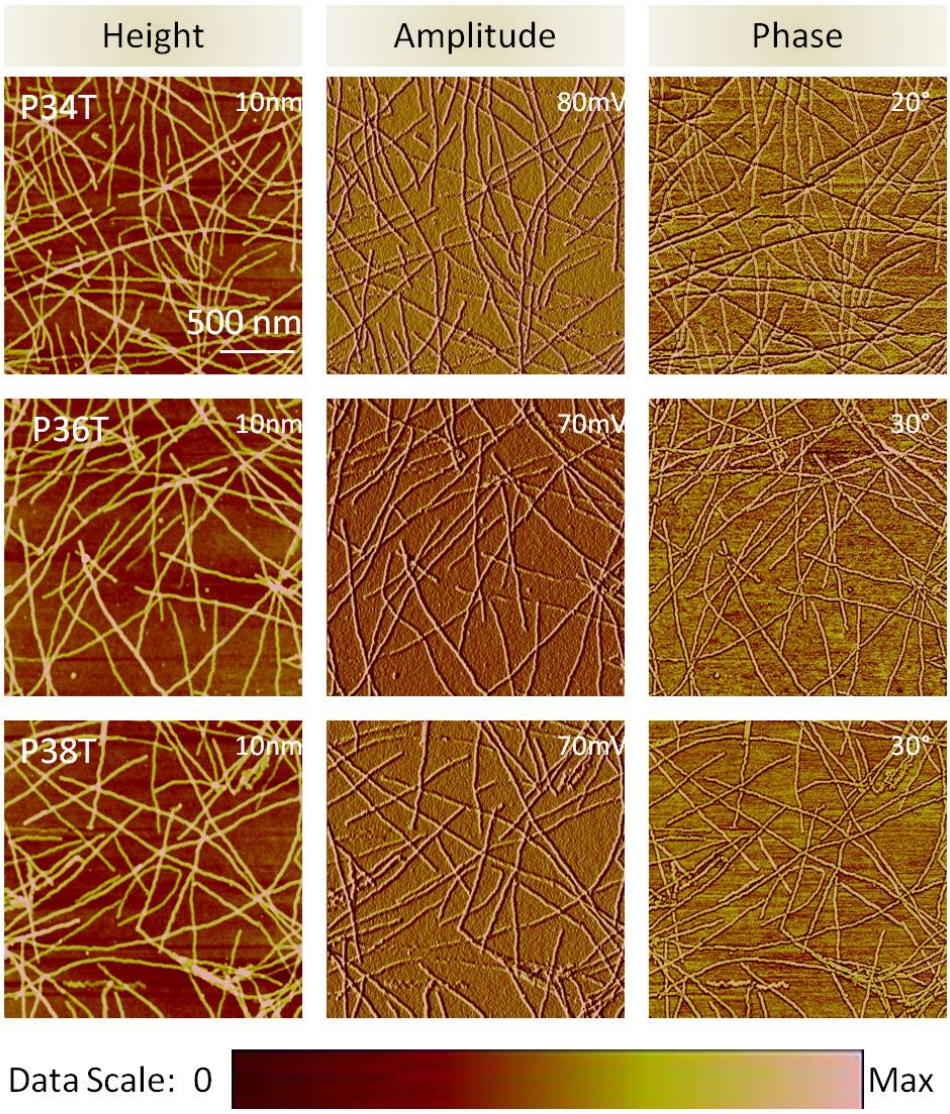

Figure 1- 6 AFM height, amplitude and phase images of P34T, P36T and P38T nanofibers.

In Figure 1- 7, we see a P34T NFs web measured at different length scales. Also, a z profile of one isolated NF is shown.

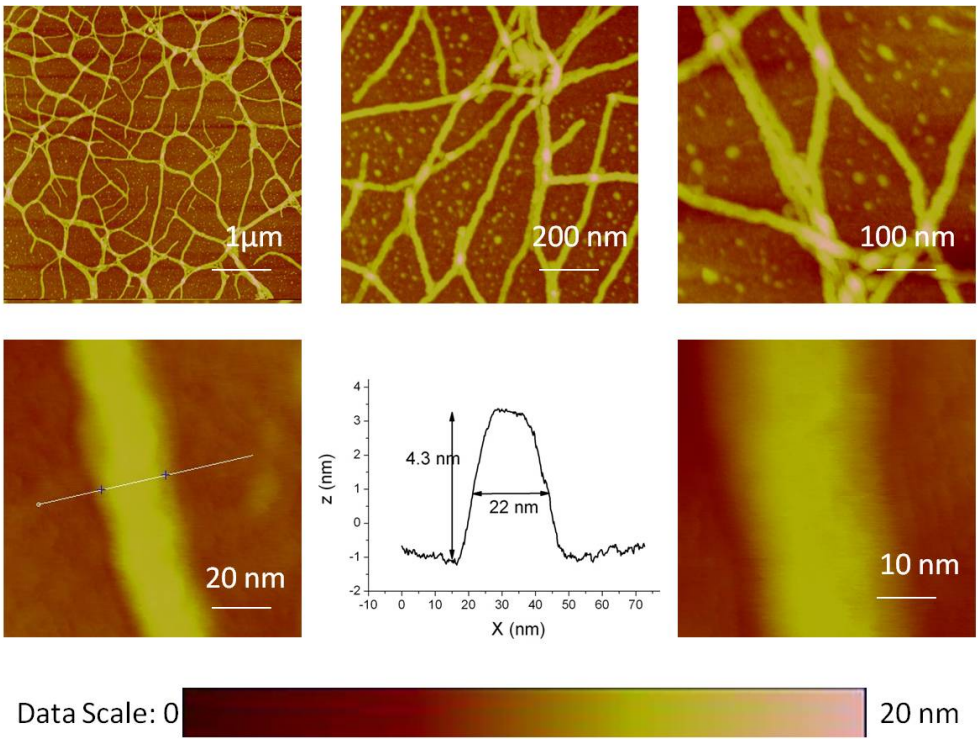

Figure 1- 7 P34T nanofibers at different length scales. High resolution maps are measured with a super sharp AFM tip.

		AFM		TEM[29]	XRD[29]	
A	Polymer	Height [nm]	Width [nm]	b [Å]	a [Å]	ξ [nm]
4	P34T	3.7 – 5	18 - 26	3.8	12.11	10.1
5	P35T	3.7 – 5	18 - 26	3.7	14.83	13.2
6	P36T	3.7 – 5	18 - 26	3.8	15.79	12.0
8	P38T	3.7 – 5	18 - 26	3.8	19.47	13.5
9	P39T	3.7 – 5	18 - 26	3.8	21.27	14.5

Table 3 Structural parameters of one nanofiber.

AFM is a fantastic technique but it remains a surface technique and if we want to get some information on the NFs internal structure, we have to go for complementary techniques like TEM, XRD and UV-Vis spectroscopy. Based on these techniques, ref. 29 and other papers[27,35] have reported the crystal structure of Figure 1- 8.

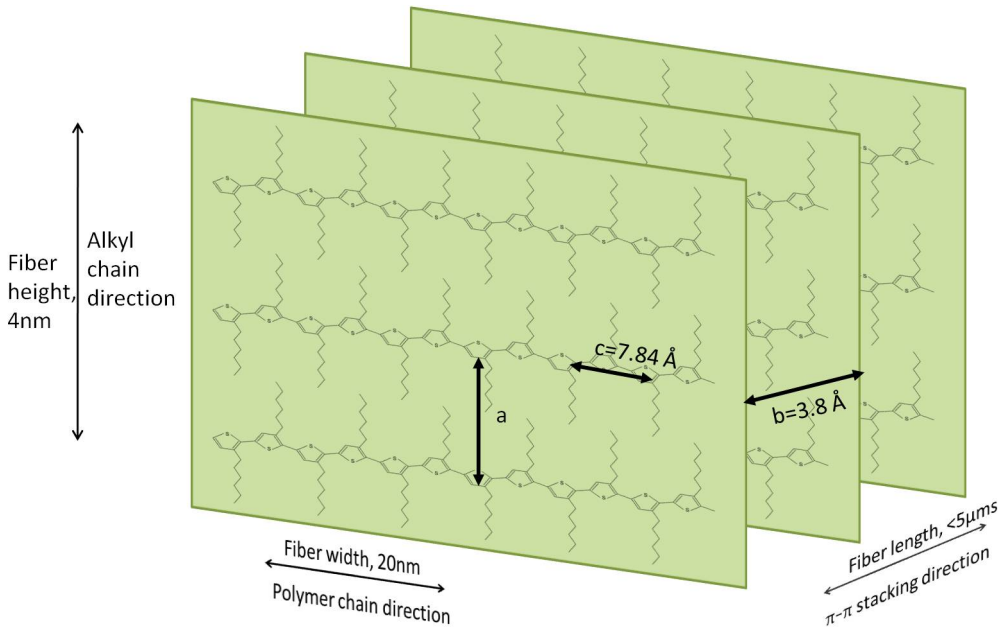

Figure 1- 8 Schematic of a P3HT (P36T) nanofiber.

The polymer chains, oriented along the c-direction, stack in lamellar sheets by $\pi - \pi$ interactions along the length of the NFs and pack laterally along the alkyl chain direction, the a-direction. Table 3 shows the lattice parameters of the NFs. Used in the $\theta - 2\theta$ mode, XRD probes the crystal planes parallel to the substrate surface and thus gives information about the a lattice parameter. A remarkable linear relation between the a values and the alkyl side chain length was found[29], see Table 3 and Figure 1- 9. The Scherrer lengths ξ which give information on the crystal size are also obtained with XRD[29]. On the other hand, when used in the diffraction mode, TEM probes the crystal planes perpendicular to the sample surface and hence the b parameter. A common $\pi - \pi$ stacking distance of about 3.8 Å is found for all P3ATs.

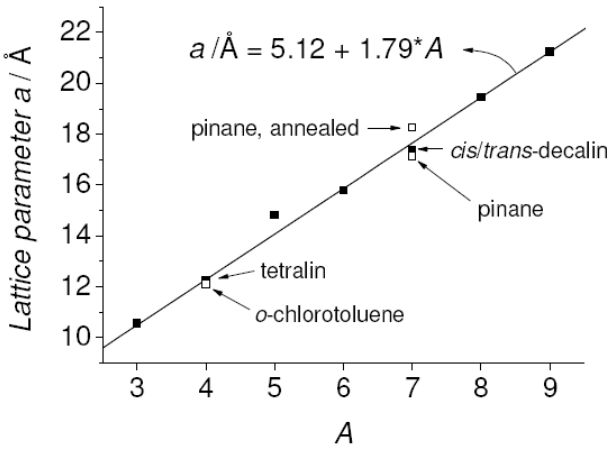

Figure 1- 9 Lattice parameter *a* for isolated NFs from XRD as a function of alkyl side chain length *A*. Reproduced from reference 29.

[1] W. Shockley, *J. Bell Syst. Techn.* **1949,** 28, 435.
[2] E. Meijer, Charge transport in disordered organic field-effect transistors, **2003**, Phd thesis, Philips Research Laboratories.
[3] C.K. Chiang et al., *Phys. Rev. Lett.* **1977**, 39, 17, 1098.
[4] J.H. Burroughes et al., *Nature* **1990,** 347, 6293, 539.
[5] J.E. McMurry, Organic chemistry, 2007, from Brooks Cole.
[6] P. Prins et al., *Phys. Rev. Lett*. **2006**, 96, 146601.
[7] H. Bässler, *Phys. Stat. Sol. (b)* **1993**, 175, 15.
[8] E.M. Conwell, *Phys. Rev*. **1956**, 103, 51.
[9] N.F. Mott, *Canadian J. Phys.* **1956**, 34, 1356.
[10] A. Miller and E. Abrahams, *Phys. Rev.* **1960**, 120, 745.
[11] S.V. Novikov et al., *Phys. Rev. Lett*. **1998**, 81, 20, 4472.
[12] M. Breselge, Electrical Characterization of 2,5-Substituted Poly(p-Phenylene Vinylene) Derivatives and Their Application in Organic Bulk Heterojunction Solar Cells, **2007**, Phd thesis, University Hasselt
[13] N.F. Mott, *J. of non Crystalline Solids*, **1968**, 1, 1, 1.
[14] N.F. Mott and E.A. Davies, Electronic Processes in non-crystalline materials, 2nd Edition, Oxford University Press, London, **1979**.
[15] M.C.J.M. Vissenberg and M. Matters, *Phys. Rev. B.* **1998**, 57, 12964.
[16] A. Salleo et al., *Phys. Rev. B* **2004**, 70, 115311.
[17] R.A. Street et al., *Phys. Rev. B* **2005**, 71, 165202.
[18] G. Horowitz et al., *J. Phys. III* **1995**, 5, 355.
[19] Ben G. Streetman and Sanjay Kumar Banerjee, Solid States Electronic Devices, 6th edition
[20] For organic: these are intermolecular values at room temperature, low electric field (0.1 MV m^{-1}) and high charge concentration obtained in FET structures (higher than 10^{19} cm^{-3}). See section 1.3.1 for intramolecular values. For inorganic: values at room temperature.
[21] Here we neglect the scattering due to impurity which is predominant at low T but can be neglected at room T.
[22] H. Sirringhaus et al., *Nature* **1999,** 40, 685-687.
[23] M. Surin et al., *J. Appl. Phys.* **2006**, 100, 033712.
[24] J.F. Chang et al., *Chem. Mater.* **2004**, 16, 4772-4776.

[25] S. Cho et al., *J. Appl. Phys.* **2006**, 100, 114503.
[26] Y. Zhao et al., *Appl. Phys. Lett.* **2007**, 90, 043504.
[27] K.J. Ihn et al., *J. Polym. Sci., Part B : Polym. Phys.* **1993**, 31, 735.
[28] S. Berson et al., *Adv. Funct. Mater.* **2007**, 17, 1377-1384.
[29] W.D. Oosterbaan et al., *J. Mater. Chem.* **2009**, 19, 5424.
[30] R.J. Kline et al., *Macromolecules* **2005**, 38, 3312.
[31] A. Zen et al., *Adv. Funct. Mater.* **2004**, 14, 757.
[32] R. Zhang et al., J. Am. Chem. Soc. **2006**, 128, 3480.
[33] W.D. Oosterbaan et al., *Adv. Funct. Mater.* **2010**, 20, 792-802.
[34] S. Samitsu et al., *Macromolecules* **2008**, 41, 8000-8010.
[35] J.A. Merlo and C.D. Frisbie, *J. Phys. Chem. B* **2004**, 108, 19169-19179.

"For their researches on semiconductors and their discovery of the transistor effect"
William Bradford Shockley, John Bardeen, Walter Houser Brattain – The Nobel prize in physics in 1956

Chapter II: Organic field-effect transistor - Method

Throughout this thesis, organic field-effect transistors (OFET)s are used to extract information on the charge transport properties of the polymer under investigation. The first half of this chapter details the device structure, working principle and fitting methods for obtaining the field-effect mobility μ. The second half focuses on the undesired effects of holes and electrons traps occurring when operating OFETs and gives some guidelines to reduce these detrimental effects.

2.1. Working principle

Beside being one of the elementary component of today's electronics, field-effect transistors (FET)s can be used to extract an important material parameter, the field-effect mobility μ. As depicted in Figure 2-1, an OFET has three electrodes: the source, the drain and the gate. It consists in applying an electric field between the source electrode (always grounded) and the drain electrode (at voltage V_D) and in measuring the drain current I_D flowing from the source to the drain while the concentration of charge carriers n can be modulated by varying the gate voltage V_G. The polymer is deposited (by spin-coating or drop-casting) on the substrate and therefore covers the channel which is the region between the source and the drain electrodes. For an overview about OFETs, see references 1, 2, 3, 4, 10.

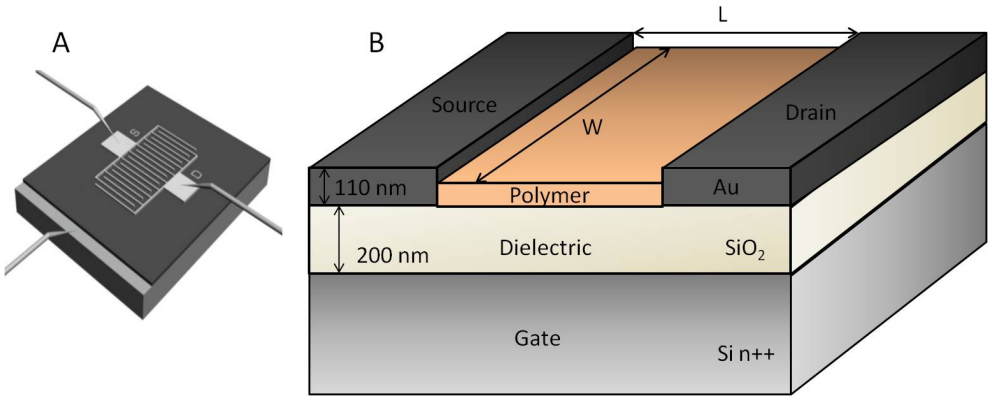

Figure 2- 1 A: Top view of the three electrodes of a FET structure contacted with the needles of a waferprober. B: OFET schematic for a bottom gate, bottom contacts configuration.

Due to the choice of the source and drain electrodes (gold on top of a titanium adhesion layer), the measurements are made in the p-mode (holes conducting). The gold work function (around 5-5.2 eV) and highest occupied molecular orbital (HOMO) levels of the P3ATs (around 5.1 eV) are very close leading to a small energy barrier for hole injection. On the other hand, electron injection in the polymer is unlikely due to the position of the lowest unoccupied molecular orbital (LUMO)((around 3 eV). The schemes of Figure 2- 2 show how the concentration of charges can be changed, how the saturation mode starts and how the transistor can be switched from the ON state to the OFF state where no current is flowing.

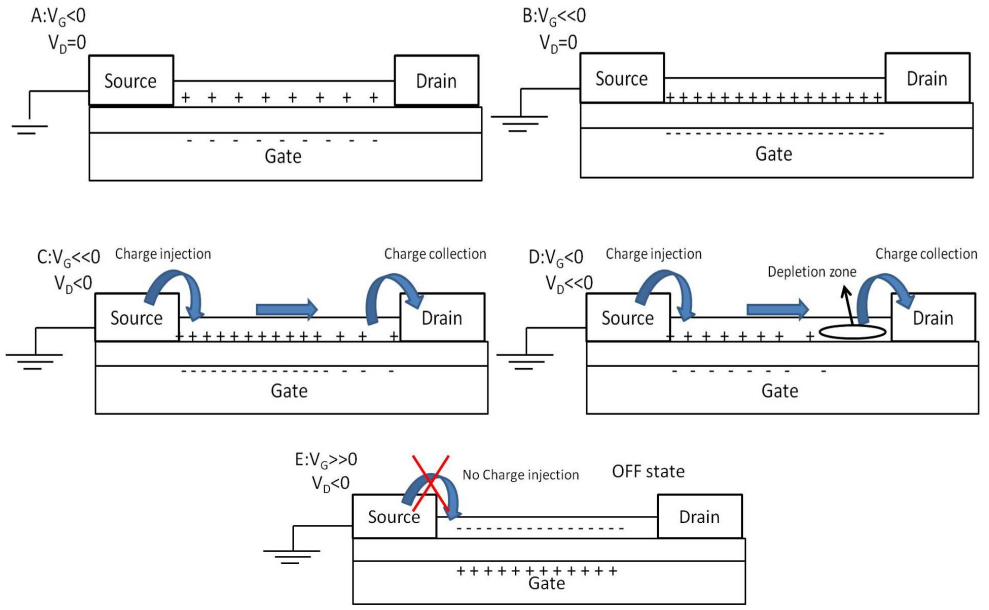

Figure 2- 2 Working principle of the OFET. A: Negative gate voltage V_G induces positive charge carriers in the polymer. B:The concentration of charge carriers can be modulated with V_G. C: When biasing the drain voltage V_D, holes are injected at the source electrode and collected at the drain. Because V_D is negative, the charge carrier concentration is not uniform but is reduced close to the drain. The current is proportional to V_D, this is the linear mode. D: At high negative V_D, a depletion zone is created at the drain size leading to an increase of the channel resistance. The current is independent on V_D, this is the saturation mode. E: For positive V_G, no electrons can be injected from the source electrode to the polymer because Au work function (5-5.2 eV) is much higher than LUMO levels of P3ATs (3 eV). No current is flowing this is the OFF state.

An output characteristic (Figure 2- 3A) is the current plot in function of V_D at different V_G. In the linear regime ($|V_G - V_T| > |V_D|$), I_D is varying linearly with V_D (meaning that the channel resistance is constant according to Ohm's law) and is varying also linearly with V_G at fixed $V_D$meaning that the channel resistance is decreasing when more charges are induced into it. This second linear relation is perfectly observed in the transfer characteristic of picture B where the slope of the curve is constant. In Figure 2- 3B, we define the onset voltage V_{onset} as the gate voltage at which conduction starts and the threshold voltage V_T as the gate voltage being the extrapolation of the linear portion of the transfer curve to zero current. In the saturation regime ($|V_G - V_T| < |V_D|$), I_D is V_D independent (meaning that the channel

resistance increases according to Ohm's law) because of the depletion zone on the drain extremity while I_D is $\propto V_G^2$ as can be seen on the transfer characteristic of picture C.

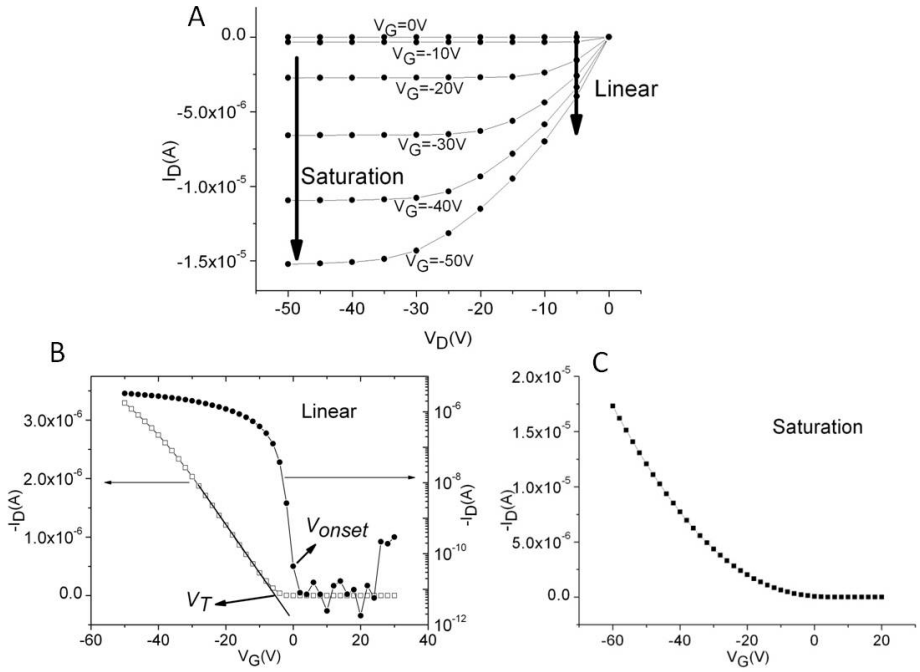

Figure 2- 3 A : OFET output characteristic of a p-type polymer in accumulation mode. B-C: transfer characteristics in the linear (V_D=-4 V) and saturation mode (V_D=-70 V) from which the mobility is extracted. On web of P34T NFs.

Quantitatively, the following standard equations which were developed for inorganic semiconductors are routinely used for organic semiconductors [5]

$$\text{Linear mode: } I_D = \frac{\mu.W.C_0}{L}.(V_D - R_C I_D).(V_G - V_T)$$

$$\text{Saturation mode: } I_D = \frac{\mu.W.C_0}{2.L}.(V_G - V_T)^2$$

Where W is the width of the channel, L its length, C_0 is the capacitance per unit area of the dielectric and R_C is the contact resistance. For an ideal transistor, V_T would be zero but, as explained in detail later in this chapter, V_T is strongly influenced by electrons and holes trapping[6]. The two equations assume that the mobility is charge carrier concentration independent (or V_G independent) which is not always the case for organic semiconductors. In this case, the gate voltage dependent mobility is extracted from the transconductance $\frac{\partial I_D}{\partial V_G}$ of the transfer curves: $\mu = \frac{L}{WC_0V_D}.\frac{\partial I_D}{\partial V_G}$ at different V_G.

Anyway, all the reported mobilities at room temperature in this thesis were gate voltage independent, except of course for the subthreshold region.

High-performance OFETs not only exhibit high mobility but must also have a high on to off ratio, a negligible contact resistance R_C and an onset voltage V_{onset} close to 0 V. Moreover, in order to operate at low voltage, the subtreshold region should be as small as possible, i.e. the threshold voltage is close to the onset voltage.

2.1.1. Technical details

OFETs substrate: Through the thesis, we use a standard bottom gate, bottom contacts OFET structure built on highly n-doped Si wafer as shown in Figure 2- 1. The capacitance per unit area C_0 of the SiO_2 dielectric is 16.9 nF cm^{-2}. A self-assembled monolayer of hexamethyldisilazane (HMDS) is used on some devices to passivate the bare SiO_2 dielectric. Using conventional photolithography, source and drain electrodes consisting of gold (100 nm) on top of a titanium adhesion layer (10 nm) were patterned. The OFETs substrates were purchased from Philips. The channel width W is 10 mm or 20 mm and the channel length L is between 10 µm and 40 µm if not otherwise specified. Prior to film deposition, the substrates were cleaned according to a standard procedure (20 min ultrasound in soap, 10 min ultrasound in acetone, 10 min in boiling isopropanol and 15 min in UV-ozone to remove the HMDS layer initially present on the dielectric of the OFETs structure.

OFETs substrate pre-annealing: Before any film deposition, the substrate is annealed in the glovebox at 120 °C for 15 min then cooled down at room temperature. The goal of this substrate pre-annealing is to outgas all the humidity captured in the hydrophilic SiO_2 during the storage and cleaning processes. This point was found to be essential. If not pre-annealed, OFETs showed no OFF state regime (proof of humidity contamination) and the only way to remove the detrimental humidity is to anneal the film which is something we do not want since it changes the film morphology and charge transport parameters and then complicates the analysis.

OFETs measurements: All OFETs measurements and sample preparations were performed under N_2 atmosphere (oxygen and humidity levels <1ppm). Measurements occurred in the dark. The current-voltage characteristics are measured using two Keithley 2400 sourcemeters, the source voltage being grounded. The leakage current through the gate dielectric is continually monitored to track any breakdown of the dielectric. Transfer characteristics consist of an off-to-on sweep (from positive to negative V_G) followed by an on-to-off sweep (from negative to positive V_G) in the linear regime. Similar results were obtained if the sweeping order was changed: first on-to-off then off-to-on sweeps. The sweep rate is 2 Vs^{-1} if not otherwise specified.

Materials: Measurements shown in the section 2.1. are performed on a web of P34T nanofibers presented in chapter I (with surface coverage lower than 20%). The nanofibers were spin-coated on the OFETs substrates at 1000 rpm for 2 min.

2.1.2. Linear versus saturation mode

As explained above, the field-effect mobility can be extracted from the transfer characteristics in the linear or in the saturation regimes. However, each technique has its own advantages and care should be taken in the choice of the mode. For samples with very low mobility (10^{-7}-10^{-8} $cm^2 V^{-1} s^{-1}$ like the water soluble conjugated polymers characterized in one of my co-authored papers, see publication section[7]) and consequently low current, the best choice is the saturation mode because the current is always higher than in the linear one and then is easier to detect. Nevertheless, for samples where the current detection is not an issue, the best choice is the linear mode. The reason is that in the linear mode the charge carrier concentration along the channel (from source to drain) is almost constant because $|V_G - V_T| > |V_D|$ whereas in the saturation mode the concentration of holes is strongly changing along the channel because $|V_G - V_T| < |V_D|$ (the difference between both modes can also be viewed in Figure 2- 2). Since for organic semiconductors, it is well established that the mobility is charge concentration dependent (especially for disordered semiconductors at low temperature, see chapter IV), it means that the saturation mode mobility is an average of mobility at different charge concentrations. Consequently, all the reported mobilities in this work were performed in the linear regime.

2.1.3. Influence of the electric field

As said in chapter I, the mobility in organic semiconductors is usually described by a Poole-Frenkel dependence, $\mu \propto \exp\left(\sqrt{E/E_0}\right)$, in other words the mobility is increased by the electric field in the direction of the motion. In the OFET structure, this electric field is $E = V_D/L$ (and not V_G related!). Since the goal of the thesis is not to investigate the influence of the electric field on charge transport, it has been decided to perform <u>all</u> the measurements at the same low electric field 0.1 MV m^{-1}. For instance, the measurements in the linear mode were made at V_D=-3 V for L=30 µm.

2.1.4. Evaluation of contact resistance, R_C

Like in all electrical measurements, care must be taken on the influence of the contact resistance R_C which includes the resistances at the source-polymer contact, at the drain-polymer contact, in the connecting cables and needles. To estimate R_C, we use the technique called transfer line method (TLM)[8] which makes benefit of the fact that the total resistance (the one which is measured) is the sum of a channel length dependent term ($R_{channel}$) and a constant term (R_C):

$$R_{tot} = R_C + R_{channel} = R_C + \frac{\rho L}{Wh}$$

Where ρ is the resistivity of the material and h the thickness of the accumulation layer. R_C is then found by plotting the $R_{tot} - L$ graph and by taking the linear extrapolation at L= 0 as this is shown in Figure 2-4

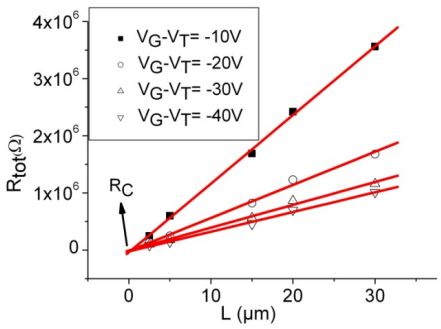

Figure 2- 4 Graphic technique used to estimate R_C. On web of P34T NFs.

The criterion we have used to decide whether the measurement is R_C limited or not is that the term $R_C.I_D$ (in linear equation above) is in the vicinity of 1% of V_D. No OFETs measurement shown in this thesis was contact limited.

2.1.5. Leakage current and transient effects

Because no dielectric is perfectly insulating, there is continuously a leakage current per unit length (noted as $J_{leak}^{channel}$) flowing through the dielectric when the OFET is biased. In addition to this first contribution, there are local leakage currents between the source and the gate I_{leak}^{source} and between the drain and the gate I_{leak}^{drain}, see Figure 2- 5. It is of course necessary to know and therefore to measure these leakage currents. In order to apply the drain and gate voltages and to monitor the source-drain and leakage currents, two measuring units (Keithley 2400) are placed as shown in Figure 2- 5.

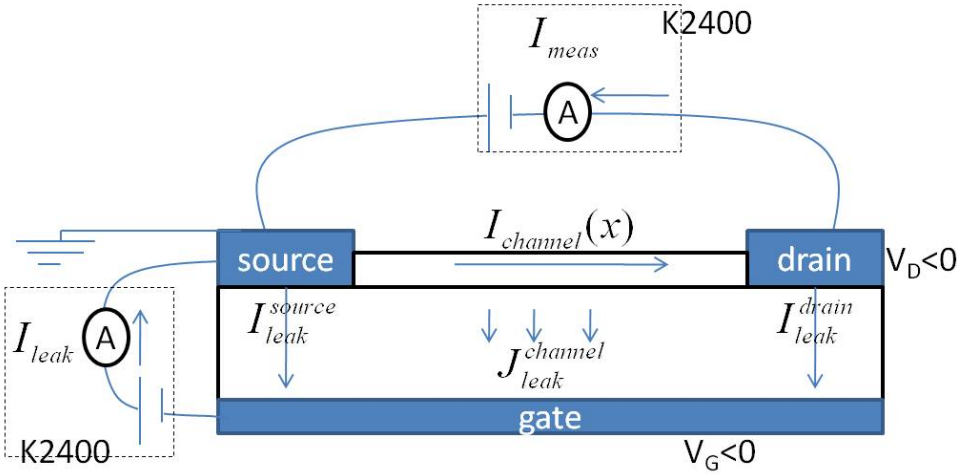

Figure 2- 5 OFET electrical connections. Two Keithley 2400 are used to bias V_D and V_G and to monitor I_{leak} and I_{meas}.

We write $I_{channel}(x)$ the current flowing in the channel (hence in the polymer). This current is decreasing with x (x is the axis from source to drain) due to the presence of $J_{leak}^{channel}$. What we want to obtain is the average current flowing through the channel (or the polymer), noted as $\overline{I_{channel}}$. Then, the problem is the following: how can we determine $\overline{I_{channel}}$ from the two measured currents I_{leak} and I_{meas}. For this, we apply the first Kirchhoff's law on four points:

- The source: $I_{leak} + I_{meas} = I_{channel}(0) + I_{leak}^{source}$
- The drain: $I_{channel}(L) = I_{meas} + I_{leak}^{drain}$
- The gate: $I_{leak}^{source} + I_{leak}^{drain} + J_{leak}^{channel}.L = I_{leak}$
- A channel segment from coordinate x to $x + dx$: $I_{channel}(x) = I_{channel}(x + dx) + J_{leak}^{channel}.dx$

We search $\overline{I_{channel}} = \frac{1}{L}.\int_0^L I_{channel}(x)dx$. Combining all these equations, we obtain the following correction that we apply for <u>every</u> OFET measurements:

$$I_D = \overline{I_{channel}} = I_{meas} + \frac{I_{leak}}{2}$$

The importance of the correction is very sample dependent. It depends on the quality of the SiO_2 dielectric (and in particular at the source and drain electrodes locations where the field is applied). One case where the correction is of prime importance is when we monitor I_D as a function of time at fixed drain and gate voltages, like in Figure 2- 6 and Figure 2- 8. When the OFET is switched on at time zero, there is an exponential decreasing I_{leak} corresponding to the charging of the dielectric. Consequently, the correction is essential for short time (say time <20 s) where the shapes of I_D and I_{meas} are completely different. For longer time, I_{leak} is constant but not zero and therefore there is an offset between I_D and I_{meas}. Values for I_{leak} are sample dependent but they are always smaller than 10 % of I_{meas}.

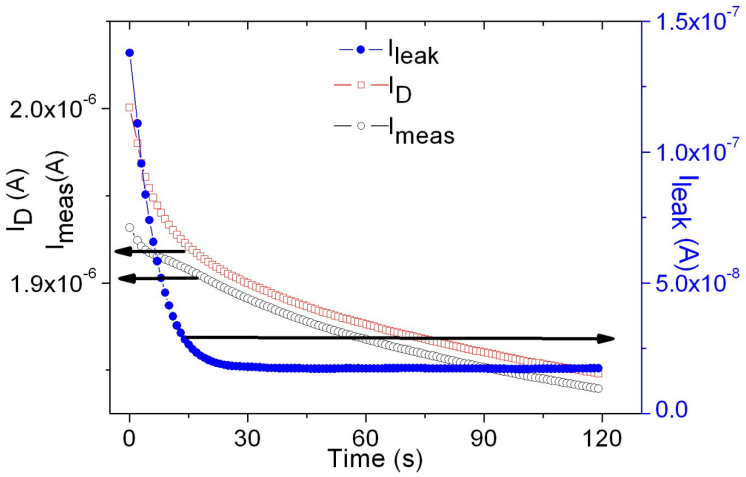

Figure 2- 6 Time dependence of the leakage, measured and drain currents at fixed V_D and V_G.

When performing transfer and output characteristics for extracting μ from the polymer, this dielectric charging effect is only present at the beginning of the voltage sweep which is most of the time in the off state domain and hence not used for fitting μ. However, there is always a residual I_{leak} (like in Figure 2-6 at long time) and the correction $I_D = \overline{I_{channel}} = I_{meas} + \frac{I_{leak}}{2}$ is routinely applied.

Speaking about transient effects, we note here that there are two others transient effects which are fortunately much too fast not to disturb our data. Firstly, the charge carrier transit time from source to drain is estimated at a few ms[9] and secondly the capacitance formed by the source and drain electrodes is about 10^{-4} pF. Both are much too fast effects for perturbing our measurements which have a time resolution not better than 500 ms.

2.2. Holes and electrons trapping in OFETs

This part of the chapter has been partially published in reference 6. Here, we focus on the trapping of holes and electrons when operating organic field-effect transistors (OFETs). Even if the huge majority of OFETs are p-type (hence conduct holes, in opposition with n-type which conduct electrons), we shall demonstrate that the undesired effects of electrons trapping are as much important as the holes one. We finish this section by giving some rules to minimize the holes and electrons trapping effects when using OFETs.

Electrical instability of OFETs manifests itself either as a decay with time of the drain current at fixed drain and gate voltage (see Figure 2- 8), either as a positive or negative voltage shift of the transfer characteristic (TC) (see Figure 2- 7) or as a hysteresis in the TC [10,11](see Figure 2- 9). The origins of trapping are multiple and can be split in different categories: intrinsic low mobility states due to

structural defects [12], stress-created trap states like bipolaron formation [13,14], interfacial trapping [15] and environmental factors such as humidity [16,17], ozone [18] and illumination [19].

Classic OFETs show p-type behaviour but Chua et al.[15] showed that at positive V_G and if the gate dielectric is passivated, electrons can be injected from the appropriate low-work-function electrodes to the polymer. In other words, most of the conjugated polymers are intrinsically bipolar. When performing OFETs measurements, V_G will be successively positive and negative leading to the occurrence of holes and electrons traps. In the literature, however, most of the studies are either concerned with electrical instability caused by hole trapping or either by electron trapping but not by both at the same time. In this part of the chapter, we systematically present the individual influences of hole ***and*** electron trapping on different features of the TC such as onset voltage V_{onset}, hysteresis between off-to-on and on-to-off sweeps and the transconductance $g(V_G) = \partial|I_D|/\partial|V_G|$ (the slope of the TC) whatever the causes or origins of trapping.

2.2.1. Materials

Measurements of section 2.2. are made on regioregular poly(3-butylthiophene) (P3BT) (number-average molecular weight 30.1 kg mol^{-1}, regioregularity 94%, polydispersity 2.29). The solvent is carbon disulfide (CS_2 boiling point: 46.3°C). The solution concentration is 1 wt %. Polymer solutions were spin-coated on OFETs substrates at 1000 rpm for 60 s.

2.2.2. General expression of the transconductance in function of n_{trap} and p_{trap}

A TC consists in applying negative and positive V_G. A negative V_G stress will induce holes in the channel with a fraction of them being trapped in pre-existing or in stress-created trap states. This trapped hole concentration (p_{trap}) results in an electrostatic screening shifting the TC towards negative V_G by a quantity ΔV_T or reducing the current by ΔI_D, see Figure 2- 7. Similarly, after applying a positive V_G an electron concentration (n_{trap}) is trapped in the channel resulting in a positive voltage shift and in a current increase due to the extra hole population needed to balance the n_{trap}. To analyse the effects of p_{trap} and n_{trap} on TCs, a general expression for the transistor current and the transconductance can be derived. The total hole concentration is influenced by trapped charges $p_{tot} \propto C_0/e\,.|V_G - V_T| + n_{trap} - p_{trap}$ where the second and third terms represent what was said above. In linear mode, the transistor current is $|I_D| = \mu(V_G) W V_D e \frac{p_{tot}}{L}$ with $\mu(V_G)$ a gate voltage dependent mobility. A power law dependence is commonly used describing either hopping in an exponential distribution of localized states [20] or charge transport limited by continuous trapping and release between trap states and band transport [21]. Combining these equations, we obtain

$$|I_D| \propto \mu(V_G)\frac{W}{L} V_D e \left(\frac{C_0}{e}|V_G - V_T| + n_{trap} - p_{trap}\right) \quad (1).$$

More interesting, is the general expression of the transconductance, the slope of the TC:

$$g(V_G) = \frac{\partial|I_D|}{\partial|V_G|} \propto \mu(V_G)\frac{W}{L} V_D e \left(\frac{C_0}{e} + \overbrace{\frac{\partial(n_{trap})}{\partial|V_G|}}^{elec\ detrapping<0} - \overbrace{\frac{\partial(p_{trap})}{\partial|V_G|}}^{hole\ trapping>0} + \frac{\partial\mu(V_G)}{\partial|V_G|}.\frac{p_{tot}}{\mu(V_G)}\right) \quad (2)$$

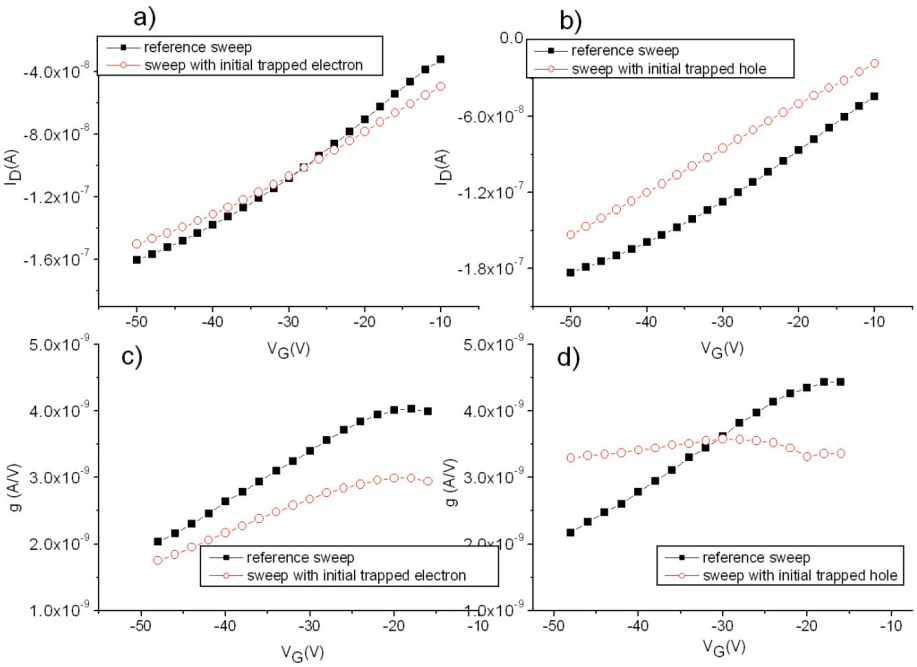

Figure 2- 7 OFET off-to-on sweeps. a) reference TC and TC after intentional electron trapping (initial n_{trap}=7.5 10^{11} cm^{-2} corresponding to a stress of 1min at 50V). b) reference TC and TC after intentional hole trapping (initial p_{trap}=1.7 10^{12} cm^{-2} corresponding to a stress of 1min at -50V). c) $g(V_G)$ of Figure 2- 7a). d) $g(V_G)$ of Figure 2- 7b).

For an off-to-on sweep (right to left) in the negative region, the electrons are detrapped and the holes are trapped. Then, the second ($\partial(n_{trap})/\partial|V_G|$) and third terms ($-\partial(p_{trap})/\partial|V_G|$) of equation (2) are both negative and $g(V_G)$ is reduced by hole trapping and electron detrapping. The fourth term is always positive. Figure 2- 7a) shows a normal off-to-on sweep and a sweep after intentional electron trapping. It illustrates the increase of $|I_D|$ at V_G = -10 V as expected from (1). On Figure 2- 7c), the two corresponding transconductance curves are reported. It is seen that for each gate voltage the transconductance is reduced for the intentional n_{trap} case. This is because electron detrapping is amplified due to the excess of trapped electron, i.e. the second term in (2) reduces $g(V_G)$. Note that the decrease of $g(V_G)$ with decreasing V_G, the upward curvature of the TC, will be explained later in the text.

Figure 2- 7b) shows a reference TC and a TC after intentional hole trapping. It illustrates the decrease of $|I_D|$ at V_G = -10 V as expected from (1). Finally, Figure 2- 7d) depicts the two $g(V_G)$ graphs. The initial p_{trap} is equivalent to one minute stress at V_G = -50 V meaning that p_{trap} is saturated during the scan and no additional hole trapping can occur leading to the constant $g(V_G)$ curve.

2.2.3. Measurements of n_{trap} and p_{trap} at fixed V_G

Since a TC is a scan through different values of V_G, it seems relevant to evaluate p_{trap} and n_{trap} along the full sweep range for different fixed V_G. The concentrations are measured by comparing a fraction of the TC before and after stressing the semiconducting film. In the linear regime, these concentrations can be calculated using

$$(p,n)_{trap} = \frac{C_0|\Delta V_T|}{e} = \frac{|\Delta I_D|L}{e\mu W V_D} \quad (3)$$

The comparisons between two sweeps made on Figure 2- 7 are not ideal because the reference sweep has a lot of influence on the trapping concentrations making the evaluation inaccurate. On the other hand, if the reference is one point then the influence is much lower[22]. Since the stress for measuring n_{trap} is in the off state it is impossible to measure a current, then the comparison is done at zero V_G.[23].

V_G [V]	-50	-30	-10	10	30	50
	p_{trap} [cm^{-2}]			n_{trap} [cm^{-2}]		
SiO_2 interface	1.7 10^{12}	5.0 10^{11}	1.2 10^{11}	6.5 10^{10}	4.0 10^{11}	7.5 10^{11}
HMDS interface	2.0 10^{11}	9.0 10^{10}	4.5 10^{10}	6.0 10^{10}	1.2 10^{11}	1.7 10^{11}

Table 1 p_{trap} and n_{trap} for two types of dielectric at different V_G for 1min stress. Note the super-linear V_G dependence of p_{trap}.

Table 1 summarizes the trapped charge concentrations for two types of dielectric surfaces. As expected, n_{trap} is lower for the HMDS interface (more on HMDs can be found in chapter III) since it substitutes the polar silanols groups, responsible for electron trapping, by apolar 0-Si-CH_3 groups[15] which do not trap electrons. This apolar termination is believed to attract the apolar butyl side chain towards the interface enhancing the polymer self-organization and hence the mobility[24], see Table 2. This enhanced structural ordering is thought to be the reason for the one order of magnitude reduction of p_{trap} with respect to the SiO_2 interface. It is known from literature[12] that the bulk trap states distribution of Alq_3 films is influenced by the degree of crystallinity of the film. Finally, we note that for both dielectrics p_{trap} follows a super-linear dependence with respect to V_G. The super-linearity can also be checked by measuring the normalized drain current decay[25] at fixed V_D and for different V_G. Equation (3) can be written as

$$p_{trap} = \frac{I_D(0)-I_D(t)}{I_D(0)} \cdot \frac{(V_G-V_T)C_0}{e} \quad (4)$$

where $\Delta I_D/I$ is the percentage of charges being trapped as depicted on Figure 2- 8. For instance, after 1min at -35V almost 10% of the induced charges in the channel are trapped. From Figure 2- 8, it is clearly seen that the percentage of trapped charges is proportional to $|V_G|$. Since the quantity of charges

is increasing as well with $|V_G|$, a super-linear dependence is again found. A possible mechanism of charge trapping is bipolaron[13] for which the principal feature is a hole trapping rate proportional to the square of the hole concentration: $\partial p_f / \partial t = -k.p_f^2 + b.p_{BP}$ where p_f is the free hole concentration, k is a bipolaron formation rate constant, b is a bipolaron dissociation rate constant and p_{BP} is the bipolaron concentration. For stress time in the ms range, bipolaron formation mechanism was proved to be the origin of trapping in polythiophene films[13]. In our case, a power coefficient of 1.8, close to 2, is found for stress time of 10 sec and 1.5 for stress time of 1min: the coefficient deviates from 2 as the stress time is increased. A possible explanation could be that bipolaron formation is the origin of trapping in the ms scale and a second mechanism, like proton migration towards the dielectric which was recently proposed[26], becomes predominant at higher time.

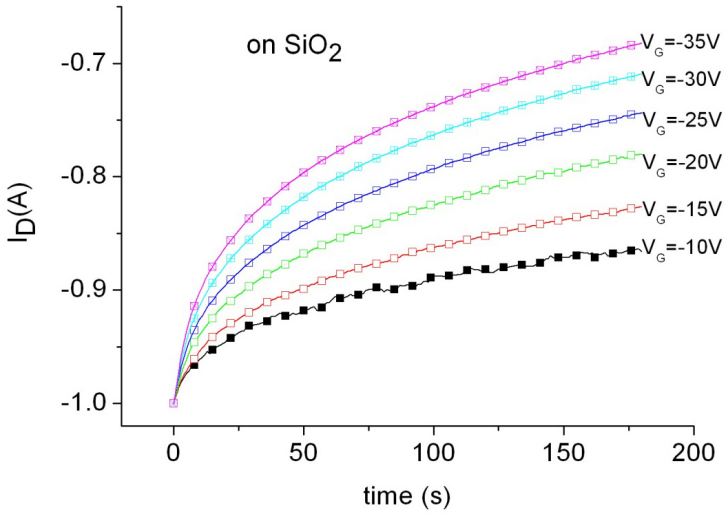

Figure 2- 8 Normalized drain current decay at V_D = -3 V and different fixed. V_G The percentage of induced charges being trapped is increasing with $|V_G|$ like the quantity of induced charges leading to a super-linear dependence.

2.2.4. Effects of n_{trap} and p_{trap} on the transconductance

Typical TCs in the linear regime on as-cast P3BT films are depicted in Figure 2- 9a) with different sweep ranges. We see that the transconductance is decreasing with decreasing V_G, the TC is upward curved on the left extremity. This was expected from the super-linear V_G dependence of p_{trap}: the third term in (2), $-\frac{\partial p_{trap}}{\partial |V_G|}$, is decreasing as V_G is becoming more and more negative during the off-to-on sweep making g smaller and leading to the upward curvature. It means that the transconductance reduction is due to hole trapping and not to a contact resistance effect as could be deduced. As confirmation it was observed that this decrease of g also occurs when sweeping is restricted to negative V_G i.e. electrons

play no role, see Figure 2- 10. This effect is almost absent for the HMDS treated sample, Figure 2- 9b), as expected from Table 1 where p_{trap} is reduced by one order of magnitude. It is worth noting that a low level of p_{trap} is a necessary condition for an increasing $g(V_G)$ at negative V_G like this is the case for the HMDS treated sample.

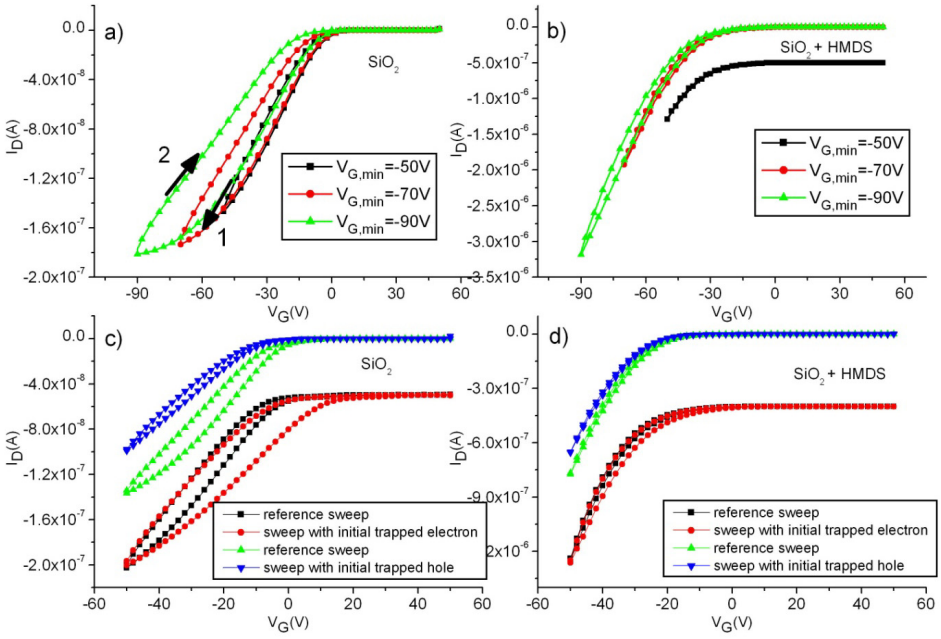

Figure 2- 9 a) TCs as a function of the sweep range. Gate dielectric : SiO_2. b) idem for HMDS treated dielectric. c) Effect on TCs of intentional holes and electrons trapping for SiO_2 (initial n_{trap}=1.5 10^{12} cm^{-2}, initial p_{trap}=4.0 10^{12} cm^{-2}). d) idem for HMDS treated dielectric (initial n_{trap}=4.0 10^{11} cm^{-2}, initial p_{trap}=4.0 $10^{11}$$cm^{-2}$).

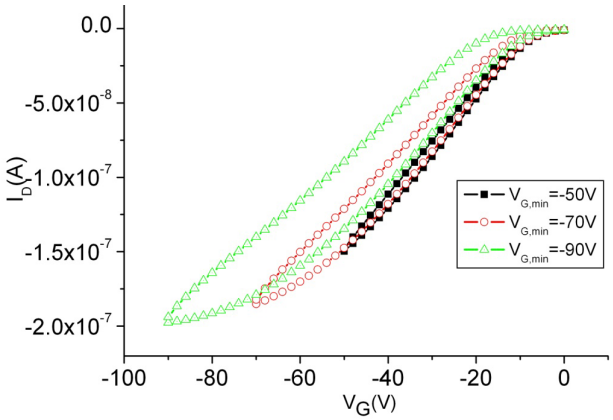

Figure 2- 10 TC for negative V_G only to exclude effect of electron trapping. It shows that hole trapping is responsible for the TC curvature at high negative V_G

2.2.5. Effects of n_{trap} and p_{trap} on the hysteresis and V_{onset}

As depicted in Figure 2- 9c) and d), TCs before and after intentional trapping have been compared. Whatever the sweeping direction, I_D in the on-to-off is always smaller than I_D in the off-to-on. This hysteresis is caused by both charges. During the off-to-on sweep, initially trapped electron at high positive V_G are continuously detrapped. Due to a detrapping rate slower than sweep rate (2 Vs^{-1}), the instantaneous n_{trap} at each V_G is higher than equilibrium. During the on-to-off sweep, it is expected that n_{trap} is pinned at its minimum value until V_G reaches 0 V. Consequently, $n_{trap}(V_G)_{off\ to\ on} > n_{trap}(V_G)_{on\ to\ off}$ is valid at each voltage which explains that I_D is higher for the off-to-on sweep, see equation (1). On Figure 2- 9c), a reference TC with a TC after intentional electron trapping are compared. This is obtained by applying a positive V_G for a certain time and measured as explained before. Clearly it is seen that hysteresis is proportional to the amount of initially trapped electrons. A similar reasoning can be done for hole trapping. During the off-to-on sweep, holes are continuously trapped according to a super-linear dependence (Table 1). Once the turning voltage is reached, hole detrapping occurs but due to detrapping inertia $p_{trap}(V_G)$ is a combination of previous p_{trap} at higher $|V_G|$ leading to $p_{trap}(V_G)_{off\ to\ on} < p_{trap}(V_G)_{on\ to\ off}$ which explains that I_D is higher for the off-to-on sweep, see equation (1) again. This is confirmed in Figure 2- 9c) where saturation of trapped hole before scanning (by applying a negative V_G for a certain time) reduces considerably the hysteresis with respect to the reference TC. Then, we can conclude that the hysteresis is caused by both charges. Figure 2- 9d) shows that the effect is much lower for the HMDS treated dielectric as foreseen by Table 1. Additionally, we note that V_{onset} is largely n_{trap} and p_{trap} dependent as expected from equation (1): right-shifted by n_{trap} and left-shifted by p_{trap}.

2.2.6. Implications for OFETs

All the trap-induced effects discussed above are a good tool to work out the OFETs TCs. Nevertheless, it is always wise to characterise OFETs in a way which minimises the trap concentration. First, it is evident

that the sweep rate must be as high as possible to reduce the total stress time. Current decay studies showed that trapping can last for months[25]. The use of a pulsed source can also be a solution. Second, we see in Figure 2- 9 the negative effect of electron trapping. It means that when characterizing p-type polymers it is better to restrict the V_G sweep range to negative values and hence not to induce n_{trap}. Third, it was observed that illumination[27] induces more p_{trap} and n_{trap} with respect to dark measurements, see Figure 2- 11. The reason is that light exposure causes an excess of photogenerated electrons and holes which represent an extra population of carriers likely to be trapped. Consequently, the transconductance is reduced because of larger electron detrapping during the off-to-on sweep. In a worst case, we were able to measure an apparent "negative mobility": the absolute current decreases for an off-to-on sweep (see Figure 2- 11). This dramatic situation consists in stressing the device at positive V_G for some minutes under light such that an excessive quantity of photogenerated electrons is trapped. Then the transistor is swept from -10 V to -30 V for example. At -10 V a big part of the electrons are detrapped so that the second term of (2) exceeds the first term and leads to a negative $g(V_G)$.

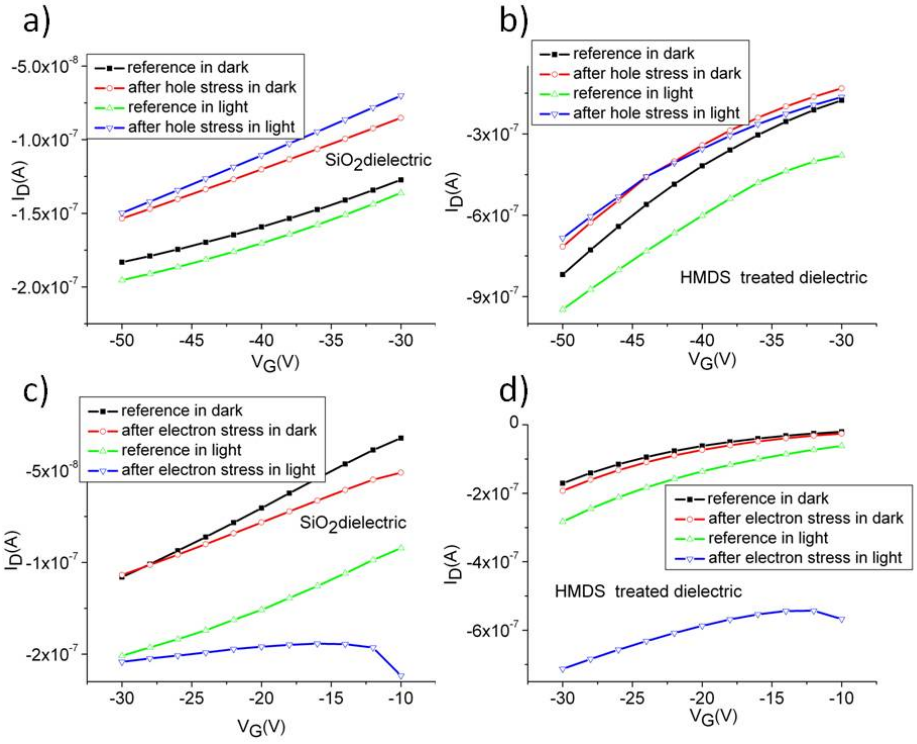

Figure 2- 11 Effect of light on electron and hole trapping. a) Comparison of hole trapping effect (V_G = -50 V for 1min) on the TC between dark and light (~ 10 mW cm^{-2}) for SiO_2 dielectric. The TC shift is higher when the sample is illuminated. b) idem for HMDS treated dielectric. c) and d) Comparison of electron trapping effect (V_G = +50 V for 1min) on the TC between dark and light (~ 10 mW cm^{-2}) . The TC shift is much higher when the sample is illuminated. Light amplified more electron trapping

than hole trapping (compare a) with c) and b) with d)). Note the apparent negative mobility for the curves after electron stress in light in c) and d), this is due to an excess of electron detrapping when starting sweeping at V_G = -10 V.

Table 2 shows that μ decreases by 35% when the sweep rate is reduced from 5 Vs^{-1} to 0.6 Vs^{-1}. Furthermore, comparison between full and half range measurements indicates that electron detrapping can lower μ by 10%. Finally, operation under light decreases the mobility by 40%. As expected, the reductions are almost absent for the passivated device.

Sweep rate	Fast 5 Vs^{-1}		Normal 2 Vs^{-1}		Slow 0.6 Vs^{-1}	Normal in light [27]
Sweep Range	Half	Full	Half	Full	Full	Full
SiO_2 interface	2.0 10^{-4}	1.9 10^{-4}	1.8 10^{-4}	1.6 10^{-4}	1.3 10^{-4}	1.2 10^{-4}
HMDS interface	2.0 10^{-3}	2.0 10^{-3}	2.0 10^{-3}	1.9 10^{-3}	1.6 10^{-3}	1.5 10^{-3}

Table 2 Mobility ($cm^2 V^{-1} s^{-1}$) measured at V_G = -40 V as a function of sweep rate, sweep range and illumination. Sweep range: Half: V_G: 0 V ➔ -50 V, Full: V_G: 50 V ➔ -50 V.

Therefore, implications for OFETs are that measurements should be carried

- In dark
- At high sweep rate
- V_G sweep range must be restricted to negative values to avoid detrimental n_{trap}.

[1] A.R. Brown et al., *Synth. Met*. **1997**, 88, 37-55.
[2] C.D. Dimitrakopoulos et al., *Adv. Mater.* **2002**, 14, 2, 99-117.
[3] D. Braga and G. Horowitz, *Adv. Mater.* **2009**, 21, 1473-1486.
[4] H. Sirringhaus, *Adv. Mater.* **2005**, 17, 2411-2425.
[5] M. Breselge, Electrical Characterization of 2,5-Substituted Poly(p-Phenylene Vinylene) Derivatives and Their Application in Organic Bulk Heterojunction Solar Cells, **2007**, Phd thesis, University Hasselt
[6] J.-C. Bolsée and J.V. Manca, *Synth. Met*. **2011**, 161, 789-793.
[7] G.K.V.V. Thalluri et al., *Sol. Energy. Mat & Sol. Cell* **2011**, accepted.
[8] G. Horowitz et al., *Adv. Funct. Mater.* **2004**, 14, 11, 1069.
[9] Assuming a typical mobility of $10^{-3} cm^2 V^{-1} s^{-1}$, a channel length of 40 µm and a drain voltage of 4 V, we have a carrier transit time of 4 ms.
[10] H. Sirringhaus, *Adv. Mater.* **2009**, 21, 1.
[11] P. D'Angelo et al., *Appl. Phys. A.* **2009,** 95, 55.
[12] R. Schmechel and H. von Seggern, *Phys. Stat. sol. (a)* **2004**, 201, 6, 1215.

[13] R.A. Street et al., *Phys. Rev. B* **2003**, 68, 085316.
[14] A. Salleo and R. A. Street, *Phys. Rev. B* **2004**, 70, 235324.
[15] L.L. Chua et al., *Nature* **2005**, 434, 194.
[16] M.L. Chabinyc et al., *Appl. Phys. Lett.* **2006,** 88, 113514.
[17] S. Hoshino et al., *J. Appl. Phys*. **2004**, 95, 5088.
[18] M.L. Chabinyc et al., *Appl. Phys. Lett.* **2007**, 90, 123508.
[19] G. Gu et al., *J. Appl. Phys.* **2007**, 101, 014504.
[20] M.C.J.M. Vissenberg and M. Matters, *Phys. Rev. B*. **1998**, 57, 12964.
[21] G. Horowitz et al., *J. Appl. Phys.* **2000**, 87, 4456.
[22] Procedure for evaluating p_{trap} at $V_{Gstress}$: 1/measurement of $I_D(V_{Gstress})$ 2/stress for 1 min at $V_G = V_{Gstress} < 0$ 3/off-to-on sweep from $V_G = V_{Gstress}$ to measure $\mu(V_{Gstress})$ and $I_D(V_{Gstress})$ 4/use of $p_{trap} = \Delta I_D L/e\mu W V_D$

[23] Procedure for evaluating n_{trap} at $V_{Gstress}$: 1/measurement of $I_D(0)$ 2/stress for 1 min at $V_G = V_{Gstress} > 0$ 3/off-to on sweep from $V_G = 0$ to measure $\mu(0)$ and $I_D(0)$ 4/use of $n_{trap} = \Delta I_D L/e\mu W V_D$
[24] H. Sirringhaus et al., *Synth. Met.* **1999**, 102, 857.
[25] S.G.J. Mathijssen et al., *Adv. Mater.* **2007**, 19, 2785.
[26] A. Sharma et al., *Appl. Phys. Lett.* **2009**, 95, 253305.
[27] The light intensity is estimated at ~10 mW cm^{-2}. A current of 6 mA was measured with a photodiode whose quantum efficiency spectrum is known. The light source was assumed as a black body with a temperature of ~3200 K.

A life spent making mistakes is not only more honorable, but more useful than a life spent doing nothing
- George Bernard Shaw -

Chapter III: OFETs - Results

This chapter presents the charge transport measurements we have performed on poly(3-alkylthiophene) samples with the standard field-effect transistor structure described in chapter II. In the first part, the importance of molecular orientation at the dielectric interface is highlighted. The second part is dedicated to the influence of the surface dielectric on the charge transport. Finally, we finish the chapter by focusing on the differences occurring between a web of nanofibers and a film of nanofibers

3.1. Introduction

The use of Poly(3-alkylthiophene)s (P3*A*Ts) (for an introduction on P3*A*Ts see chapter I) and in particular poly(3-hexylthiophene) (P3HT) as working material for organic field-effect transistors has been first reported in 1996[1], followed by a substantial number of publications. The reasons for this intense interest are that P3HT exhibits 1) a good solubility in most common organic solvents, 2) a large overlap between π-orbitals delocalized over the polymer chain and 3) a well-ordered semi-crystalline structure. P3*A*Ts crystallize in a self-organized lamellar structure formed by successive layers of polymer backbones and layers of perpendicularly oriented alkyl side chains[2]. This regular arrangement allows for efficient π-π stacking of the conjugated backbones and leads to a fiber structure (see chapter I).

Field-effect mobility of P3*A*Ts films has been proved to depend on several parameters such as the deposition technique[3], the solvent type[4,5], the presence of a passivation layer[6], the use of an annealing treatment[7] and last but not least the crucial role of molecular weight[8,9,10.] Furthermore, it has been shown that high degree of regioregularity is necessary for nanofibers crystallization[11]. As we see, OFETs on P3*A*Ts are very delicate and care on many parameters must be taken when trying to compare samples to samples or with literature values. We have seen in Table 2 of chapter I that the variation of regioregularity is small enough meaning that its influence on charge transport is negligible. Moreover the values of the number-average molecular weight are all sufficiently high to be in the region where the mobility is molecular weight independent[8,9,10]. In other words, the influences of regioregularity and molecular weight can be excluded.

In order to clarify and facilitate the following discussions, all the layers we have analyzed can be separated in two mains systems:

1. **Films or webs of nanofibers (model system 1)**. The layers are prepared from nanofiber dispersions as explained in chapter I. Each P3*A*T has its own solvent, see Table 2 in chapter I. By

changing the dispersion concentration, we will study either a web of NFs or a film of NFs. For these layers, the crystallization occurs mainly before deposition.

2. **Chlorobenzene processed films (model system 2)**. The layers are prepared from molecularly dissolved polymer solutions (in this case we use chlorobenzene (CB) as the good dissolving solvent for P3*A*Ts). For these films, the crystallization occurs during the film deposition.

Caution must be paid to the fact that the name chlorobenzene processed film does not mean that these films, once dried, do not contain nanofibers crystallites. Indeed, it is more than often observed that chlorobenzene processed films exhibit nanofibers crystallites immersed in an amorphous matrix. This point is clearly observed in Figure 3- 1 where nanofibers are seen on the AFM phase images.

Important remark: In order to avoid any confusion in the discussions, we use the following convention. Before any measurement, a polymer solution is deposited and dried into a solid thin film on a FET substrate. We call the "buried (air) interface" the interface between the substrate (air) and the deposited polymer film. Since we use a bottom gate OFET geometry (see chapter II), in order to measure the mobility at the air interface the film has to be flipped upside down by a delamination technique. In the flipped configuration, we keep the initial names: the buried interface is in contact with the air and the air interface is in contact with the substrate.
In other words, buried (air) interface is the interface between the substrate (air) and the thin film during the drying process and not those after the flipping step.

3.2. The importance of molecular orientation at the dielectric interface

All the measurements reported in this section are for polymer layers deposited on bare SiO_2 dielectric. The effects of others dielectrics will be investigated in section 3.3.

3.2.1. Buried interface[12]

P3*A*Ts NFs and CB films for *A* ranging from 4 to 9 have been spin-coated (see end of this chapter for all the preparation details). The resulting AFM phase images are shown in Figure 3- 1.

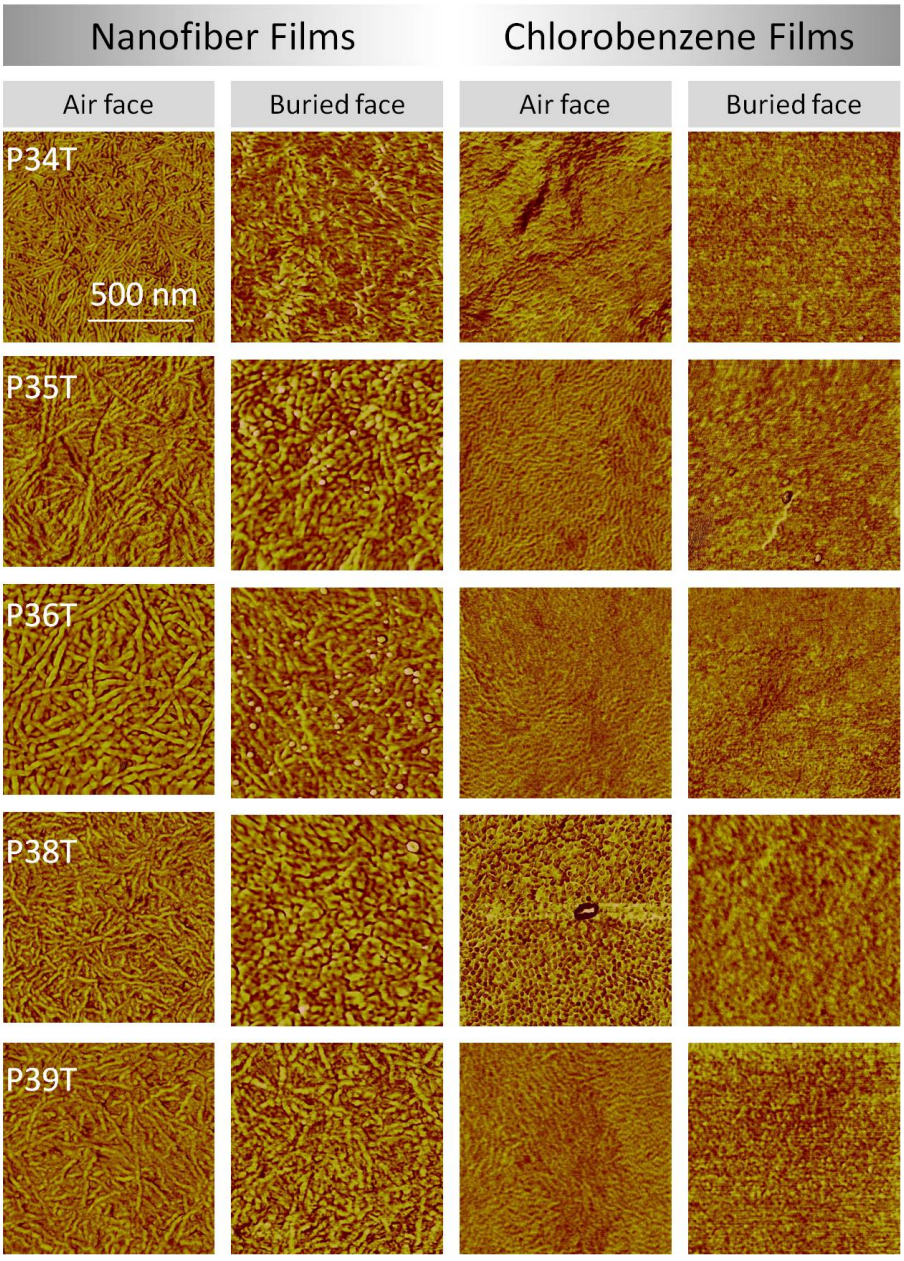

Figure 3- 1 AFM phase images on SiO_2 for CB (2 wt%) and NFs films for the air and buried interfaces as a function of the number of carbon atoms in the side chain. In order to access the buried interfaces, the layers were turned upside down by means of a HF treatment.

Using the same processing conditions, these films are deposited on a OFET structure in a bottom gate bottom contact configuration (see chapter II for the method) and field-effect mobility values are obtained for each film and reported in Figure 3- 2. No gate voltage dependence on the mobility was observed (except of course for the subtreshold region). These mobility measurements correspond to the buried interfaces of Figure 3- 1. First of all, we observe that the chlorobenzene films (for both concentrations) display a trend: the mobility is getting higher when the alkyl side chain is reduced: a factor 10 improvement is obtained when going from P39T to P34T. This fact is not new and was reported in the literature many times[13,14,15] even if the exact physical explanation was still unclear. In complete contrast with the CB films, the field-effect mobility for the set of nanofiber films shows no variation when *A* is varied. All values are comprised in the sharp range 24-35 $cm^2 V^{-1} s^{-1}$. To explain and understand these opposite behaviors between NFs and CB films, they were studied in great detail using several characterization techniques: Transmission electron microscopy (TEM), UV-Vis absorption spectroscopy, AFM and finally polarized near edge X-ray absorption fine structure (NEXAFS) spectroscopy[16]. This study was led by Dr. Wibren Oosterbaan (Hasselt University, organic chemistry group) and therefore only the key points will be given here. Intensive use of the NEXAFS measurements will be done through the thesis. They were performed at the Australian Synchrotron under the supervision of Dr. C. R. McNeill (University of Cambridge) and Dr. L. Thomsen (Australian Synchrotron) at the request of Dr. Oosterbaan.

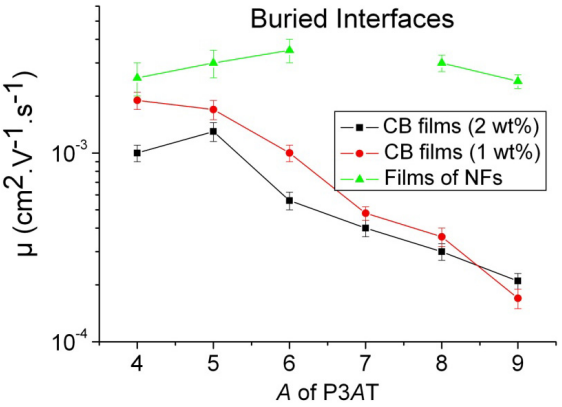

Figure 3- 2 Field-effect mobility of buried interfaces as a function of side chain length *A* for films from nanofiber dispersions and from molecularly dissolved solutions in chlorobenzene.

The explanation for the discrepancy between NFs and CB films was found using NEXAFS spectroscopy. NEXAFS is an unusual synchrotron-based technique that utilizes X-ray photons to study transitions between core states to unoccupied molecular orbitals[16]. It is not the intention to give here a detailed description of the working principle, measurement protocol and all the technique capabilities of NEXAFS. Very shortly, NEXAFS is a surface technique which gives information about the average molecular orientation. The output number from NEXAFS spectroscopy is the average thiophene tilt angle *<α>,* see schematic of Figure 3- 3. We have seen in chapter I that P3*A*Ts crystallize in a lamellar

structure. Several studies[11,17] have shown that crystallites from spin-coated films of P3*A*Ts have a strong preference for one of two orientations: "face-on" orientation and "edge-on" orientation (see schematics in Figure 3- 3) with the b and a crystal directions perpendicular to the substrate, respectively. Therefore, it means that the average thiophene tilt angle <*α*> is a weighted average between these two orientations. Comparing NEXAFS and OFETs measurements is very relevant because they are both surface sensitive techniques: sensitive depth is around 2.5 nm for P3HT[18] for NEXAFS while in OFETs charge transport occurs in the first nm at the dielectric interface[19].

The use of a bottom gate, bottom contacts transistor implies that the OFET structure measures the charge transport at the buried interface while NEXAFS probes the air interface. Therefore, in order to investigate the buried interface with NEXAFS, the layer has to be flipped upside down by means of a HF treatment, see Figure 3- 4.

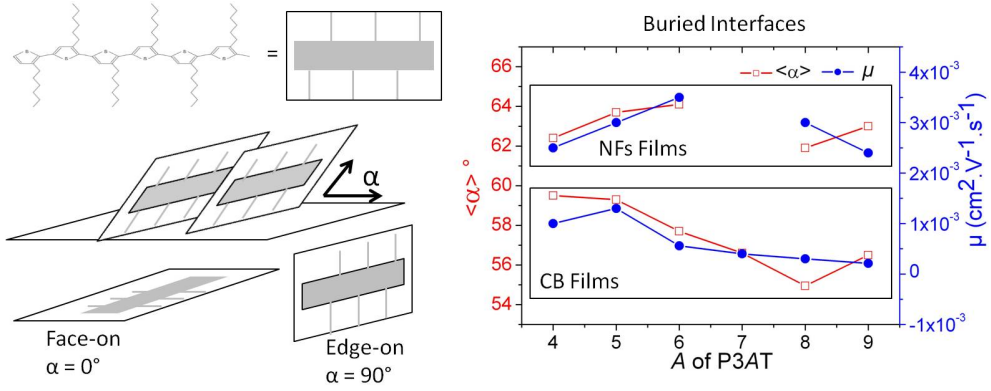

Figure 3- 3 Left: NEXAFS spectroscopy can quantify the average thiophene tilt angle ⟨α⟩. The two preferential crystallites orientations are depicted: α = 0° corresponding to the unfavorable face-on orientation and α = 90 ° corresponding to the favorable edge-on orientation. Right: matching between NEXAFS angle and OFETs mobility is remarkable for buried interfaces of nanofibers and CB films (2 wt%).

Figure 3- 3 right shows the NEXAFS angles and the corresponding field-effect mobilities of the buried interfaces, already shown in Figure 3- 2. Figure 3- 3 is remarkable. Average thiophene tilt angle <*α*> follows the same trends as the mobility: alkyl side chain independent for NFs films and getting higher at short side chain for CB films. This correlation suggests that charge transport at the dielectric interface can be predicted by the thiophene backbone orientation at the interface. The *A* independent mobility for NFs films can then be explained: being self-assembled in the dispersion, the NFs can hardly change their orientation when deposited on the dielectric leading to an average angle <*α*> independent of *A* which in turn gives a mobility independent on *A*. For the CB films, the situation is completely different. The polymer chains are dissolved in chlorobenzene and self-assemble during the drying process and, as evidenced by NEXAFS results, short side chain length allows for better (more edge-on) orientation leading to higher mobility than long side chain.

3.2.2. Air interface[20]

The measurements performed for buried interfaces can also be made for the air interfaces. Now, the NEXAFS can be directly performed on the deposited films while our bottom gate, bottom contacts FET structure requires to flip upside down the films. The technique is illustrated in Figure 3- 4.

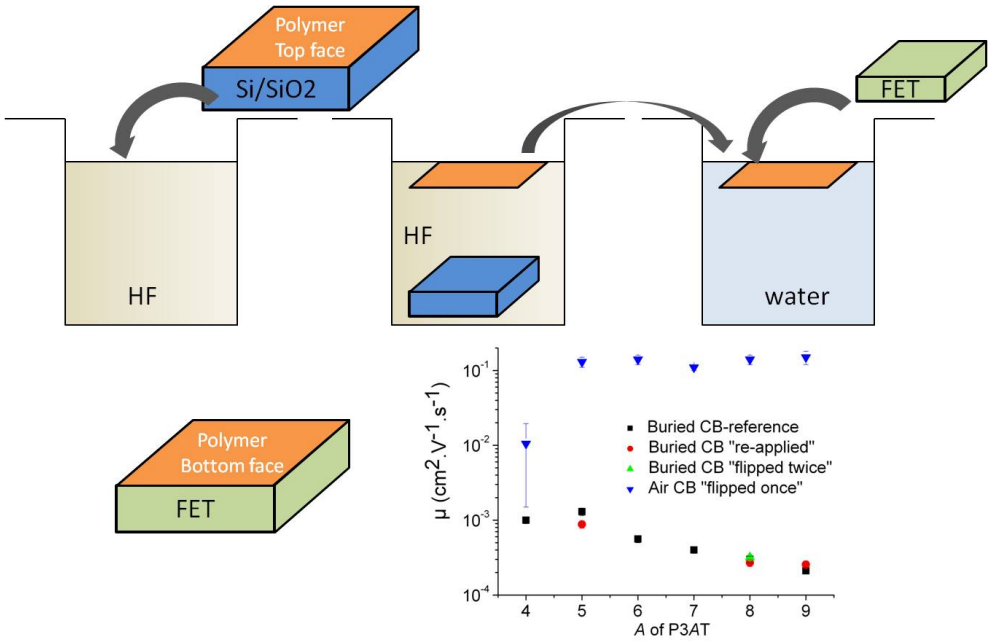

Figure 3- 4 Strategy followed to turn polymer film upside down. The SiO_2 layer is etched by HF and then releases the self standing polymer film which can be transferred in water to eliminate residual HF. In the end, the polymer layer is "fished" with a FET substrate with the originally buried face pointing up.

Surprisingly, the mobilities measured for the set of air interface CB films (Air CB "flipped once") are all two orders of magnitude higher than the buried face CB films (buried CB-reference which are the values reported in Figure 3- 2 for 2 wt%). For P34T, the mobility is lower and the error bar longer; this result is attributed to the lower solubility of P34T in CB which limits the reproducibility of the film formation. To check the validity of this strong result and in particular to check whether the HF treatment is valid, we have performed some additional proofs. In the first check experiment, the FET substrate "fishes" the self standing polymer film in such a way that the original buried face remains the buried face, in other words the film is not flipped. This check experiment, called buried CB "re-applied" , was performed on P35T, P38T and P39T. As seen on Figure 3- 4, the obtained mobility (red circle points) are the same than the reference points (black square points) meaning that the technique is valid. In the second check experiment, the polymer film is flipped two times so that the original buried face remains the buried face, in other words the film is not flipped. Applied on P38T, we call this experiment buried CB "flipped twice". Again, on Figure 3- 4 we see that the green triangle point is very close to the reference point. In

the end, the two check experiments prove that the HF treatment is valid and that the very high mobility values (0.1 $cm^2 V^{-1} s^{-1}$) obtained for the air interface CB films are valid.

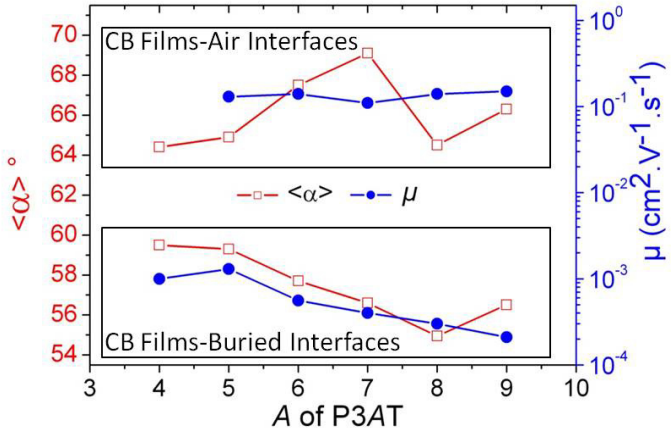

Figure 3- 5 Comparison of average thiophene tilt angle <α> with mobility μ for air and SiO_2 interfaces CB processed films.

Now, the question is to know whether these high mobility values could have been predicted by the NEXAFS measurements. On Figure 3- 5, the comparison between the average thiophene tilt angle and the field-effect mobility is shown. Again, the correlation is perfect: the average angles for the flipped films are significantly higher than for the buried faces and there is no trend on <α> for *A* varying from 4 to 9. Then, we can conclude that the molecular orientation at the dielectric interface is the parameter determining the charge transport in the polymer layers. This statement will be further analyzed in chapter VIII where additional information coming from the nanoscale part of the thesis will be added to the discussion. Finally, we compile all the mobility values from Figure 3- 2 to Figure 3- 5 in Figure 3- 6. This graph will also be discussed in chapter VIII.

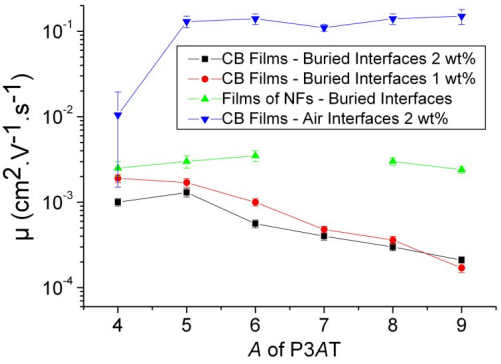

Figure 3- 6 Compilation of mobilities for NFs films, SiO_2 interface CB films and air interface CB films.

3.3. Effect of surface dielectric

It is well established that the surface dielectric properties influence considerably the charge transport in OFETs. For instance it has been proved by Friend et. al[21] that the type of transport in the FET channel (n or p types) can be modified by the presence of a self-assembled monolayers (SAM) on the silicon dioxide dielectric. The presence of hydroxyl groups (OH^-) at the surface of SiO_2 is known to trap the electrons. The SAMs reduces the concentration of hydroxyl groups and then allows electron conduction. One of the frequently employed SAMs is hexamethyldisilazane (HMDS). As we have experience throughout this thesis, HMDS deposited on SiO_2 has the following properties, Figure 3- 7:

- Transformation of the polar hydroxyl groups (OH^-) in apolar O-Si-CH_3 groups which
  - Attract the polymer alkyl side chains (promotes edge-on orientation)[22]
  - Cancel out electron trapping and hence promotes n-type OFETs (as seen in some ambipolar OFETs we have built[23])
- Transformation of SiO_2 from hydrophilic to hydrophobic (due to a change in surface energy[24]), see Figure 3- 8
- Reduction of the SiO_2 work function (see chapter VI)

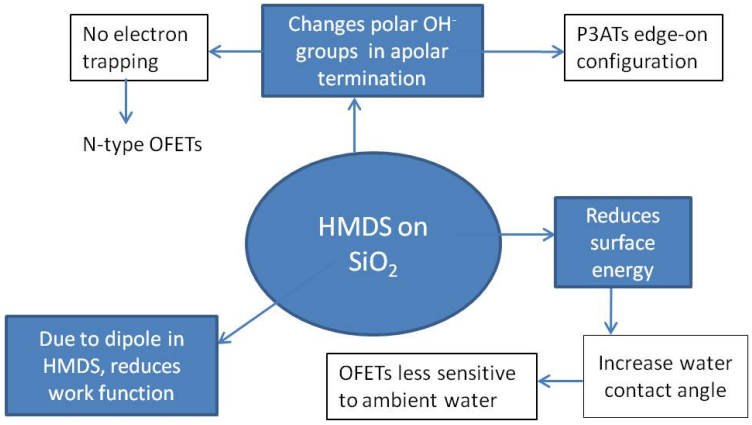

Figure 3- 7 Silanization of SiO_2 with HMDS has many influences on OFETs parameters.

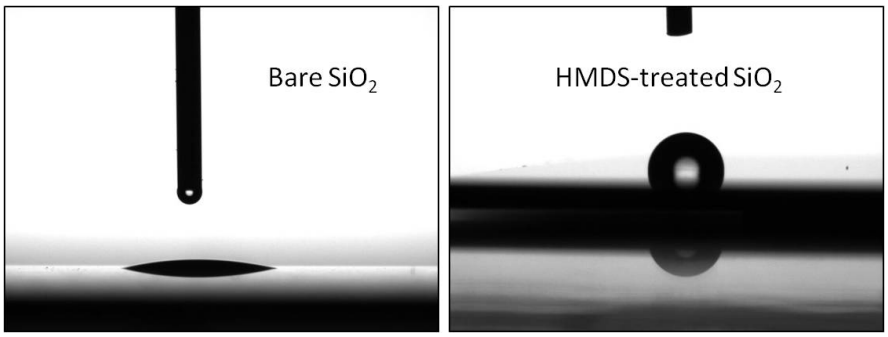

Figure 3- 8 Water contact angle measurements on hydrophilic bare SiO_2 (<10 °) and hydrophobic HMDS-treated SiO_2 (80-90 °).

In summary, HMDS on SiO_2 has three advantages on the performance of OFETs: (1) better edge-on orientation, (2) less sensitive to detrimental ambient humidity because of high hydrophobicity and (3) much less electron trapping bringing the onset voltage closer to 0 V. Since HMDS is known to promote edge-on orientations, the question is to know how HMDS influences the field-effect mobility in our polymers. We have investigated the effect of HMDS on samples made from nanofiber dispersion (in the forms of film and web) (model system 1) and from molecularly dissolved solution (chlorobenzene processed films, model system 2). The results are summarized in Table 1.

From nanofiber dispersions (model system 1)		
A	μ ($cm^2 V^{-1} s^{-1}$) on SiO_2	μ ($cm^2 V^{-1} s^{-1}$) on HMDS
Web of nanofibers		
4	5.5×10^{-2}	5.5×10^{-2}
Film of NFs		
6	3.5×10^{-3}	2.6×10^{-3}
8	3.0×10^{-3}	3.3×10^{-3}
Chlorobenzene Films (model system 2)		
A	μ ($cm^2 V^{-1} s^{-1}$) on SiO_2	μ ($cm^2 V^{-1} s^{-1}$) on HMDS
5	1.7×10^{-3}	2.0×10^{-3}
6	1.0×10^{-3}	2.2×10^{-3}
7	5.2×10^{-4}	1.2×10^{-3}
8	4.4×10^{-4}	2.0×10^{-3}
9	1.7×10^{-4}	1.9×10^{-3}

Table 1 HMDS treatment of SiO_2 does not influence μ for samples prepared from nanofiber dispersions (films and webs) but it enhances μ for samples prepared from molecularly dissolved solutions.

It is very interesting to see that for samples prepared from nanofiber dispersions (films and webs) the mobility is not changed by the HMDS treatment. It indicates that the nanofibers, which have already crystallized and assembled in dispersion, cannot change their orientation when deposited and dried on

the substrate. AFM images, Figure 3- 9, on web of P34T NFs confirm that SiO_2 passivation has no effect on the topography.

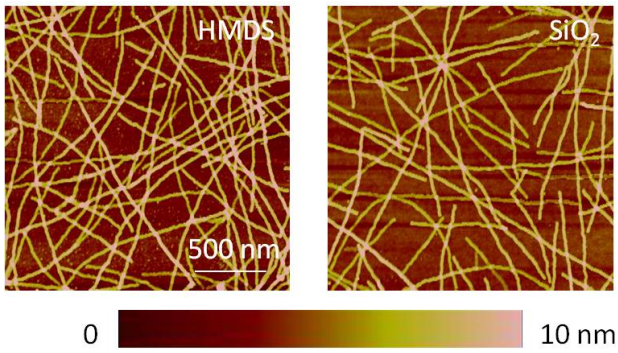

Figure 3- 9 Height AFM images showing that passivation of SiO_2 does not change the P34T NFs topography.

On the other hand, HMDS has a clear positive impact on chlorobenzene processed films. It is very interesting to plot the data of Table 1 and Figure 3- 2 on Figure 3- 10. When looking at Figure 3- 10 left plot and Table 1, we observe three points:

1. The gain (defined as μ_{HMDS}/μ_{SiO2}) is reduced at shorter alkyl side chains: gain is around 10 for P39T but is almost 1 for P35T.
2. The maximum μ is the same for HMDS and for SiO_2 dielectrics: about 2 X 10^{-3} cm^2 V^{-1} s^{-1}.
3. The μ is alkyl side chain independent on HMDS.

Point 1 strongly suggests that the positive effect of HMDS is due to a better molecular orientation (edge-on orientation). Indeed, we have seen in Figure 3- 3 that molecular ordering is very bad for P39T and then leaves a lot of room for orientation improvement (hence a gain 10) while orientation is better for P35T leading to a smaller gain (=1). The conclusion that the beneficial effect of HMDS is due to a better molecular ordering at the interface is reinforced by point 2. Indeed, a common maximum value for both dielectrics indicates that an optimal morphology is reached by a common mechanism, i.e. by molecular orientation at the interface. Finally, point 3 indicates that the beneficial effect of HMDS on the orientation is stronger than the beneficial effect of short *A*. Consequently this latter effect is hidden.

3.3.1. Conclusion

In Figure 3- 10, we see clearly that the mobility of the CB films is influenced by the alkyl side chain length *A* and the surface dielectric while NFs layers (webs and films) are independent on these two parameters (we have even observed that the mobility of a web of NFs is not influenced by the deposition technique, drop-casting or spin-coating). The reason is that, since the nanofibers crystallize in the dispersion (hence before film deposition), when they are deposited on the substrate their orientation is hardly influenced by the type of dielectric, deposition technique or the length of side chains. The situation is completely different for samples obtained from chlorobenzene solution. They are sensitive to the type of surface dielectric and the length of side chains, the reason being that the crystallization occurs during (and not

before) the film deposition and then the orientation of the polymer chains can be influenced by external factors such as the dielectric surface, deposition technique and side chain length. This point will be further discussed in chapter VIII.

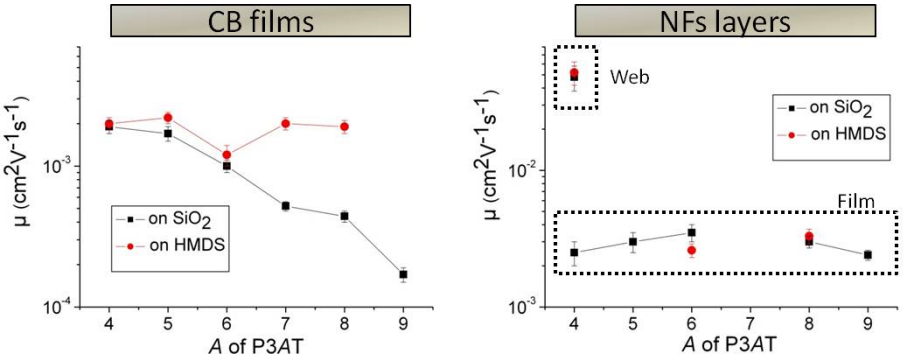

Figure 3- 10 From data of Table 1 and Figure 3- 2: on samples prepared from chlorobenzene solutions, dielectric surface and alkyl chain length influences the mobility. On samples (films and webs) prepared from nanofiber dispersions, there is no influence of dielectric and alkyl chain length.

3.4. On web and film of nanofibers

In this section, we focus on the layers prepared from the P34T nanofiber dispersions (described as model system 1 in the introduction).

3.4.1. Web of nanofibers at low surface coverage

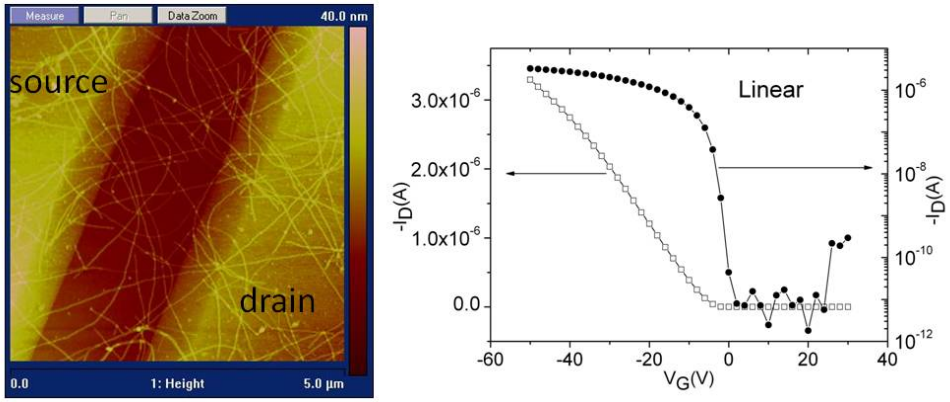

Figure 3- 11 Left: AFM image showing a web of P34T nanofibers crossing the OFET channel. Right: resulting transfer characteristic in the linear mode V_D=-4 V. Surface coverage is 9%.

Figure 3- 11 shows an AFM height image of a web of P34T nanofibers and the corresponding OFET measurement. The displayed transfer characteristic looks like the one from a perfect transistor, as confirmed by the parameters in Table 2. Indeed, the current ratio between ON and OFF states is among the best reported value I_{ON}/I_{OFF} ~10^6. Moreover, the onset voltage, defined as the voltage at which conduction starts, is very close to 0 V which is the expected value for a layer free of electron and hole trapping[25]. Furthermore, the subthreshold swing (SS) is one of the smallest value ever reported. SS is calculated as the slope of the V_G versus $\log(-I_D)$ plot in the region between V_{onset} and the threshold voltage V_T. In the framework of the mobility edge model (see low temperature section), SS can be seen as an image of the width of the trap distribution in the band gap. Consequently, the lower SS, the thinner the trap distribution and the better the OFET. Finally, the contact resistance, evaluated by the TLM technique developed in chapter II, is around 15 kΩ. This number is perfectly negligible since in worst case the term $R_C I_D$ is 0.05 V which is about 1 % of $V_D = 4$ V.

μ_{WEB} ($cm^2 V^{-1} s^{-1}$)	V_{onset} (V)	SS ($V A^{-1}$)	I_{ON}/I_{OFF}	R_C (kΩ)
5.5 X 10^{-2}	-1	1.55	10^6	15

Table 2 OFETs parameters for the web of P34T nanofibers of Figure 3- 11. Surface coverage is 9%.

The standard equations to extract the field-effect mobility μ for the web of nanofibers have to be adapted for the channel geometry since only a small fraction of it is covered by the NFs. For this, we use an image processing software to measure the fraction of the channel which is effectively covered by the nanofibers. This variable is called the surface coverage, *SC*:

$$I_D = \frac{\mu_{WEB}.W.C_0}{L}.(V_D - R_C I_D).(V_G - V_T).SC$$

The surface coverage of Figure 3- 11 is about 9 % which leads to a web mobility of $\mu_{WEB} = 5.5$ X 10^{-2} cm^2 V^{-1} s^{-1}. Surprisingly, μ_{WEB} is one order of magnitude higher than the mobility in a film of NFs (5 X 10^{-2} cm^2 V^{-1} s^{-1} compared to 3 X 10^{-3} cm^2 V^{-1} s^{-1}). To understand the origin of this discrepancy, we have prepared layers with different surface coverage by changing the dispersion concentration (from 0.005 to 0.4 wt%).

3.4.2. From web of nanofibers to film of nanofibers

As seen in Figure 3- 12, the surface coverage is progressively increased. For all the layers, we have performed OFETs measurements from which the OFETs parameters are extracted and reported in Table 3.

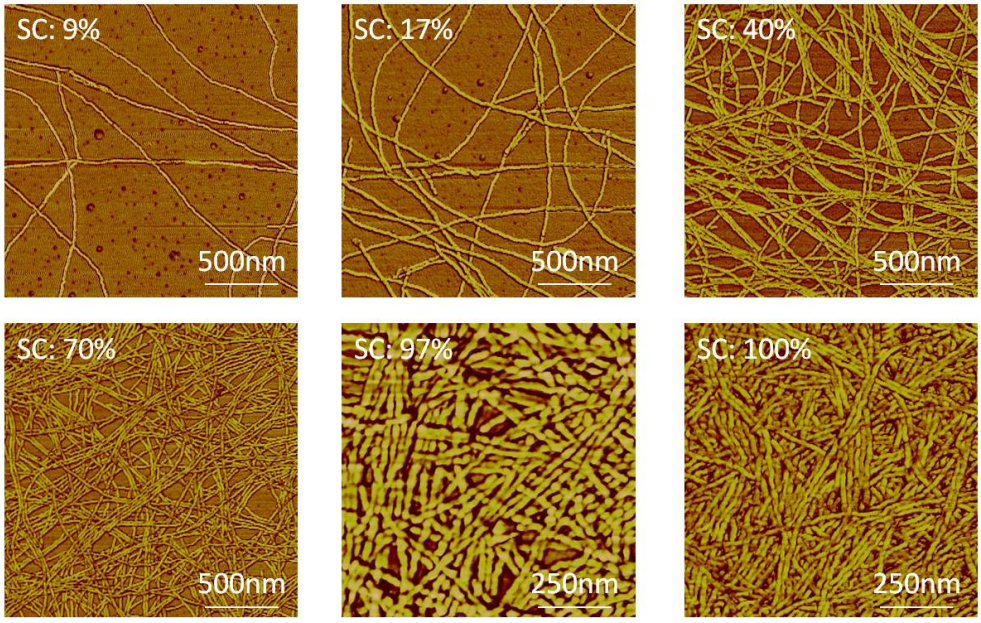

Figure 3- 12 AFM phase images for different surface coverage of P34T nanofibers on SiO_2.

SC (%)	μ_{WEB} (10^{-3} $cm^2V^{-1}s^{-1}$)	V_{onset} (V)	V_T (V)	$(V_{onset} - V_T)$ (V)	*SS* (V A^{-1})	I_{OFF} (A)
9	59 ± 7	0 ± 2	-2 ± 2	2 ± 1	1.6 ± 0.1	10^{-11}
14	58 ± 7	3 ± 1	1 ± 1	2 ± 1	1.7 ± 0.1	10^{-11}
17	55 ± 6	3 ± 1	1 ± 1	2 ± 1	1.7 ± 0.1	10^{-11}
30	41 ± 5	3.5 ± 1	0.5 ± 0.5	3 ± 1	2.3 ± 0.15	10^{-10}
40	25 ± 3	3.5 ± 1	0.5 ± 0.5	3 ± 1	2.3 ± 0.15	10^{-10}
55	13 ± 2	7 ± 1	1.5 ± 0.5	5.5 ± 0.5	3.0 ± 0.2	10^{-10}
70	8.1 ± 0.9	7 ± 1	1.5 ± 0.5	5.5 ± 0.5	3.1 ± 0.2	10^{-10}
92	5.9 ± 0.7	12 ± 5	4 ± 4	8 ± 2	3.3 ± 0.7	10^{-10}
97	6.2 ± 0.7	12 ± 5	4 ± 4	8 ± 2	3.3 ± 0.7	10^{-10}
100	3.8 ± 0.4	26 ± 9	6 ± 8	20 ± 2	5.1 ± 0.9	10^{-9}

Table 3 OFETs parameters for web of P34T NFs with varying *SC* and for the film of P34T NFs.

Several points are observed in Table 3:

1. The mobility μ decreases by more than one order of magnitude when the surface coverage is increased. This is also plotted in Figure 3- 13C.
2. The onset and threshold voltages are shifted towards positive gate voltage when the surface coverage is increased. In chapter II, we have thoroughly explained that a right shift of the threshold voltage is explained by the presence of trapped electrons in the semiconducting layer.
3. The difference between the onset and threshold voltages increases at high surface coverage (see Figure 3- 13B). It means that, when the *SC* is increased, more and more trap states have to be filled by holes until the mobility becomes carrier concentration independent.
4. The same observation is done for the subthreshold swing (see Figure 3- 13B). The subthreshold swing is the slope of the V_G versus $\log(-I_D)$ plot in the region between V_{onset} and the threshold voltage V_T. Therefore this is the inverse of the slopes seen in Figure 3- 13A where it is clearly observed that the subthreshold swing increases with *SC*. Actually, point 3 and point 4 are a common observation: they both mean that more and more trap states have to be filled (by the holes) if the *SC* is increased.
5. The offset current I_{OFF} is getting higher as the surface coverage is increased as observed on the right extremity of Figure 3- 13A. At high positive gate voltage no current is expected because the holes are repelled from the polymer layer by electrostatic forces. The presence of I_{OFF} means that there is as a residual hole current. We think that these residual holes are attracted in the layer by the trapped electrons of point 2.

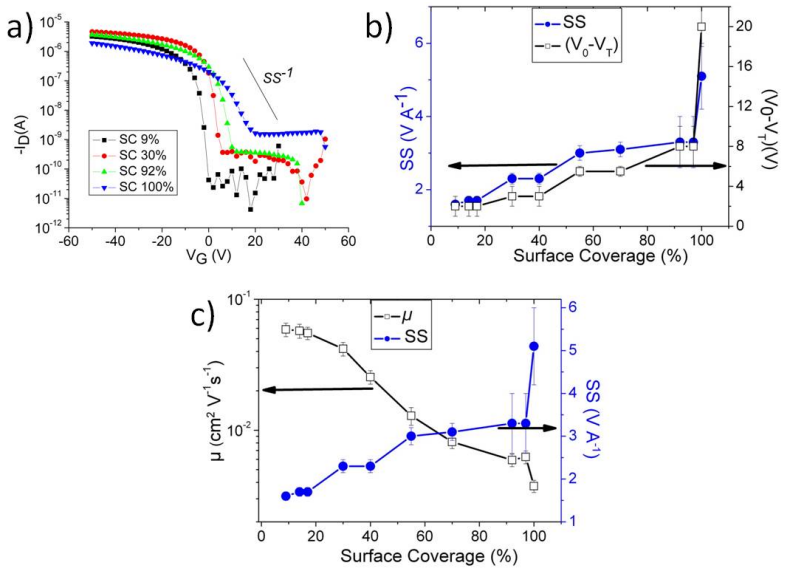

Figure 3- 13 a) Transfer characteristics at several *SC* in the log-lin scales. b) Subthreshold swing and onset and threshold voltages differences increases when *SC* is increased. The two curves perfectly correlates. c) Field-effect mobility decreases as *SC* is increased.

In other words, all the points observed above indicate that the difference in mobility between a web and a film of NFs is most likely explained by an increased concentration of holes and electrons trapping in the polymer layers when the surface coverage is increased. The discussion on the morphological origins for these traps will be made in chapter VIII because measurements obtained at low temperature (chapter IV) and measurements obtained at the nanoscale (chapter VII) will bring additional information.

3.5. Technical details

Film preparation for section 3.2.:

Nanofiber films are spin-coated on OFETs substrates (SiO_2 dielectric) after stirring for several days at room temperature at 1000 rpm (acceleration 500 rpm s^{-1}). For flipped films, nanofiber films are spin-coated at 500 rpm (350 rpm for P38T and P39T) to get thicker films. NF dispersions concentrations are 0.4 % in o-chlorotoluene for P34T, 0.5 % in p-xylene for P35T, 0.6 % in p-xylene for P36T, 0.4 % in pinane for P38T and 0.5 % in pinane for P39T. See chapter I for the material parameters.

Chlorobenzene films: Polymers are dissolved in chlorobenzene (1 or 2 wt%) at 120 °C and filtered through a 0.45 µm pore size PTFE filter. To make sure that all the polymer solutions are completely dissolved and free from colloidal precipitates, the solutions are heated at 120 °C for at least 15 min, then cooled down at 50 °C (only 90 °C for P34T to prevent aggregation) and spin-coated at 2000 rpm on SiO_2 (for both air and buried interfaces). See chapter I for the material parameters.

Layer preparation for section 3.3.: See section 3.2. for the films and section 3.4 for the webs.

Film preparation for section 3.4.: All the webs of P34T nanofibers were obtained by spin-coating (1000 rpm) on the OFETs substrates (SiO_2 dielectric). Similar results were obtained by drop-casting. Images of Figure 3- 12 were obtained from dispersions concentrations of 0.005%, 0.01%, 0.025%, 0.05%, 0.1% and 0.4%. See chapter I for the material parameters.

[1] Z. Bao et al., *Appl. Phys. Lett*. **1996**, 69, 4108.
[2] S. Hugger et al., *Colloid Polym Sci* **2004**, 282, 932-938.
[3] M. Surin et al., *J. Appl. Phys*. **2006**, 100, 033712.
[4] J.F. Chang et al., *Chem. Mater* **2004,** 16, 4772-4776.
[5] H. Yang et al., *Adv. Funct. Mater.* **2005**, 15, 671-676.
[6] A. Zen et al., *Jpn. J. Appl. Phys.* **2005**, 44, 6A, 3721-3727.
[7] S. Cho et al., *J. Appl. Phys*. **2006**, 100, 114503.
[8] R. Zhang et al., *J. Am. Chem. Soc.* **2006**, 128, 3480-3481.
[9] R.J. Kline et al., *Macromolecules* **2005**, 38, 3312-3319.
[10] A. Zen et al., *Adv. Funct. Mater.* **2004**, 14, 757-764.
[11] H. Sirringhaus et al., *Nature* **1999**, 401, 685-688.
[12] This chapter section is part of W.D. Oosterbaan et al., *Adv. Funct. Mater*. **2010**, 5, 792-802.
[13] Y.D. Park et al., *Org. Elec.* **2006**, 7, 514-520.
[14] K. Kaneto et al., *Jpn. J. Appl. Phys.* **2000**, 39, L872-L874.
[15] A. Babel et al., *Synth. Met.* **2005**, 148, 169-173.
[16] W.D. Oosterbaan et al., *Adv. Funct. Mater*. **2010**, 5, 792-802.
[17] J.-F. Chang et al., *Phys. Rev. B* **2006**, 74, 115318.

[18] L.L. Chua et al., *Langmuir* **2006**, 22, 8587.
[19] C. Tanase et al., *Org. Elec.* **2003**, 4, 33-37.
[20] W.D. Oosterbaan et al., to be submitted, see publication list.
[21] L.L. Chua et al., *Nature* **2005**, 434, 194.
[22] C.D. Dimitrakopoulos et al., *Adv. Mater.* **2002**, 14, 2, 99-117.
[23] Not written in the thesis but can be found in A. Gadisa et al., *Adv. Funct. Mater.* **2009**, 19, 3300. (see publication list).
[24] Surface energy is the amount of work needed to bring material from bulk to surface. It is always higher for metals than for polymers because metallic bonds are stronger than Van der Waals forces.
[25] J.-C. Bolsée and J.V. Manca, *Synth. Met.* **2011**, 161, 789-793.

Wire bonder? Just devil's invention

Chapter IV:
OFETs - Low temperature

In this chapter, we perform OFET-measurements at low temperatures in the range of 80-380 K. Temperature dependent experiments are essential if we want to give an insight on the charge transport mechanisms. We discuss the results using the mobility edge model, that we present in detail, and extract some charge transport parameters.

4.1. Results

Like for inorganic semiconductors, investigations at low temperature bring meaningful and valuable information on the charge transport mechanisms occurring in the layer. Because of the difficulty and fragility of the experiments (e.g. due to wire bonding), low temperature measurements were restricted to only three devices from which we expect different behaviors: a web of P34T NFs (surface coverage 25%), a film of P34T NFs and a P34T chlorobenzene processed film. The transfer characteristics are shown in Figure 4- 1. The measurements were performed according to the methods and recommendations described in chapter II.

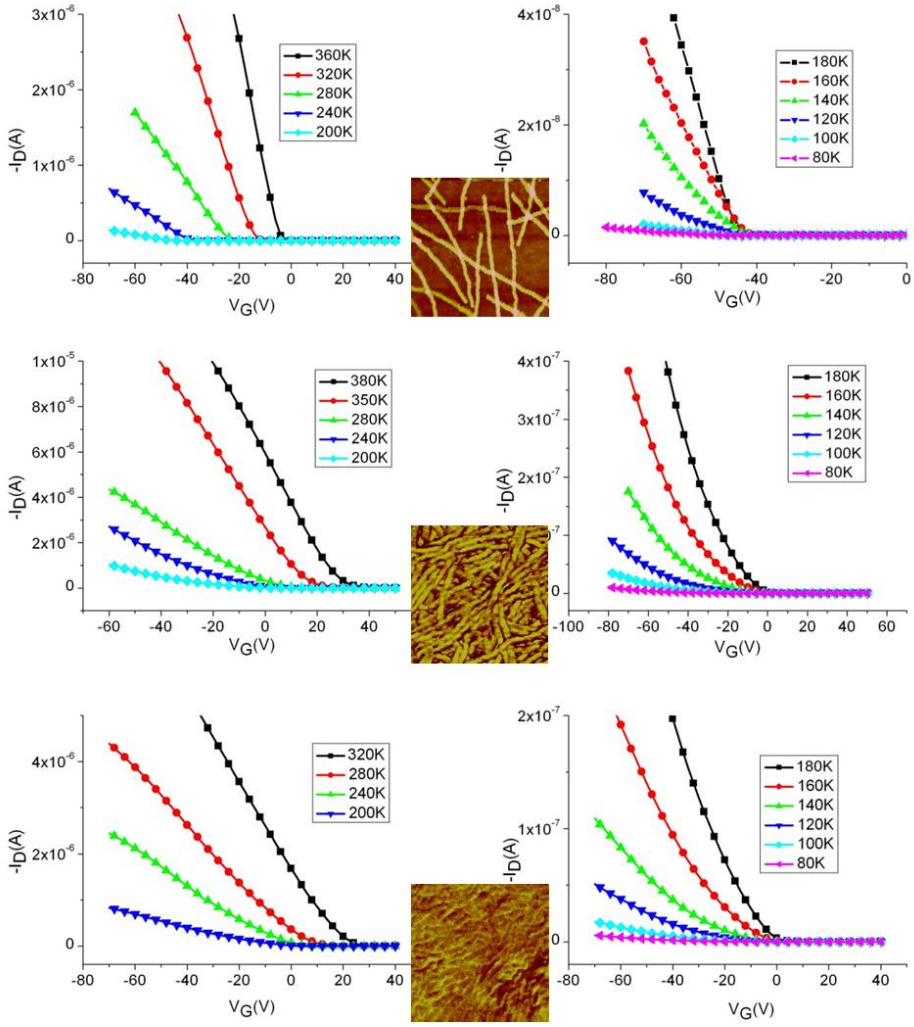

Figure 4- 1 Transfer characteristics as a function of temperature for a web of NFs, a film of NFs and a CB processed film.

From these transfer characteristics, the linear mobility is calculated by using the concept of the "effective mobility"[1,2,3]

$$\mu_{eff} = \frac{I_D}{C_0(V_G - V_{onset}^0)V_D} \cdot \frac{L}{W}$$

Where V_{onset}^0 is the onset voltage at room temperature (before cooling down not after the temperature cyclus). In Figure 4- 1, we observe that the onset voltage shifts to the left (negative gate voltage) when

the temperature is decreased. This is because the thermal energy of charge carriers is reduced and consequently more charges are trapped. The particularity in the calculation of the effective mobility is that the temperature dependence of V_{onset} is taken into account. In this way, in the description of μ_{eff} all the mobile and immobile carriers are included. The conventional description of the mobility (the one which was described in chapter II and used in the other parts of the thesis) is based on the slope of the transfer curves $\mu = \frac{L}{WC_0V_D} . \frac{\partial I_D}{\partial V_G}$. This mobility, sometimes noted as μ_{TFT} for thin film transistor in the literature, takes only the mobile carriers into account. At high temperature and high gate voltage $\mu_{TFT} \sim \mu_{eff}$ while at low temperature $\mu_{TFT} > \mu_{eff}$ since the transfer characteristics become superlinear and therefore more charges are trapped. The calculated effective mobilities are shown in Figure 4- 2 which clearly indicates that the transport is thermally activated with a gate voltage dependent activation energy (in the 200-300 K domain) close to 80-110 meV which is typical for P3HT[4,5] .

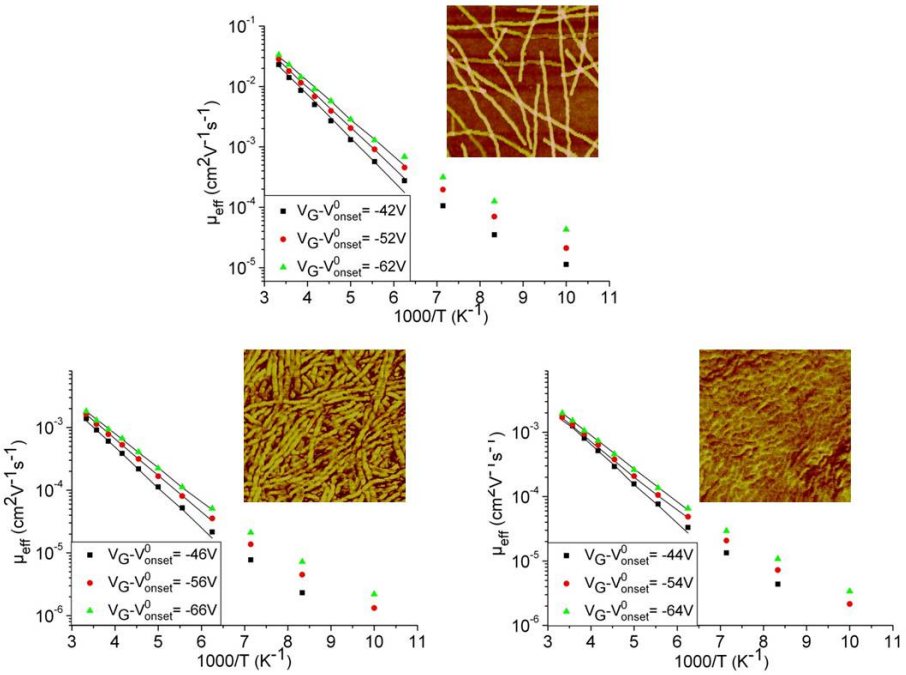

Figure 4- 2 Effective mobility as a function of the temperature and gate voltage V_G for three different samples: web of nanofibers, film of nanofibers and chlorobenzene film, all from P34T. Points are measured data and lines are fit to the ME model.

These plots contain a lot of information. In order to analyze them properly, it is necessary to proceed step by step. First, we will discuss the features common to three sample then, later in the text, we will point out the differences between each layers and extract some material parameters. For each plot of Figure 4- 2, we observe that:

- μ decreases as T is decreased (this is valid for each V_G).
- μ increases as $|V_G|$ is increased (especially at low T).

These dependencies are usual for organic semiconductors and have been routinely reported[6,7,8]. However, the physical reasons for these trends are, to our opinion, not always perfectly understood. In the next section, we describe them in the framework of the mobility edge (ME) model[1, 2]. It is very interesting to notice that for inorganic semiconductors like Si the temperature dependencies are completely different: μ decreases with increasing T due to increased phonon scattering and μ is charge carrier independent.

4.2. Mobility edge model

The mobility edge model has been successfully applied to semi-crystalline polymers which are composed of ordered crystalline domains surrounded by amorphous grain boundaries[1,2] and thus is perfectly applicable to the CB and NFs films studied in the thesis. The model stipulates that in the crystallites the holes can move in delocalized bands whereas in the amorphous matrix they are trapped in localized states. We will show that this model fits reasonably our data. Figure 4- 3 illustrates the salient points of the model.

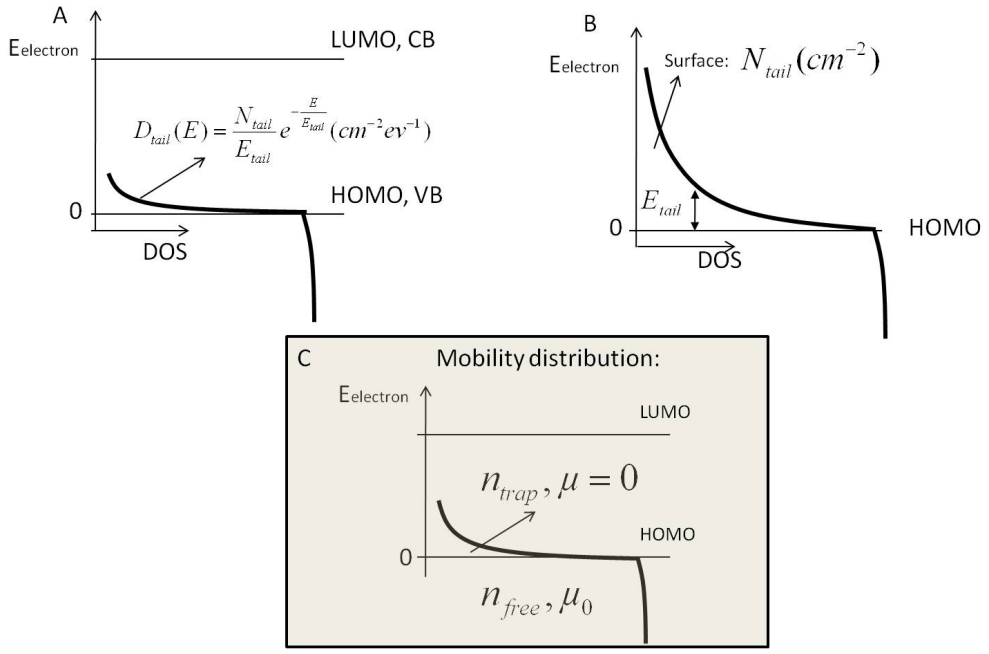

Figure 4- 3 Description of the mobility edge model. A: schematic of the density of states (DOS): exponential shape for the localized states in the bandgap and nearly flat in the valence band. B: zoom of A: E_{tail} is the width of the trap distribution and N_{tail} is the total concentration of trap states. C: the mobility is assumed to be zero in the localized states and constant (μ_0) in the band states.

The density of shallow localized states $D_{tail}(E)$ in the bandgap follows an exponential decreasing law:

$$D_{tail}(E) = \frac{N_{tail}}{E_{tail}} \cdot e^{-\frac{E}{E_{tail}}} \quad (1)$$

Where N_{tail} is the total concentration of trap states and E_{tail} is the width of the exponential trap distribution. The exponential shape can be justified as an approximation of the tail of the Gaussian distribution generally accepted for organic semiconductors[1]. It has been successfully applied to describe the conductivity temperature dependence in other disordered systems such as hydrogenated amorphous silicon[9,10]. The shape of the DOS in the band is unknown but might be assumed to be $\sim\sqrt{E}$ like for a free electron gas in three dimensions[1] or to stay constant with E. The beauty of the model lies in the simple mobility distribution: the charges in the localized states are trapped, hence μ = 0, while the charges in the band are delocalized with a constant mobility μ_0. We call n_{trap} the concentration of charges being trapped in the bandgap and n_{free} the concentration of charges being free in the band. The total concentration of charges is of course the sum of both: $n_{total} = n_{trap} + n_{free}$. Moreover, the mobility edge model stipulates that the effective mobility is proportional to the amount of free charges:

$$\mu_{eff} = \mu_0 \cdot \frac{n_{free}}{n_{total}} \quad (2)$$

This simple model can explain the gate voltage and temperature dependence of the mobility as shown in the next two paragraphs.

4.2.1. Dependence of μ on V_G at fixed T

As explained in chapter II, OFETs have the very interesting property of modulating the charge carrier concentration in the polymer just by changing the gate voltage:

$$n_{total} = \frac{C_0}{e} \cdot |V_G - V_{onset}^0| \quad (3)$$

We remind that e is the electron charge, C_0 is the gate capacitance per unit area and V_{onset} is the onset voltage at which conduction starts. Since we have to do with holes conduction (not electrons), then V_G is swept in the negative region. Consider the initial situation with $V_G = V_{G1}$ at fixed temperature, see Figure 4- 4A. The concentration of charge is then $n_{total} = C_0/e\,|V_{G1} - V_{onset}^0|$. Exactly like it is for inorganic semiconductors, n_{total} obeys to the Fermi statistics:

$$n_{total} = \int_{-\infty}^{+\infty} DOS(E) \cdot \frac{1}{1+e^{\frac{(E_F-E)}{kT}}} dE \quad (4)$$

Where E is the electron energy, E_F is the Fermi energy and k the Boltzmann's constant. In Figure 4- 4A, the Fermi level is positioned inside the bandgap. The Fermi level is positioned in such a way that equation (4) is satisfied while n_{total} is fixed by equation (3). We see in Figure 4- 4A that

n_{total} is split in n_{trap} (blue zone) and n_{free} (red zone):

$$n_{trap} = \int_0^{+\infty} DOS(E) \cdot \frac{1}{1+e^{\frac{(E_F-E)}{kT}}} dE; \quad n_{free} = \int_{-\infty}^{0} DOS(E) \cdot \frac{1}{1+e^{\frac{(E_F-E)}{kT}}} dE. \quad (5)$$

When the gate voltage is decreased to V_{G2} (see drawing B in Figure 4- 4) according to (3) n_{total} is increased (compare both grey zones) and according to (4) the Fermi level E_F has to be pushed towards the HOMO level. This has the consequence that the fraction of free charge is considerably increased (compare both areas) which in turn increases the effective mobility according to (2): $\mu_{eff}(V_{G2}) > \mu_{eff}(V_{G1})$. Then the gate voltage dependence of μ is explained.

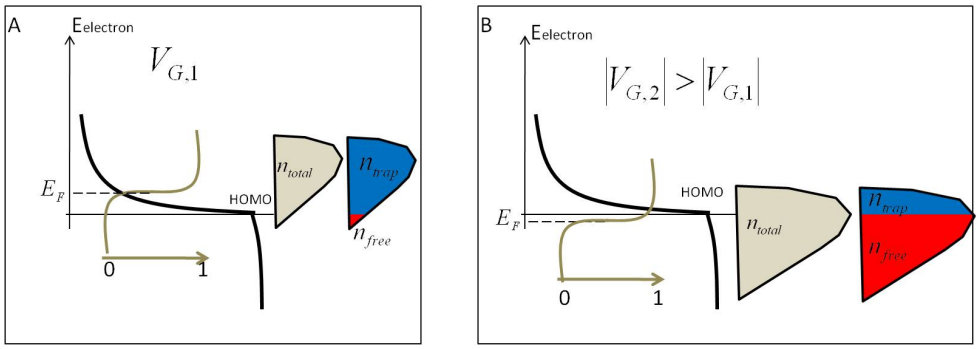

Figure 4- 4 Influence of gate voltage on ratio of free and trapped charge concentrations. A: situation for V_{G1}. B: When V_G is changed to V_{G2}, the Fermi level moves towards the band edge.

4.2.2. Dependence of μ on T at fixed V_G

Now, we work at fixed gate voltage and thus at fixed n_{total}. We consider the situation at temperature T_1, see drawing of Figure 4- 5A. Again, the Fermi level is positioned in order to satisfy (4). The effective mobility is proportional to the free holes concentration (red area). If the temperature is reduced to T_2, the Fermi distribution function[11] becomes more "square", see drawing B (in the previous section the Fermi function stayed unchanged due to a fixed temperature). Physically speaking, it means that the thermal energy of the holes is reduced and thus that the probability of having an available state below the Fermi energy occupied by a hole is reduced. In order to keep n_{total} constant (both grey zones are equal), the Fermi level E_F has to move toward the band edge since the Fermi function is more "square". Nevertheless, the big majority of filled states are above E_F and therefore n_{free} is very small for T_2 which leads to a decrease of the effective mobility: $\mu_{eff}(T_1) > \mu_{eff}(T_2)$. Then the temperature dependence of μ is explained.

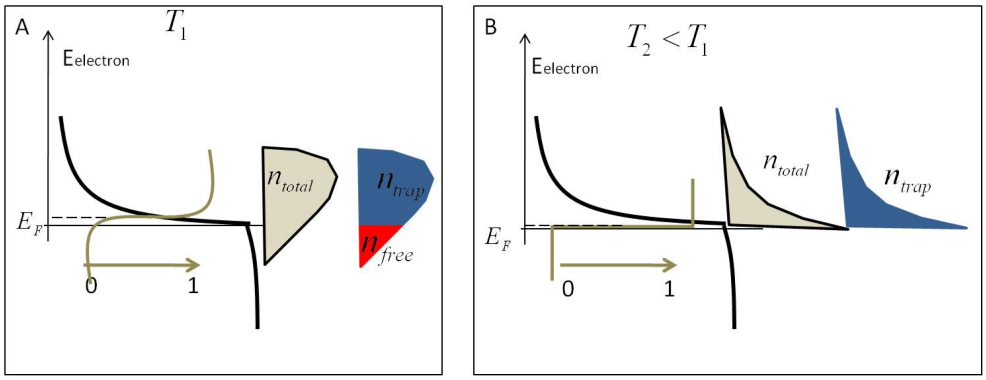

Figure 4- 5 Influence of temperature on ratio of free and trapped charge concentrations. A: situation for T_1. B: when T is decreased to T_2, the Fermi distribution becomes more "square" and in order to keep the charge concentration constant the Fermi level has to move towards the band edge. Despite the Fermi level shift, n_{free} is considerably reduced (almost zero).

4.3. Application to our samples

In this paragraph, we apply the mobility edge model to the data of Figure 4- 2. The model offers three free parameters (width of trap states distribution E_{tail}, trap states concentration N_{tail} and band mobility μ_0) to fit the calculated effective mobilities at various gate voltage and temperature $\mu_{eff}(V_G, T)$. We wrote an algorithm (using Maple 12.0) which does the following. Consider a fixed gate voltage and temperature (V_G^* T^*). The total concentration of charges is calculated with (3). Then, the Fermi energy E_F is obtained by solving (4). Knowing E_F, we calculate the free and trapped fractions using (5) and finally $\mu_{eff}(V_G, T)$ is obtained with (2) and compared with the measured values. The fitted parameters are reported in Table 1 while the fitted and measured mobilities are compared in Figure 4-2. The points below 180 K were intentionally excluded from the fits. In this range, the temperature dependence of the mobility is too weak to be explained by a simple activation behavior. In the 180-300 K range, the fits are acceptable.

	Web of nanofibers	Film of nanofibers	CB film
E_{tail} (meV)	50	55	50
N_{tail} (cm^{-2})	6.5 X 10^{13}	4 X 10^{13}	4.35 X 10^{13}
μ_0 (cm^2 V^{-1} s^{-1})	1.35	0.07	0.065

Table 1 Mobility edge model parameters for web of nanofibers (*SC* 25%), films of nanofibers and CB film. All from P34T.

The main discrepancy between the web and both films is the difference by a factor 20 for the band mobility μ_0. Physically, μ_0 represents the mobility in crystalline regions. Then, the factor 20 difference between the web and films of nanofibers is quite surprising since final morphologies are both made up of the same crystalline nanofibers. However, as already pointed out by Wang et al.[12], we have noticed that μ_0 is strongly dependent on the DOS in the band (noted as N_{VB}, VB stands for Valence Band) while

the trap distribution is relatively insensitive to reasonable variations in N_{VB}. Here, we use a constant DOS $N_{VB} = N_{tail}/E_{tail}$ which is equal to the density of localized states at the band edge (equation (1) for $E = 0$). But there are still some discussions on the shape of the DOS in the band: some authors use a DOS $\sim\sqrt{E}$ [1,3] with different prefactors while others use a flat DOS[2,12] but with varying values. In other words, the choice of N_{VB} is still subject to discussions and therefore can considerably impact μ_0.

We see also in Table 1 that the parameters of the trap distribution (E_{tail} and N_{tail}) are very similar for the three layers. This result was not expected for two reasons. (1) We have observed in chapter III that the subthreshold swings of a web of NFs and a film of NFs are very different (from 2.2-2.4 for the web with a surface coverage of 25 % to 5.1 for the film). (2) When we observe carefully Figure 4- 1, it is noticed that the behavior of the web of NFs is different to the films (NFs and CB) behaviors: the transfer characteristics are straighter for the web. At high temperature (T>200 K), this is seen nearby the onset voltage (start of conduction) while at low temperature (T<200 K) this is more evident. The explanation for this contradiction comes from the trap distribution of equation (1) which contains only one shallow exponential distribution. This model is too simple to account for the reality: we were unable to fit the very first data nearby the onset voltage, that is why on Figure 4- 2 there is no fit for points with $\left|V_G - V_{onset}^0\right|$ smaller than 42 V. A bimodal distribution of deep and shallow donor-like trap states (hence two exponential distributions) has been used in the literature to explain low temperature measurements in the early subthreshold region[3,8] :

$$D_{tail}(E) = \frac{N_{tail}}{E_{tail}} \cdot e^{-\frac{E}{E_{tail}}} \quad 0 < E < E^*$$

$$D_{deep}(E) = \frac{N_{tail}}{E_{tail}} \cdot e^{-\frac{E^*}{E_{tail}}} \cdot e^{-\frac{(E-E^*)}{E_{deep}}} \quad E > E^*$$

Where D_{tail}, D_{deep} are the shallow and deep trap states distributions, E_{tail}, E_{deep} are the widths of the shallow and deep exponential distributions, N_{tail} is the concentration of shallow states and E^* is the energy separating the two distributions. Figure 4- 6 depicts the trap distribution in the bandgap when the tail distribution is the one for the film of NFs in Table 1 and the deep distribution has the following parameters: E_{deep}= 250 meV, E^*= 250 meV. Chang et al.[3] proved that the use of deep states allows a more accurate description of the subthreshold voltage behavior. Moreover, they showed that the shape of the shallow distribution is not influenced by the inclusion of the deep distribution in the model. Therefore, we argue that webs of NFs have a narrower deep trap states distribution than the films which explain the lower subthreshold swings and apparent straighter FET curves for the webs of NFs and that the three layers have a very similar shallow trap states distribution as found out in Table 1. In chapter VIII and particularly in Figure 8-4, we will further discuss this point.

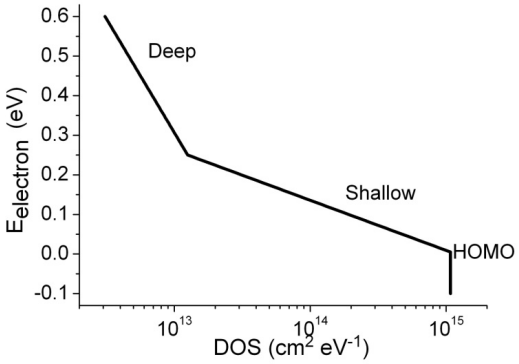

Figure 4- 6 Localized states in the bandgap might be represented by two exponential distributions.

We have not tried to fit this upgraded model because our subthreshold voltage data suffer strongly from the fact that measurements are not performed with a pulsed bias but with a DC bias. Indeed, DC bias induces permanently holes in the channel with a part of them being trapped. The problem is that the holes are not released as fast as they are trapped and thus the amount of trapped charge (noted as p_{trap} in chapter II) is increased. In the literature, this effect is referred to as bias stress effect. As largely explained in chapter II, p_{trap} shifts the transfer characteristic towards negative voltage and thus is superposed to the same shift caused by the decrease in temperature. Consequently, it is highly recommended to use pulsed bias (in place of DC bias) in order to minimize the bias stress effects. We note that these bias stress effect were not too detrimental for models with only one tail distribution like we did.

4.4. Technical details

A system available in the laboratory was adapted for the low temperature OFET measurements, see Figure 4- 7. The vacuum unit (down to 10^{-7}mbar) consists of a turbomolecular pump in series with a rotary vane primary pump. A temperature control unit from Oxford instruments drives a heater to stabilize the sample to a temperature fixed by the operator (80-450 K). The measurements are computer controlled via Labview programs and two measurement units (Keithley 2400).

We used the same OFETs substrates and samples processing conditions as in chapter III. OFETs samples were wire bounded (very critical and delicate operation!) to a dedicated low temperature and high vacuum sample holder. OFETs measurements were performed after one night at high vacuum (10^{-7} mbar) in order to outgas the residual solvent, humidity and oxygen gas. Displayed data were obtained during the cooling down (from 300 K to 80 K) with a step resolution of 20 K. Measurements were performed in the linear regime and according to the methods described in chapter II.

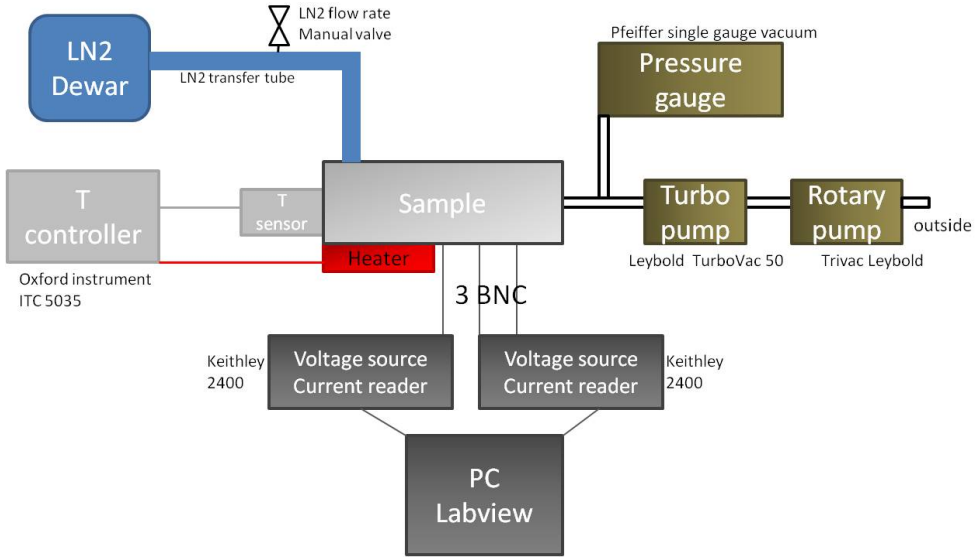

Figure 4- 7 Low temperature set-up.

[1] A. Salleo et al., *Phys. Rev. B* **2004**, 70, 115311.
[2] R.A. Street et al., *Phys. Rev. B* **2005**, 71, 165202.
[3] J-F Chang et al., *Phys. Rev. B* **2007**, 76, 205204.
[4] J.A. Merlo and C.D. Frisbie, *J. Phys. Chem. B* **2004**, 108, 19169-19179.
[5] L.H. Jimison et al., *Adv. Mater.* **2009**, 21, 1568-1572.
[6] G. Horowitz et al., *J. Appl. Phys.* **2000**, 87, 9, 4456.
[7] A.R. Volkel et al., *Phys. Rev. B* **2002**, 66, 195336.
[8] J.A. Merlo, C.D. Frisbie, *J. Phys. Chem. B* **2004**, 108, 19169-19179.
[9] M. Shur et al., *J. Appl. Phys.* **1984**, 55, 3831.
[10] R.A. Street et al., *Phys. Rev. B* **1988**, 38, 5603.
[11] The Fermi distribution function gives the probability that a hole (or an electron) fills a state. The function varies between zero (the state is not filled) and one (the state is filled).
[12] C. Wang et al., *Adv. Mater.* **2010**, 22, 697-701.

Success is the ability to go from one failure to another with no loss of enthusiasm
- Sir Winston Churchill -

Chapter V: SPM equipment for investigating organic semiconductors

After the macroscopic analysis of the previous three chapters, we switch now to the nanoscale world. At the nanoscale, two electrical characterization techniques are used in this thesis: Kelvin Probe Force Microscopy (KPFM) and Conductive AFM (CAFM). The first measures the surface voltage at the nanoscale while the second measures the electrical current. They both belong to the family of Scanning Probe Microscopy (SPM). In this chapter, we describe all the equipment required for performing consistent and reliable SPM investigations. In particular, a significant step achieved in this thesis was the construction of a glovebox around the AFM. We describe in detail the construction and the functioning of the glovebox.

5.1. AFM set-up

All the SPM (it includes AFM, CAFM and KPFM) measurements are performed with the Veeco® multimode AFM (Figure 5- 1) equipped with the Nanoscope IIIa controller and the quadrex module. An additional dedicated module is used for CAFM.

Figure 5- 1 Multimode AFM (Veeco® company)

5.2. SPM tips

A key element in SPM investigations is the choice of the probing tip. Table 1 summarizes for each SPM technique the essential parameters of the tips. We see for instance that, because CAFM is performed in contact mode, the CAFM spring constant is low in order to ensure a soft contact to prevent sample degradation or scratching. We see also that AFM tips have no metal coating, since they are used for topography and not for electrical characterizations, which ensures a smaller contact radius and hence a better spatial resolution.

	AFM	CAFM	KPFM
	Tapping mode	Contact mode	First pass: tapping mode Second pass: oscillating mode
Used for	Topography	Current	Voltage
Model from Nanosensors®	PPP-NCH	PPP-CONTPt PPP-CONTAu	PPP-EFM
Metal coating	No	Yes (Au or $PtIr_5$)	Yes ($PtIr_5$)
Nominal resonance frequency	330 kHz	13 kHz	75 kHz
Spring constant	42 Nm^{-1}	0.2 Nm^{-1}	2.8 Nm^{-1}

Table 1 Key parameters of SPM tips purchased from Nanosensors®

5.3. AFM glovebox

To prevent sample contamination from moisture and oxygen present in normal air, electrical measurements on organic semiconductors are routinely performed under inert gas (like Nitrogen)[1]. In our laboratory, we have a commercial (MBraun®) nitrogen filled glovebox which allows to prepare and characterize different kinds of devices such as solar cells, organic light emitting diodes and field-effect transistors in inert atmosphere. However, our AFM is not placed in this glovebox and if we want to perform consistent nanoscale electrical measurements (like CAFM and KPFM) with the AFM a solution needs to be found. Therefore, during the first year of the thesis, it was decided to build a glovebox around the AFM.

Basically, it consists of an aluminum rectangular box (0.7 X 1.3 X 1.8 m^3) with two front and top transparent panels. The dimensions are large enough so that the inclusion of a solar simulator inside the glovebox is possible in the future. The AFM is positioned on an anti-vibration table and is connected to the computer via appropriate flanges and feedthroughs. An antichamber which allows to bring in and out objects from the glovebox is foreseen on the right panel. The frame (including the top and front transparent panels) was fabricated by an external company (Easy Systems®) while the rest (antichamber, flanges, feedthroughs, control system of the pressure) was done by Johnny Baccus and Johan Soogen from University Hasselt.

Figure 5- 2 shows the glovebox under operation (around 2 mbar nitrogen overpressure). Obtaining this glovebox working was a tough challenge. The main issue we have encountered was nitrogen leaking. We spent weeks and weeks in the laboratory basement (the glovebox original location) hunting for leaks around the glovebox. Every corner in the Al frame, every knob on the front panels and the contact with the ground were all source of leaks. Then, the glovebox was moved in a larger room (to facilitate access to the back side) and an anti-permeation carpet was put on the floor. At this moment, things went much better and we could obtain a working glovebox.

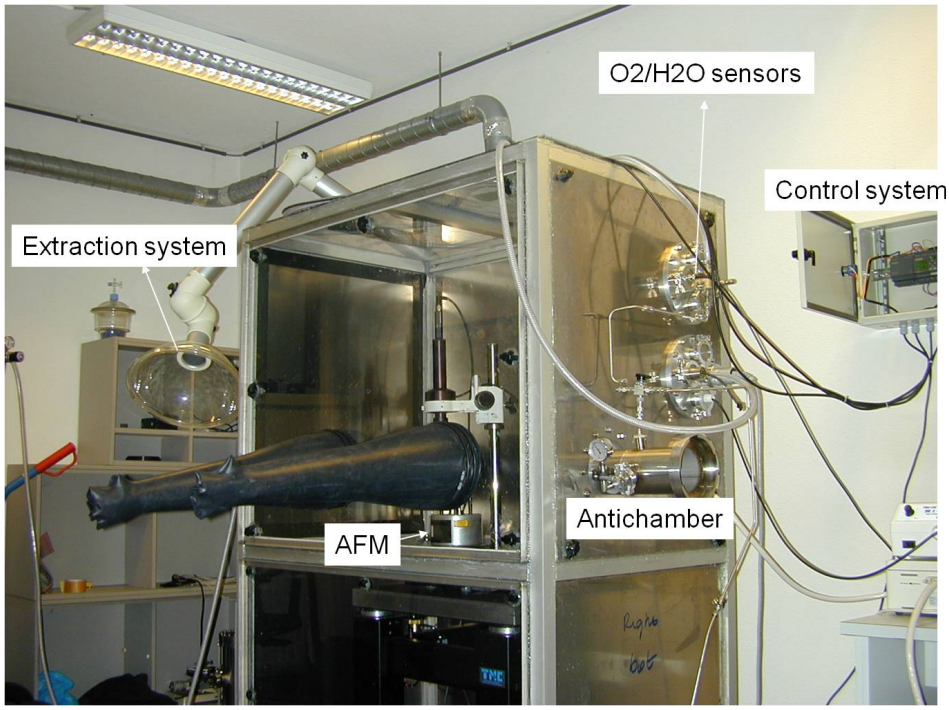

Figure 5- 2 Picture of the AFM home-made glovebox under 2 mbar nitrogen overpressure.

5.3.1. Glovebox description

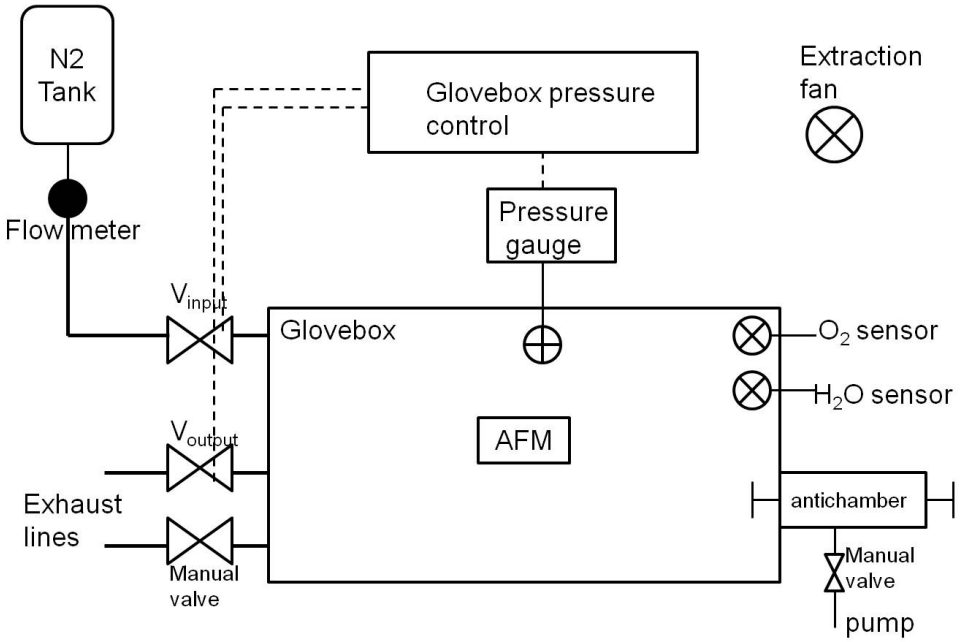

Figure 5- 3 Glovebox schematic flow diagram.

5.3.1.1. Oxygen and humidity sensors

Due to the sensors high cost, it was decided to use, when needed, the available oxygen and humidity sensors from the commercial MBraun® glovebox. A control unit, including the supply voltage and reading subunits, was built for both sensors:

- O_2 sensor: sensing range: 0-1000 ppm, supply voltage 24 V, analog output 0-10 V, sensitivity 10 mV/ppm, response time 10 sec
- H_20 sensor: sensing range: 0-500 ppm, supply voltage 24 V, analog output 0-10 V, sensitivity 20 mV/ppm, response time 120 sec

5.3.1.2. Control of the glovebox pressure

In order to maintain high nitrogen concentration in the glovebox, it is essential to keep the glovebox slightly in overpressure (a few mbars) and thus avoid oxygen and moisture diffusion in the glovebox. For this purpose, a controller from Siemens® is used. The controller monitors the pressure in the box and compares it to user-preselected pressure values to decide whether or not the input and output valves have to be opened or closed. The operators must enter 3 pressure values: p_{low} (typically 0.3 mbar), p_{high} (typically 2 mbar) and p_{max} (typically 3 mbar). Figure 5- 4 shows how the controller works. At the beginning, we consider that the valves V_{input} and V_{output} are closed and that the pressure in the box is between p_{low} and p_{high}. Due to residual leaks, the pressure drops (in a negative exponential way) until it

reaches $p_{low.}$ Then, V_{input} is opened and the pressure rises until p_{high} is reached where V_{input} is closed and a new cyclus can start. If for any reason, the most frequent one being that the operator enters his arm in the glovebox and causes an abrupt pressure jump, the pressure in the box exceeds $p_{max,}$ then V_{output} is opened while V_{input} is kept closed.

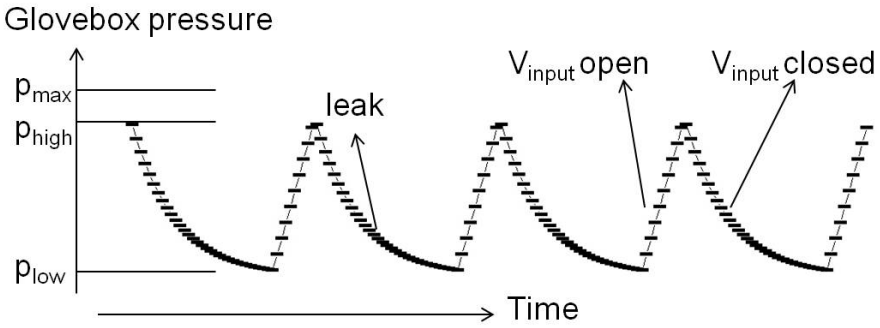

Figure 5- 4 The opening of the input valve is controlled to keep the pressure in the box between p_{low} and p_{high}.

This is what we call the "normal" operation mode where the box is nitrogen filled and measurements can be done. But before this is made possible, the glovebox has to be purged: this is the second mode, the "purge" mode. Here, we open the manual valve and the input valve in such a way that the pressure in the box is constant and that the box is nitrogen flushed. As explained below, the purging time depends on the desired oxygen and moisture levels and the nitrogen flushing rate.

5.3.1.3. Operator security

Excessive and uncontrolled leaking of nitrogen in the local could reduce the ambient air oxygen concentration and lead to health damage for the operator. To ensure operator's security, some rules are followed. (1) An extraction fan near the glovebox is continuously turned on (maximum extracting rate is 27 l s^{-1} which is orders of magnitude higher than the leaking rate. (2) Two oxygen detectors are placed in the AFM room. They track continuously the oxygen level and start beeping if the oxygen levels drop below 19.5% (standard condition is 20.9%).

5.3.2. Performance of the glovebox

While using the glovebox, the standard contamination levels we reached are $[O_2]$ < 50ppm and $[H_2O]$ < 10ppm. Because our glove box has no purification system, no moisture absorber and no internal circulation flow, better contamination levels are impossible to reach. In particular, we cannot avoid small O_2 molecules to backflow inside the glovebox. However, the obtained values represent a huge improvement in comparison with air at 1 atm, relative humidity 50% and 20°C where $[O_2]$ is about 200000 ppm (improvement by a factor 4000) and $[H_20]$ is about 15000 ppm (improvement by a factor 1500).

5.3.3. How to determine the glovebox leak rate?

As explained above, nitrogen leak was the main issue of the glovebox. While hunting for leaks, we have used two methods for evaluating the nitrogen leak rate:

5.3.3.1. Static mode

In this mode, the pressure is kept fixed, V_{input} is open, V_{output} is closed and the nitrogen input flow rate is read at the flow meter (see Figure 5- 3). Due to the law of mass conservation, the leakage rate is equal to the nitrogen input rate. As expected, the leakage rate is increasing with the glovebox pressure:

Pressure (mbar)	0.75	1.55	3.5
Leak rate (l s^{-1})	0.03	0.05	0.08

Table 2 Glovebox leak rate as a function of glovebox overpressure

5.3.3.2. Dynamic mode

The static mode technique is easy to use but has the disadvantage that it does not represent the normal operation mode where the pressure varies between p_{low} and p_{high}. Here, in the dynamic mode, the goal is to calculate the volume of gas which has leaked between the status high pressure and the status low pressure, to divide this volume by the time elapsed between both status to have the average leak rate. To do this, we use the ideal gas law $PV = nRT$ with T the absolute temperature in Kelvin, n the amount of gas in moles and R the gas constant (8.314 $Jmol^{-1}K^{-1}$). To clarify and illustrate the method, we take an example:

- In the high pressure state: $T = 298$ K, $P_{high} = 2.1$ mbar + 1 atm, $V = 1500$ l + 30 l
  Putting everything in the ideal gas law, we obtain $n_{high} = 62.68$ moles. Note that for the evaluation of the volume, we have added 30 liters for the volume of the two gloves which are filled.
- In the low pressure state: $T = 298$ K, $P_{low} = 0.1$ mbar + 1 atm, $V = 1500$ l
  Putting everything in the ideal gas law, we obtain $n_{low} = 61.33$ moles.

So, 1.35 moles of nitrogen have leaked from the glovebox. To what volume does it correspond? Again, we use the ideal gas law: $V_{leak} = \frac{(n_{high} - n_{low})RT}{P_{mean}}$ where P_{mean} is the average pressure value between high and low. We find $V_{leak} = 33$ l. At the same time, we have measured the elapsed time between high and low status (9 min) and we find that the average leak rate is 0.06 l s^{-1}. As expected, we can check that this value is comprised between the extreme values of the static mode table.

5.3.4. How long do we have to purge the glovebox?

Before making any measurements, the glovebox has to be purged, i.e. to flush away the initially present air atmosphere and to replace it by nitrogen. The question is to know how long the box has to be purged in function of the glovebox volume, Vol (calculated equals to 1.5 m^3), nitrogen input flow rate α, initial oxygen concentration $[O_2]_{ini}$ (taken as 20% in this work) and desired oxygen concentration $[O_2]_{fin}$. If we assume that during the purging process the pressure in the glovebox is constant (and

hence the gas mass) then we can write that the oxygen concentration temporal variation is proportional to the oxygen concentration:

$$\frac{\partial[O_2]}{\partial t} = -\frac{\alpha}{Vol}.[O_2]$$

$$[O_2](t) = [O_2]_{ini}.exp^{-\frac{\alpha}{Vol}t} = 0.2\ exp^{-\frac{\alpha}{1.5}t}$$

Or

$$[O_2]_{fin} = 0.2\ exp^{-\frac{\alpha}{1.5}t_{final}}$$

Where t_{final} is the total purging time. We see that the desired oxygen concentration $[O_2]_{fin}$ is only function of the product $\alpha.t_{final}$ which is the total nitrogen volume injected in the box during the purging process. Table 3 gives some examples which can be used by the glovebox operator to predict the purging time.

Desired oxygen concentration , $[O_2]_{fin}$	Total volume of N2 injected	Nitrogen flow rate, α	Purging time, t_{final}
10 ppm	14.85 m^3	10 l min^{-1}	24,7 hours
100 ppm	11.40 m^3	10 l min^{-1}	19 hours
1000 ppm	8 m^3	10 l min^{-1}	13,3 hours

Table 3 Estimation of the purging time needed as a function of the desired oxygen concentration and the nitrogen input flow arte. Nitrogen flow rate is programmable with a flow meter at the outlet of the nitrogen tank.

[1]A. Alexeev, J. Loos, *Org. Elec.* **2008**, 9, 149-154.

I have not failed. I've just found 10,000 ways that won't work.
- Thomas Edison -

Chapter VI: Measuring voltage at nanoscale

In this chapter, we present and describe in detail Kelvin Probe Force Microscopy (KPFM) which allows one to measure the electrical potential of a sample surface at the nanoscale. First of all, the working principle of the technique is described. Then, the technique capabilities are demonstrated on several test samples (voltage difference on external electrodes, solar cell, work function gradient on one sample). Finally, the voltage profile on the nanofibers when biased in OFET structure is investigated.

6.1. Working principle

The name of the Kelvin probe technique comes from William Thomson, better known as Lord Kelvin, who in 1898[1] explained the formation of a built-in potential difference when two different metals with two different work functions are contacted, the so called contact potential difference, CPD. In this experiment, an external voltage is applied between the two metals to nullify the internal electric field. KPFM is based on the same principle as the macroscopic Kelvin experiment: application of an external voltage to nullify the voltage difference between the tip and the sample.

The working principle of KPFM is sketched in Figure 6- 1[2]. The basic idea is to probe the electrostatic force F between two objects, the tip and the sample. If sufficiently close to each others, tip and sample can be considered as a capacitor. In case of a voltage difference ΔV between the tip and the sample, there exists a force which can be written as $F = -{}^{1}/_{2}\,{}^{\partial C}/_{\partial z} \cdot \Delta V^2$ (1), C being the tip-sample capacitance and z the tip-sample distance. The key question is to know how to detect this electrostatic force with an AFM tip. The solution is to apply an oscillating potential $V_{AC}\sin(\omega t)$ to the tip (point 1 Figure 6- 1) in such a way that the tip is successively attracted and repelled by the sample. The trick is that the frequency ω is chosen close to the tip resonance frequency so that the tip cantilever is going to mechanically oscillate in response to the successive electrostatic attraction and repulsion. Consequently, a signal at frequency ω can be detected by the photodiode (point 2 Figure 6- 1). The oscillation amplitude is proportional to the tip-sample voltage difference. An active feedback loop is then activated: a direct current potential V_{DC} is applied to the tip to nullify the electrostatic force at frequency ω, F_ω (point 3 Figure 6- 1). In total, a direct and an alternating voltage components are applied to the tip leading to the following expression: $\Delta V = -V_{DC} + V_{AC}\sin(\omega t) + \Delta\phi/e$ (2) where $\Delta\phi = \phi_{tip} - \phi_{sample}$ is the work function difference between the tip and the sample and e the electron charge. Injecting (2) in (1), we obtain:

$$F = -\frac{1}{2}\frac{\partial C}{\partial z}\left[(\Delta\phi/e - V_{DC})^2 + \frac{V_{AC}^2}{2}\right] - \frac{\partial C}{\partial z}[(\Delta\phi/e - V_{DC})V_{AC}\sin(\omega t)] + \frac{1}{4}\frac{\partial C}{\partial z}[V_{AC}^2\cos(2\omega t)] \quad (3)$$

$$F = F_{DC} + F_{\omega} + F_{2\omega}$$

We see that when the feedback loop tries to nullify F_{ω}, it tunes V_{DC} to the difference in work function $\Delta\phi = \phi_{tip} - \phi_{sample} = V_{DC} \cdot e$. It means that by monitoring V_{DC} it is possible to extract the sample work function if the tip work function is calibrated.

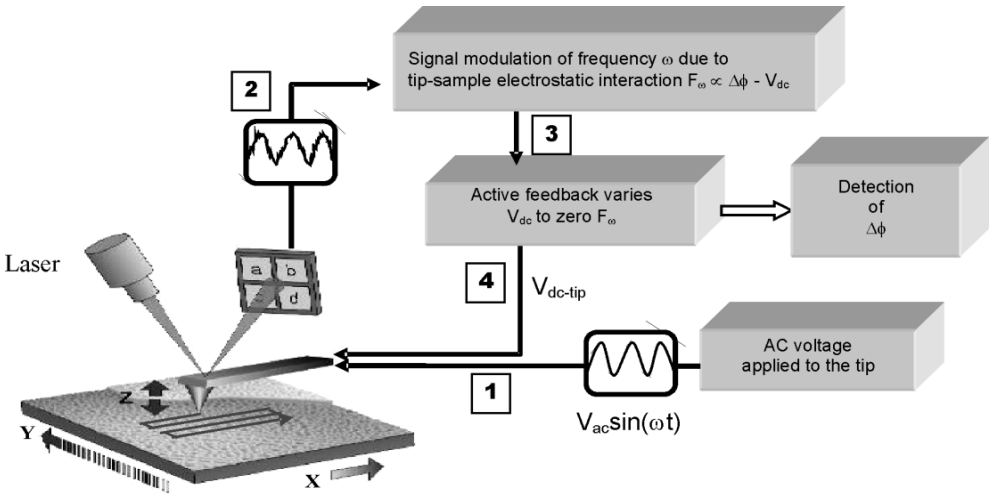

Figure 6- 1 KPFM working principle schematic[2]. See text for explanation.

In order to minimize the influence of the sample topography on the electrostatic response, we have used KPFM in the double pass mode as illustrated in Figure 6- 2. It means that each line on the sample is scanned twice. The first scan (or main scan) is the classic tapping mode scan for measuring the topography. Before the second scan is performed, the KPFM tip is positioned above the sample to a distance defined by the operator and named the lift height. During the second scan, the tip follows the recorded topography in such a way that the tip sample distance is always equals to the lift height and the surface potential is measured.

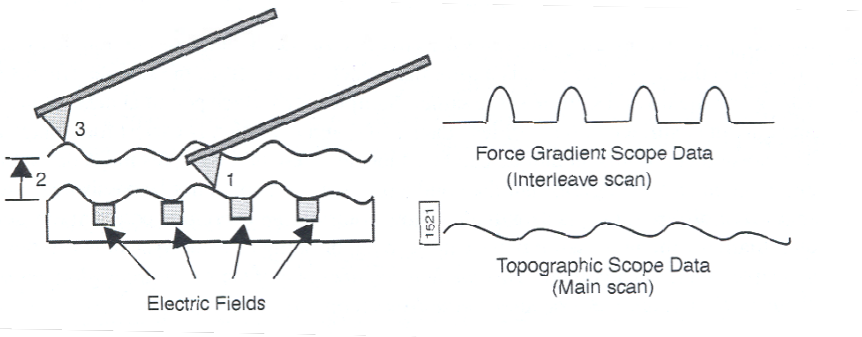

Figure 6- 2 Double pass mode used in KPFM

In summary, the KPFM method we employ is based on the detection and zeroing of the amplitude of the first harmonic component F_ω of the tip sample electrostatic force. In the literature, this is reported as KPFM amplitude modulation (AM) and lift mode. It has to be noted that many other different modes exist, some detect the vertical force gradient $\partial F/\partial z$ by monitoring the frequency modulation (FM) of the tip[3]. While others measure the topography and the surface potential simultaneously (single pass mode) by detecting the amplitude at two different harmonics (first for the topography and second for the potential).

Since KPFM is a non-contact and non-destructive method, it is perfectly appropriate for studying soft materials like organic semiconductors. Moreover, it does not require specific sample preparation like exposure to high electric fields or plasma treatment and it works for conducting and non conducting samples. For all these reasons, KPFM has been frequently used for characterizing organic semiconductors: evaluation of contact resistance in OFETs[4,5,6], monitoring of band bending at a p-n junction[7], charge distribution in an organic solar cell[8,9], charge trapping in OFETs[10,11] and charge transport in OFETs[12]. KPFM has also been intensively applied to inorganic electronic systems like GaN p-n junction[13] or evaluation of samples work function[14].

The main drawback of the KPFM method is the poor lateral resolution[15]. The reason is that KPFM uses the electrostatic force which is proportional to r^{-2} and thus is considered as a long range force for which the undesired contribution of the neighbour pixels vanishes slowly impeding considerably the lateral resolution[16]. It has been demonstrated that the measured potential does not exactly correspond to the surface potential of a given point but rather is a weighted average of all the local potentials on the surface under the tip[16]

$$V_{DC} = \frac{\sum_{i=1}^{n}(C'_{it}V_i)}{\sum_{i=1}^{n}(C'_{it})} \quad (4)$$

Where $V_{DC}$is the voltage applied during the scan (and hence is the KPFM measured voltage), V_i is the surface potential at point i and $C'_{it} = \partial C_{it}/\partial z$ is the z-derivative of the capacitance between the tip and the point i. All the C'_{it} are the weighting factors of the average. In the end, it gives a method with a

lateral resolution of 50-100 nm and a voltage resolution of a few mV. This is in contrast with the standard tapping mode AFM which is based on short range forces (r^{-6}, r^{-12}) giving much better resolution (typically 1 nm).

6.2. Learning the technique on test samples

Before using KPFM on the P3*A*T nanofibers which is the object study of the chapter, we will first show some measurements on samples for which the potential distribution is either expected or either defined by the operator. In this way, the multiple capabilities of the technique and the interpretation of the data, which is never straightforward with KPFM, will be progressively shown.

6.2.1. On external applied voltage

To practice and test KPFM, the simplest sample to use is probably one on which a voltage difference is put by an external voltage supply between two distinct electrodes. In this way, we can easily check whether the set-up is capable of measuring voltage contrast. The device architecture is depicted in Figure 6- 3: two Au fingerlike interdigitated electrodes with a spacing of 2.5 µm, which is small enough to be measured with the AFM piezoelectric scanner, are deposited on a SiO_2 chip. The two microscopic Au electrodes are wire bonded to two macroscopic Cu electrodes on a PCB (printed circuit board). Finally, two ordinary electrical cables are soldered to the Cu and plugged into a voltage supply. The big challenge is to position the two microscopic wire bonding cables and the interdigitated electrodes in such a way that the KPFM tip is not blocked or hindered when approaching the sample. A lot of effort and trials were necessary.

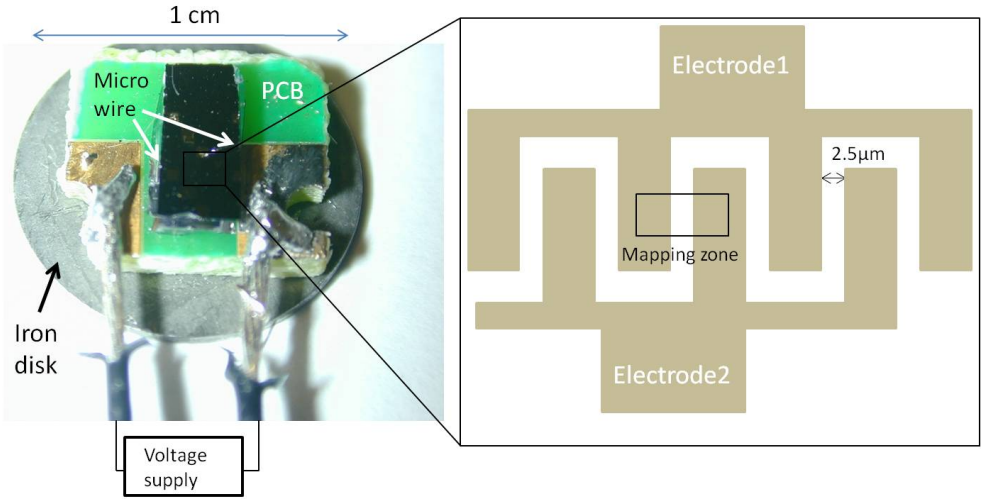

Figure 6- 3 Device architecture used to practice and test KPFM: two electrodes on a chip mounted on a PCB glued on an iron disk. The two micro sized electrodes are wire bonded to the macroscopic copper electrodes which are cables connected to an external supply voltage.

The mapping zone consists in the two electrodes and the channel in between, see topography in Figure 6- 4. On the scope trace, we see that the trace and retrace are perfectly superposed, proof of a stable measurement, and that the channel depth is about 45 nm. On the potential scope trace, we see that, as expected, the potential is constant on both electrodes whereas the variation is linear in the channel. On Figure 6- 4, we measure a potential drop of 3 V while the applied voltage was 4 V. The reason for this mismatch comes from equation (4): when measuring the electrode potential, there is always a detrimental contribution coming from other potentials on the surface. Nevertheless, we have checked that the measured voltage followed the evolution of the applied voltage in the negative and positive domains (range 12 V), we just keep in mind that a correction factor has to be applied if absolute values are needed[17].

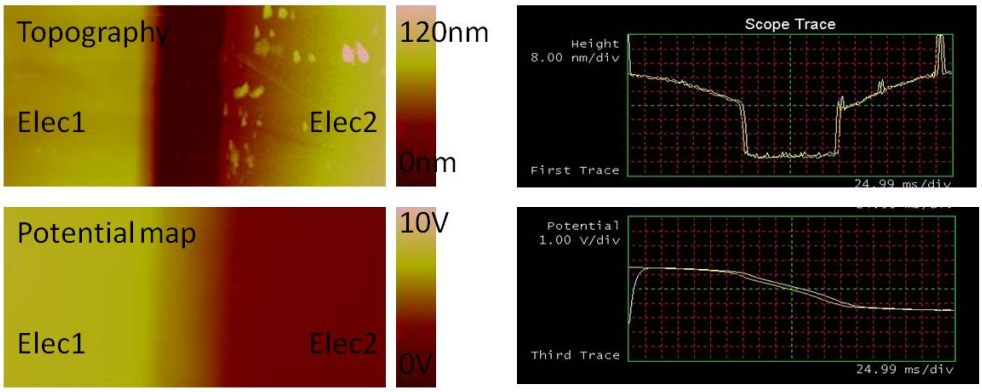

Figure 6- 4 Topography and potential maps and the corresponding line sections (V_{AC} = 6 V, tip height 25 nm).

6.2.2. On organic solar cell

KPFM has been applied several times on the active layer of organic solar cells[8,9,18], the reason being that, for bulk heterojunction solar cell, the active layer is composed of two different materials, one being the electron donor and one being the electron acceptor, which have tendency to phase separate. Since the two materials have distinct electronic properties, i.e. different HOMO and LUMO levels, their surface voltage is expected to be different and a KPFM contrast can be measured. The most relevant solar cell to study with KPFM is probably the one being formed by MDMO-PPV, the donor material, and PCBM, the acceptor material. This is because, if choosing toluene as solvent, the phase separation between both materials is very large, larger than 200 nm as confirmed by Figure 6- 5, which facilitate considerably KPFM measurements (remind that KPFM lateral resolution is not better than 50-100 nm). Even if giving bad performance, due to the large phase separation, the MDMO-PPV:PCBM solar cell has been intensively studied and is become a standard model system for studying organic solar cell.

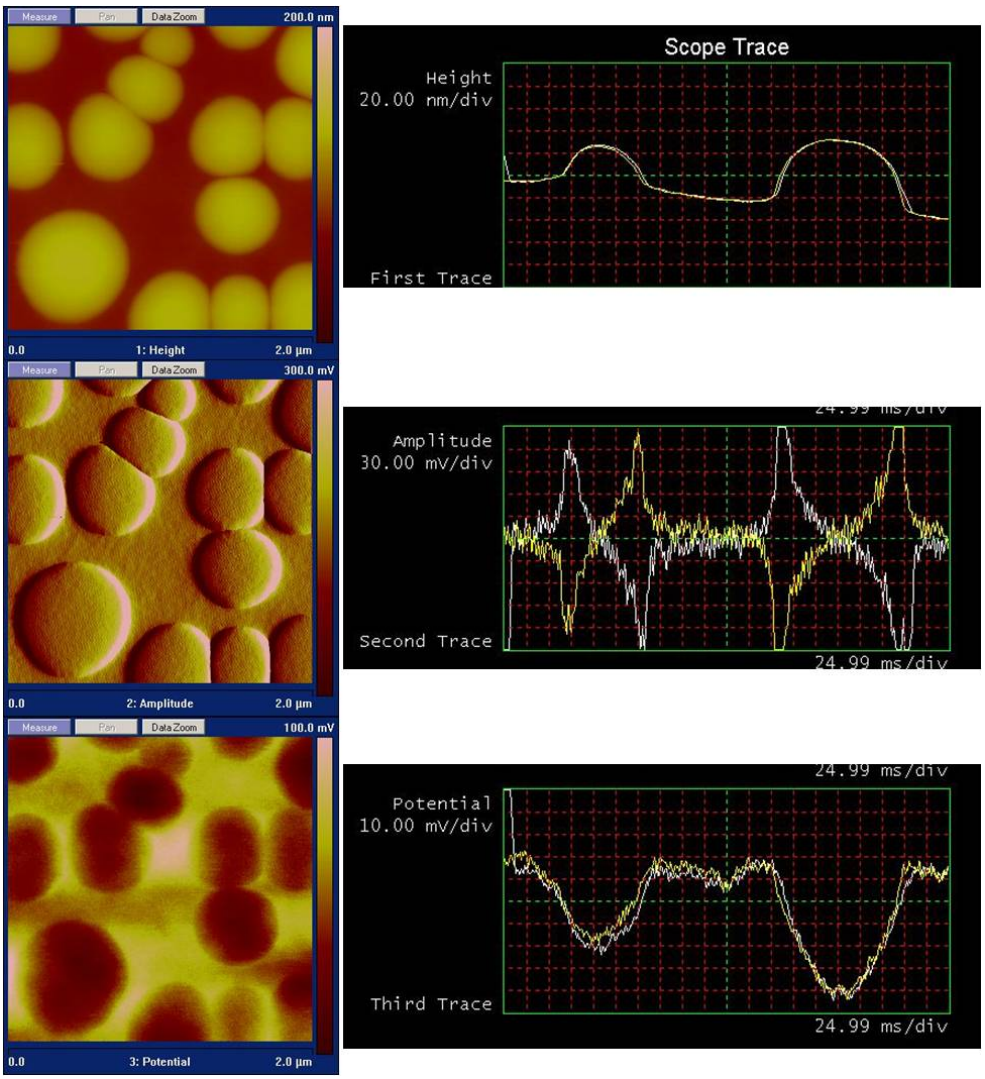

Figure 6- 5 Height, amplitude, potential images and the corresponding line sections on MDMO-PPV :PCBM solar cell active layer.

Our measurements on the MDMO-PPV:PCBM solar cell are shown in detail in Figure 6- 5. The large phase separation is clearly observed in the height and amplitude maps: the high elevated yellow balls are PCBM clusters and the low elevated red matrix is MDMO-PPV enriched. The correlation with the potential map is evident: PCBM clusters give lower surface voltage than the MDMO-PPV rich matrix (40 to 60 mV contrast). The correlation is even clearer on the three corresponding cross sections shown on the right side. The nice thing about our data is that they agree completely with the published work of

Maturova et. al[9] and confirm that our set-up is working. Their explanation for the dark contrast is that holes from the bottom electrode (ITO/PEDOT, HOMO level 5.2 eV) diffuse into the MDMO-PPV matrix (HOMO level 5.2 eV) which creates a positive space charge and hence a positive voltage while diffusion from the bottom electrode into the PCBM clusters is impossible because of the positioning of the HOMO level of PCBM (6.2eV).

6.2.3. On work function contrast

The last practice sample is pretty easy. We take a piece of SiO_2 covered with a passivation layer (in this case a self-assembled monolayer of HMDS, see chapter III), and then we expose half of the sample to UV/ozone radiation which has the property to remove the HMDS monolayer. KPFM (Figure 6- 6) gives a voltage shift of about 30 meV which is expected since it is known that the HMDS monolayer reduces the work function of the bare SiO_2 surface (remember that $V_{DC} = V_{measured} = (\phi_{tip} - \phi_{sample})/e$). The nice thing about this measurement is that the tip work function is not needed since the two materials under investigation are measured with the same tip and thus the tip influence is zero.

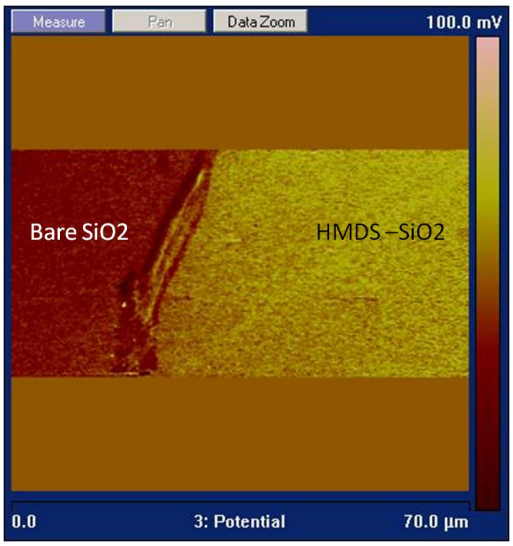

Figure 6- 6 Work function contrast between bare SiO_2 and HMDS treated SiO_2.

6.3. Visualizing charge transport on nanofibers in OFETs

It is now time to switch to the polymer nanofibers (NFs) and see what can be done with KPFM[19, 20]. The goal we aim is to observe the voltage variation along the NFs when they are connected by two electrodes. For this purpose, we have drop cast the NFs on a FET substrate, see scheme in Figure 6- 7. By tuning the gate voltage V_G, the carrier concentration and hence the conductivity of the NFs can be switched. We remind that, since they are p-type semiconductors, the conductivity increases if V_G decreases and vice-versa.

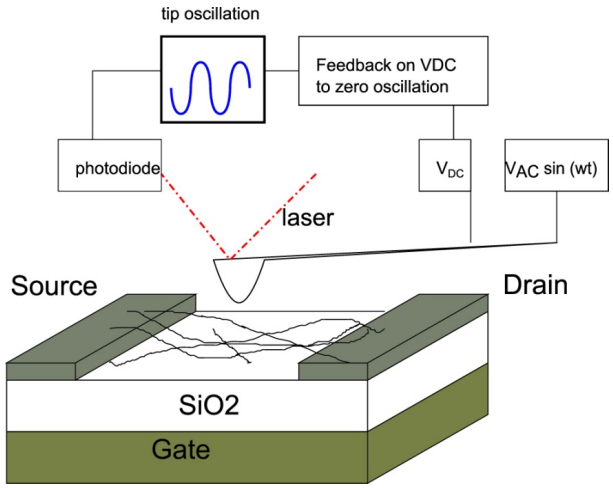

Figure 6- 7 Device structure for visualizing charge transport in nanofibers when deposited on a field-effect transistor.

Before studying the NFs, it is worthwhile to see what the KPFM response of the 3 electrodes without the NFs is, Figure 6- 8. On the same FET channel, three different bias conditions are successively applied by changing the drain and gate voltages while the source electrode is kept grounded. On the corresponding cross sections displays, we see that the potential profile follows well the applied voltages. This fact is evident for the open air source and drain electrodes but is more relevant for the buried gate electrode which is screened by the dielectric. Actually, the voltage on the dielectric surface (keep in mind that KPFM is a surface technique) is a combination of the three electrodes voltages: when changing V_G an electric field is created through the dielectric which modifies the voltage of the dielectric surface and V_D creates an electric field running in the plane of the dielectric. Consequently, the measured KPFM signal on the SiO_2 dielectric is not the gate voltage but a combination of the three electrodes voltages.

Two remarks can be drawn from the potential profiles. Firstly, we see that the potential signals are much smoother than the topographic signal; this is because the AFM resolution (around 1 nm) is almost 2 orders of magnitude better than the KPFM resolution (around 50-100 nm). Secondly, the amplitudes shown on the profiles (2 V for first potential profile, 1.5 V for second potential profile) are not the applied voltages on the electrodes (read on the left images). Again, the explanation is in equation (4).

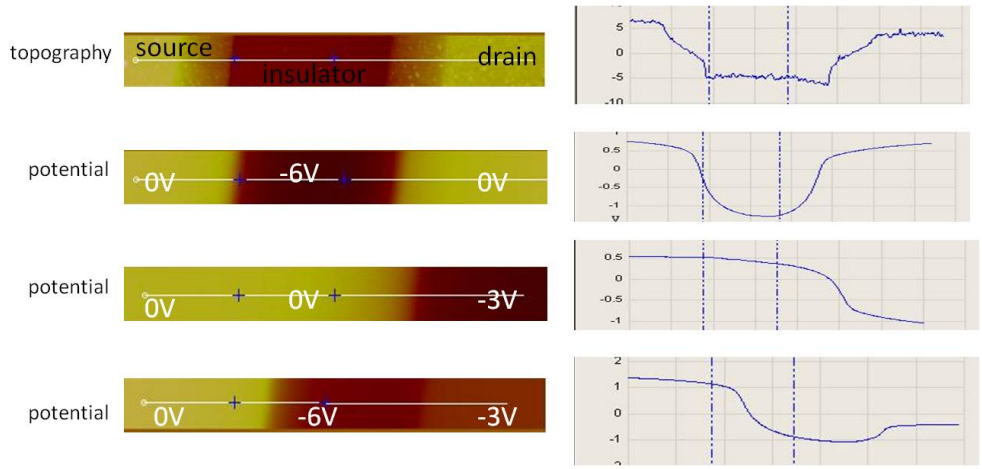

Figure 6- 8 Surface potential measurements on the FET structure without the nanofibers at different bias conditions (electrode thickness: 12nm, channel length: 1.5 µm). The applied voltages are written on the left images.

At this point, we know that KPFM is able to detect the potentials of the three electrodes, even the one of the buried gate. Now, we deposit the NFs on the sample, bias the OFET and perform some KPFM measurements, see Figure 6- 9. For $V_G = 5$ V, the holes are repelled from the NFs which turn insulating (OFF state). Can we measure this property with KPFM? On the potential map, no NFs signature can be seen, i.e. they have the same potential as the background dielectric, which is by definition insulating, and this proves that the NFs are insulating. Consequently, KPFM can detect the OFF state. For $V_G = -10$ V, holes are induced in the NFs which become conducting (ON state). On the potential image, we see a clear contrast between the low dielectric potential (dark color) and the high potential of the web of NFs (bright color). The origin for the contrast is that, being conducting, the NFs take the same voltage as the drain and source electrodes which is 0 V. Therefore, KPFM can detect ON state. In conclusion, KPFM is able to qualitatively differentiate conducting and insulating NFs.

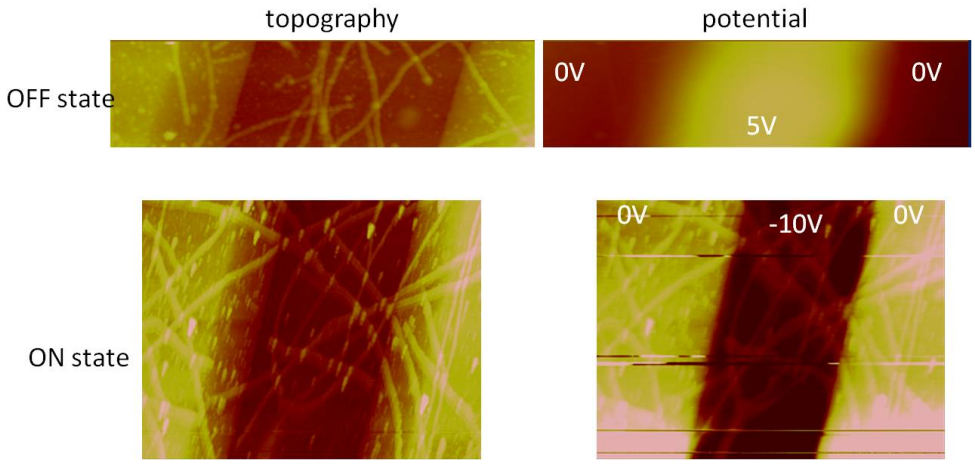

Figure 6- 9 Surface potential measurements on the FET substrate with the nanofibers: changing the gate voltage switches the nanofibers from OFF to ON states (electrode thickness: 12nm, channel length: 1.5 µm). The applied voltages are written on the right image.

Still, remains the question whether KPFM is able to measure quantitatively the potential profile along one NF. We see on Figure 6- 9 "On state" that the NFs voltage is lower than the drain and source electrodes voltages; this can be explained by equation (4) again. When the tip is above one NF, the undesired influence of the surrounding dielectric voltage (the dark red zone in the channel) is strongly reducing the NFs voltage in such a way that the voltage on the NFs is lower than 0 V (the drain and source voltages).

Maybe, a solution to cancel the harmful effect of the surrounding dielectric voltage would be to implement the following correction. Consider we want to measure the NFs potential for V_G = -10 V and V_D = -1 V. The obtained KPFM map, map1, is a combination of the dielectric and NFs voltage. Then, we measure a second KPFM map, map2, under the bias V_G = -10 V and V_D = 0 V. Since V_D = 0 V, map2 is only influenced by the dielectric voltage. Then, in order to remove the undesired influence of the dielectric voltage we propose to subtract map2 from map1. Due to a lack of time, this suggested correction technique has not been tested but could be implemented in the future.

6.4. Local charge trapping

KPFM can also be used to monitor charge trapping in organic semiconductors[10, 11]. An amount of trapped holes at a certain location is a space charge which can be measured with the KPFM tip by a positive voltage. We have tried to detect holes trapping in a web of NFs when deposited on a FET structure. In Figure 6- 10, the bias conditions are chosen in such a way that the nanofibers are conducting and thus that trapping of holes when moving through the semiconductor is possible. In particular, the intersection points of two NFs could be a good site for charge trapping. In Figure 6- 10C, the intersection points are clearly visible on the topography but unfortunately on Figure 6- 10D the bridging points are

hardly visible on the potential map. It is difficult to properly visualize bridging points from segments of NFs and therefore impossible to see if a positive voltage contrast is associated with the bridging points. Like in previous section, due to the poor lateral resolution and the detrimental effect of the dielectric voltage, we cannot conclude on the presence or not of holes trapping at the intersection points of two NFs. However, next chapter will be able to address this question.

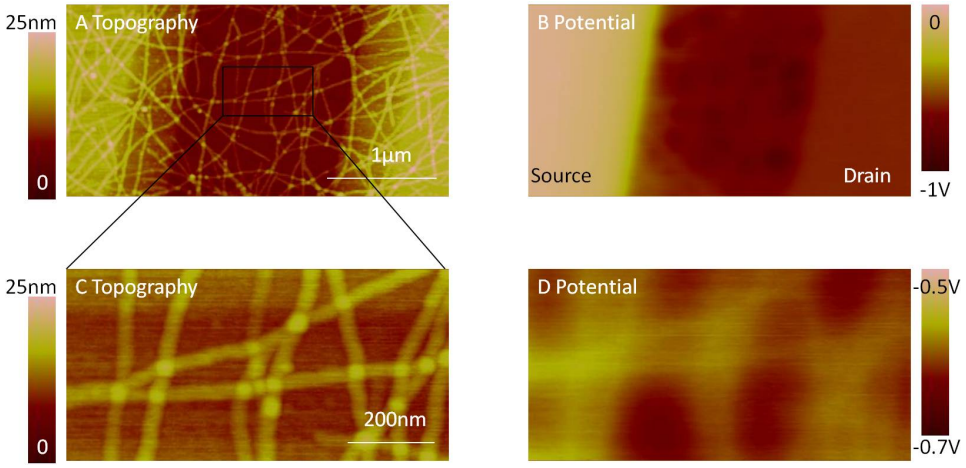

Figure 6- 10 Trial to visualize charge trapping at the intersection points of NFs. A-B: Topography and potential maps at low resolution. C-D: Topography and potential maps at high resolution. Both cases for V_G = -10 V and V_D = -1 V.

6.5. Technical details

KPFM was performed with the multimode AFM from Veeco equipped with the Nanoscope IIIa controller and the quadrex module. Tips were purchased from Nanosensors (PPP-EFM): $PtIr_5$ metal coating, nominal resonance frequency around 75 kHz, nominal spring constant around 2.8 Nm^{-1}. Alternating amplitude V_{AC} is comprised between 6 V and 9 V and lift height between 30 nm and 80 nm. All the shown measurements were performed in the home-made glovebox with oxygen concentration lower than 50 ppm and water concentration lower than 10 ppm.

MDMO-PPV:PCBM solar cell: PEDOT was spin -coated on ITO at 3000 rpm (acceleration 1500 rpm s^{-1}) for 40 s then annealed at 120 °C for 2 min. 12 mg of MDMO-PPV was added to 48 mg of PCBM in 5 ml toluene . The solution was spin-coated on ITO/PEDOT substrate at 750 rpm (acceleration 300 rpm s^{-1}) for 2 min.

Nanofibers in OFETs: We used the OFETs substrates described in chapter II with thin drain and source electrodes (10 nm Pt layer on top of a 2 nm Ti adhesion layer) to reduce NFs disruption or damage. Source and drain electrodes were connected as shown in Figure 6- 3, gate electrode was connected to

the piezoelectric scanner chuck using Ag paste and was controlled by a voltage source intern to the AFM. Measurements were performed on P34T nanofibers (0.005 wt.%) presented in chapter I. The P34T NFs were drop cast on the substrate and then the remaining solvent (o-chlorotoluene) was gently N_2 flushed.

[1] L. Kelvin, *Philos. Mag.* **1898**, 46, 82.
[2] V. Palermo et al., *Advanced Materials* **2006**, 18, 145-164.
[3] T.R. Albrecht et al., *J. Appl. Phys*. **1991**, 69, 2, 668-673.
[4] L. Bürgi et al., *Appl. Phys. Lett*. **2002**, 80, 16, 2913-2915.
[5] K.P. Puntambekar et al., *Appl. Phys. Lett.* **2003**, 83, 26, 5539-5541.
[6] A. Petrovic et al., *Synth. Met*. **2009**, 159, 1210-1214.
[7] L. Liu et al., *Appl. Phys. Lett.* **2010**, 96, 083302.
[8] H. Hoppe et al., *Nano Lett.* **2005**, 5, 2, 269-274.
[9] K. Maturova et al., *Adv. Funct. Mater.* **2009**, 19, 1-8.
[10] H. Huang et al., *Appl. Phys. A* **2009**, 95, 125-130.
[11] T. Hallam et al., *Phys. Rev. Lett*. **2009**, 103, 256803.
[12] L. Bürgi et al., *Synth. Met.* **2004**, 146, 297-309.
[13] S. Barbet et al., *Appl. Phys. Lett*. **2008**, 93, 212107.
[14] C. Kim et al., *J. Kor. Phys. Soc.* **2005**, 47, S417-S421.
[15] L.S.C. Pingree et al., *Adv. Mater*. **2009**, 21, 19-28.
[16] H.O. Jacobs et al., *J. Appl. Phys*. **1998**, 84, 3, 1168-1173.
[17] D.S.H. Charrier et al., *ACS Nano* **2008**, 2, 4, 622-626.
[18] O. Douhéret et al., *Microelectronic Engineering* **2007**, 84, 431.
[19] A. Liscio et al., *Adv. Funct. Mater.* **2006**, 16, 1407-1416.
[20] A. Liscio et al., *Adv. Funct. Mater.* **2008**, 18, 1-8.

Eurêka!
- Archimède -

Chapter VII: Measuring current at nanoscale

In this chapter, we present the results obtained on nanofibers with Conductive Atomic Force Microscopy (CAFM). In a first part, the description and characterization of a CAFM-based transistor is given. In the CAFM-transistor, one of the electrode is the mobile conducting CAFM tip. It allows us to measure the current distribution at the nm scale and to probe the current in one nanofiber. In a second part, we focus on charge carrier transport within one single nanofiber by measuring the mobility along the NFs length and height.

7.1. Working principle

CAFM is a current sensing AFM technique where a metal coated tip scans in contact mode the sample and measures simultaneously the sample conductivity and the topography under a certain voltage. CAFM can be used in two modes: the first mode, called imaging mode, consists in applying a constant voltage to the sample while the tip is scanning. The topography and current images are simultaneously recorded and allow correlating the highly conducting regions with the topography features. For the second mode, called spectroscopic mode, the tip is fixed on one point and the sample voltage is swept giving an I/V characteristic.

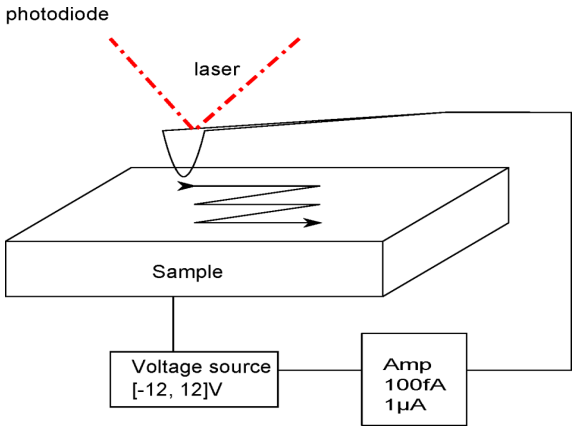

Figure 7- 1 CAFM set-up.

7.2. CAFM-based transistor

As already explained in chapter I, poly(3-alkylthiophene) (P3*A*T) nanofibers (NFs) offer an ideal tool for investigating charge transport phenomena in field-effect transistor structures [1,2]. In chapter III, we have shown measurements for webs of P34T NFs. Depending on the surface coverage, we have found out mobilities in the range 5 X 10^{-3}- 5 X 10^{-2} $cm^2 V^{-1} s^{-1}$. In the literature, webs of P3*A*T NFs have been studied intensively and mobility values in the range 0.04 $\pm$ 0.02 $cm^2 V^{-1} s^{-1}$ were reported by different groups [3,2,4]. However, the employed OFET devices have dimensions (channel width: W~mm; channel length: L~10 µm) much larger than typical NFs dimensions (width: 20 nm; length: ~ µm)[5]. Consequently, charge transport in these cases involves transport through two processes: within individual NFs and interfiber transport at the intersection of two nanofibers. The impact of these bridging points on the effective transport is unknown and subject to discussion[2,6,7].

In order to address these questions, we have developed a transistor where one of the electrodes is the mobile CAFM tip. It enables one to resolve the current distribution at the nm scale within a web of P34T NFs and to evaluate the role of the bridging points in charge transport within a web of NFs.

In a first step, a qualitative description of our CAFM field-effect transistor will be given on samples obtained from a high concentration dispersion (0.005 wt%). Its capability to resolve the current distribution at the nm scale and the appearance of the transistor effect (increase of NFs conductivity by a negative gate voltage) will be demonstrated. Then, in a second step, we will focus on samples obtained from a lower concentration dispersion (0.001 wt%) and measure the contact resistance R_C. Finally, in a third step, we will evaluate the role of NFs bridging points on charge transport.

7.2.1. Transistor with CAFM tip electrode: proof of concept

To study charge transport along the NFs, we have used a transistor structure like the one depicted in Figure 7- 2. It consists of a highly n-doped Si gate electrode with a SiO_2 gate dielectric (gate capacitance per unit area: $C_0 = 16.9$ nF cm^{-2}). A self-assembled monolayer of hexamethyldisilazane (HMDS) was used to passivate SiO_2. Using conventional photolithography, a thin drain electrode (10 nm Pt layer on top of a 2 nm Ti adhesion layer) was patterned. The electrode was made as thin as possible to improve electrode connection and to avoid NFs disruption since their thickness is close to 4 nm. Compared to a standard FET device with two fixed electrodes, our set-up has one mobile electrode which is the CAFM tip. While scanning across the sample, the current flowing from the CAFM tip to the Pt drain electrode via the NFs is measured. Two voltage sources and associated current meters were used: one being internal to the AFM and one external (Keithley 2400 sourcemeter). Both power supplies are grounded on the tip potential. To determine the transistor transfer characteristics for which the gate voltage, V_G, is swept at a fixed drain voltage, V_D (see Figure 7- 12), the AFM source is connected to V_G and the external one to V_D. While to determine the output characteristics for which V_D is swept at different fixed V_G (see Figure 7- 4), both sources are switched.

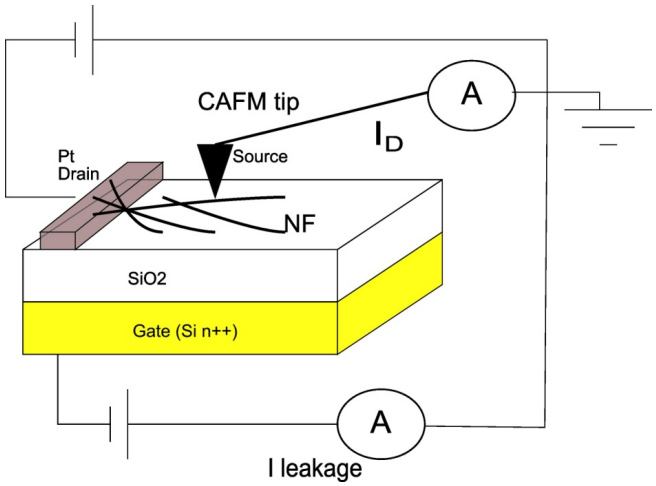

Figure 7- 2 Schematic of the CAFM field-effect transistor with one electrode being the mobile CAFM tip

The NFs were randomly drop-cast on the substrate. Due to their high surface coverage, they form a two-dimensional web connected to the drain electrode even at a distance of hundreds of µm from the electrode. Figure 7- 3 shows three typical CAFM measurements in the imaging mode. In the first zone, the correlation between the topography image (A) and the current image (B) is excellent: the current is zero when the tip is not touching any NFs and becomes positive as soon as a NF is reached. Some NFs, like the ones encircled in A, are not connected to the drain electrode and consequently the associated current in B is zero. The correlation is also outstanding for zone 2 (compare C and D) and zone 3 (compare E and F). In other words, it is possible to measure the current distribution with nm resolution and in particular through isolated NFs.

A second key point shown in Figure 7- 3 is the conductivity enhancement of the NFs when the V_G is decreased as this is expected for p-type semiconductors. On D, V_G is progressively decreased from 0 V to -12 V leading to a current increase by a factor 10 while on F the NFs are alternately switched from insulating to conducting states by switching the gate voltage between 0 V and -10 V.

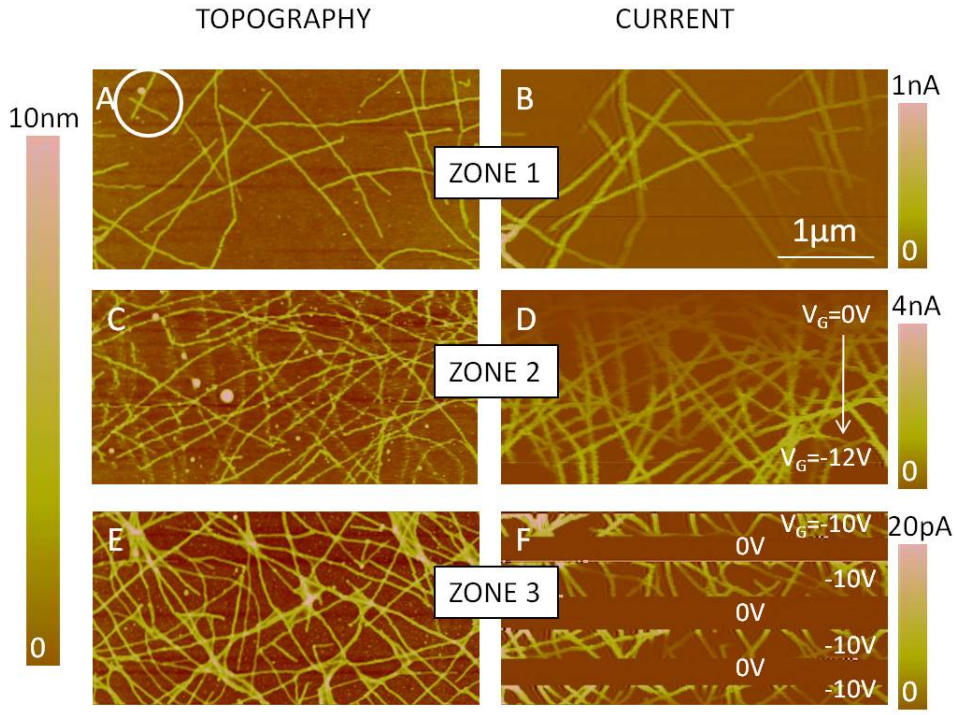

Figure 7- 3 Topography and corresponding current images obtained on P34T NFs on HMDS treated SiO_2 at various V_D and V_G conditions. A-B, zone1: V_D=2 V and V_G=-4 V are fixed. C-D, zone2: the fibers conductivity is increased as V_G is decreased progressively from top to bottom with V_D fixed at 4 V. E-F, zone3: as V_G is switched from -10 V to 0 V, the NFs are switched from on to off states with V_D fixed at 4 V.

An important question for current transport through nanofibers is to know whether the measurements are destructive or not for the NFs. To address this point, we image two times the same area for fixed V_D and V_G, and compare the two current maps. By changing V_D and V_G, the mean value of the current map can be tuned. It is found that for mean current lower or equal to 4 nA, the second map keeps the same signature as the first one but with a slight current reduction. This hysteresis is a well known phenomenon in organic transistor where hole trapping causes the transistor current to continuously decrease under constant bias conditions[8]. Therefore, the observed current reduction is not attributed to NFs destruction but to bias stress effects. On the other hand, for current approaching 5 nA we observe that the current drops immediately to zero and stays for the rest of the image. Consequently, we have a maximum current of 4 nA leading to a maximum current density of $J_{max} = \frac{I_{max}}{Wh}$ =20 kA cm^{-2} with W=20 nm the width of one NF and h=1 nm the thickness of the accumulation layer[9]. It is widely accepted and reported that in OFETs conduction mainly occurs in the first nm of the semiconducting layer from the dielectric interface[9, 10]. The reasons are that both the charge carrier density and field-effect mobility are significantly reduced at 1 nm depth perpendicularly from the interface compared to interface values[9].

Since the conductivity is proportional to the product of the mobility by the carrier concentration, it explains that conduction occurs in the first nm. This result is valid for undoped semiconductors placed in field-effect devices operating in the linear regime and does not depend on the lateral dimensions of the investigated structure and thus is also applicable for the nanofibers. For metals, the DC fusing current density for a straight wire is given by Preece's law $J_{max} = \frac{4k}{\pi d^{0.5}}$ where k is a metal dependent constant and d is the wire diameter in cm[11]. As seen, the maximum density is dependent on the wire diameter: for aluminum (k= 1870 A cm$^{-1.5}$) $J_{max} = 7600$ A cm^{-2} for $d = 1$ mm and $J_{max} = 1.7$ MA cm^{-2} for 20 nm diameter which is close to the width of the NFs. In other words, the maximum current density is much higher for metals which was expected since the melting point of Al (around 660 °C) is considerably higher than for P3HT (=P36T) (around 240 °C).

All the measurements shown in Figure 7- 3 are for positive drain voltage where the holes are emitted from the drain electrode and collected at the tip. There is no hole injection barrier from the Pt drain electrode (work function ~5.6 eV) into the polymer HOMO level (~5.2 eV). For negative drain voltage, less stable and reproducible results were obtained probably because of the high work function of the drain electrode which hampers holes collection or due to a high contact resistance at the tip NFs junction which limits holes injection. Therefore, most of the data presented here are made with positive drain voltage. We are aware that the denominations "drain" and "source" electrodes like sketched in Figure 7- 2 could be controversial since for positive V_D holes are emitted from the side electrode and collected at the tip electrode. However, we keep this appellation because our source electrode is grounded as this is usually the case.

In the spectroscopic mode, an output characteristic can be performed at a fixed tip position, see Figure 7- 4A. In order to deplete the channel at the drain side and thus visualize the saturation regime, it is necessary to sweep V_D within negative values. The obtained curves are those of a p-type semiconductor with current amplification for negative V_G, which confirms once again that we constructed a transistor with one mobile electrode.

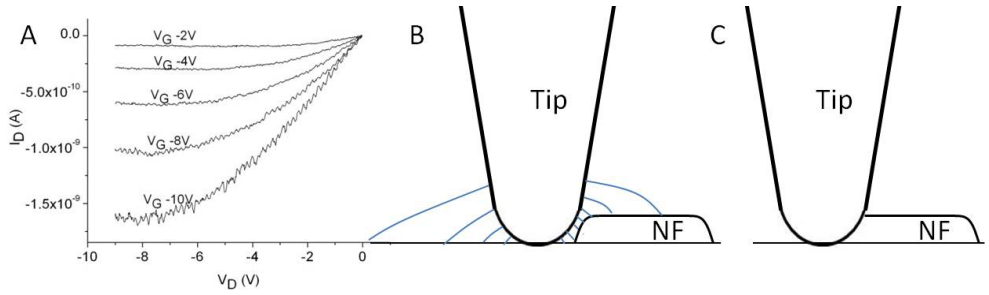

Figure 7- 4 A: Output characteristic for a fixed CAFM tip position on a P34T NF showing the expected linear and saturation behaviors for a p-type semiconductor working in accumulation mode. B: Field lines in the vicinity of the CAFM tip. C: The tip indents the NF.

It is observed in almost all the current maps that the "electric width" (defined as the width of one NF measured in the current map) is larger than the "geometric width" (as measured in the topography

map) which is also larger than the true NF width due to tip broadening[12]. The typical deviation between electric and geometric width is 6-8 nm (3-4 nm on each side). It corresponds to a situation where current is detected while the CAFM tip is still pressing on the substrate, like this is sketched in Figure 7- 4B and Figure 7- 4C. A tunneling current is expected to occur for tip-NF distance lower than 1 nm, situation in Figure 7- 4B. This is one contribution for the difference between geometric and electric width. The second occurs when the tip touches one NF, indents it along a certain lateral distance, situation in Figure 7- 4C, until the force exerted on the tip is high enough to be detected. At this moment, the AFM controller lifts the tip and the geometric width is detected.

7.2.2. Estimation of the contact resistance, R_C

Due to the limited contact size at the tip (contact radius ~2nm, see experimental part) and the short length of the NFs, the question of contact resistance effects is relevant[13, 14]. Before trying to extract any mobility values from our data, we have to prove that the measurements are not contact limited. The total resistance R_{tot} (which is the one we directly measure with the CAFM) is the sum of the contact resistance R_C and the channel resistance: $R_{tot} = R_C + R_{channel} = R_C + \frac{\rho L}{Wh}$ with L the channel length, W the channel width, h the thickness of the accumulation layer and ρ the NFs resistivity. Since a current map displays the current in the NFs as a function of the length of the NFs, it is possible to estimate R_C as the value of R_{tot} at zero length. Figure 7- 5 explains the strategy to determine the contact resistance R_C. First, topography and current maps are taken close to the drain electrode (A and B) but without reaching it to avoid instabilities. Then, the drain electrode is partially imaged to measure the channel length (C). Finally, we zoom in on the NFs to be studied (D and E). F and G show the current profiles along top and bottom NFs where the extrapolation to zero length gives $R_C \sim 1\ \text{G}\Omega \pm 1\text{G}\Omega$. Considering the worst case $R_C \sim 2\ \text{G}\Omega$, this gives $R_C W \sim 4\ \text{k}\Omega$ cm which is of the same order of magnitude as the reported values for standard organic transistors[15]. Although R_C seems huge, this is only 5% of R_{tot} when we measure 100 pA at $V_D = 4$ V which is typical for CAFM measurements. It is worth noting that the same behavior was observed on many different samples. Therefore, we can conclude that the measurements are not contact limited.

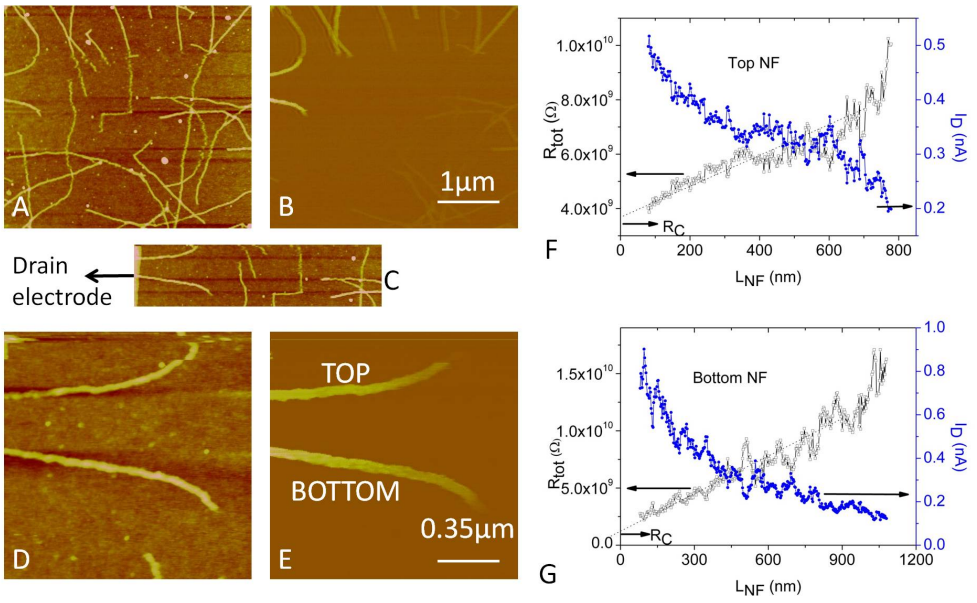

Figure 7- 5 Estimation of contact resistance from current images at fixed bias for P34T NFs on HMDS treated SiO_2. A: Topography and B: corresponding current images for V_G= -4 V and V_D= 2 V. The drain electrode is out of the image on the left. C: topography image of a part of A with the drain electrode on the left extremity. No bias is applied when imaging the drain electrode to avoid instabilities. D: Zoomed topography and E: corresponding current images of C showing two NFs. The drain electrode is 80 nm on the left of the image. F-G: Current profiles along both individual NFs where it is clear that the current increases as the tip approaches the drain electrode. L_{NF} denotes the length of the NF starting from the drain electrode. From the extrapolation of R_{tot} to L_{NF}=0 we obtain R_C ~1 GΩ ± 1GΩ.

7.2.3. Influence of bridging points on the charge transport

The main benefit of the CAFM based transistor is that one can visualize the current distribution at the nm scale and, as it will be demonstrated, it allows us to evaluate the electrical resistance of bridging points of nanofibers.

For each pixel of a current map, a current $I(x,y)$ is obtained which can be converted into an equivalent electrical resistance using the relation $R_{eq}(x,y) = V_d/I(x,y)$ (1). An important question is to know what influences $R_{eq}(x,y)$. When flowing from the tip, fixed on point P, to the drain electrode, the current is split at each bridging point (defined as the intersection of two or more NFs) and follows different percolation pathways until the drain electrode is reached. The electrically active web between the tip and the drain electrode is composed of n bridging points each having a resistance R_{bp} and m NFs segment of length l with a length dependent intrinsic resistance $R_{NF}(l)$. R_{eq} at point P is influenced by all these elements: $R_{eq,P} = f\left(n, R_{bp}, m, R_{NF}(l), R_C\right)$ (2). The electrical resistance of a bridging point, R_{bp}, can be estimated by comparing the CAFM currents at the different sides of a bridging point. If the tip-electrode distance is large (more than 10 µm) and the NFs concentration is high (like in Figure 7- 3),

then n and m can be as high as 10^4 and 10^5. These numbers are so large that even if the transport was limited by bridging points, no current variation would be detected.

On the other hand, measurements taken at low concentration and close to the drain electrode bring quantitative information. In Figure 7- 6 the currents at the four poles (points 1, 2, 3 and 4) of a typical bridging point are compared: $I_1 = 430$ pA, $I_2 = 420$ pA, $I_3 = 430$ pA, $I_4 = 395$ pA. The four equivalent resistances of the four poles are deduced by looking at the topographical image. For instance, when the tip is on point 1, $R_{eq,1}$ is the parallel association of four different pathways (the ones going through 2, 3, 4 and the one to the drain electrode). It is clear that the resistance of the short pathway to the drain electrode is much smaller than the three others pathways hence $R_{eq,1} = R_{NF}$(300nm) with 300 nm the length between point 1 and the drain electrode, as deduced from the topography map. A similar reasoning holds for point 2, 3 and 4 for which the bridging point contribution has to be added: $R_{eq,2} = R_{eq,3} = R_{eq,4} = R_{NF}$(300nm) $+ R_{bp}$. Using equation (1) for the four poles, it is possible to calculate R_{NF}(300nm) = 4.6 GΩ and R_{bp} = 0.4 GΩ. In other words, the electrical resistance of the bridging point is much smaller than the one of a segment of NF.

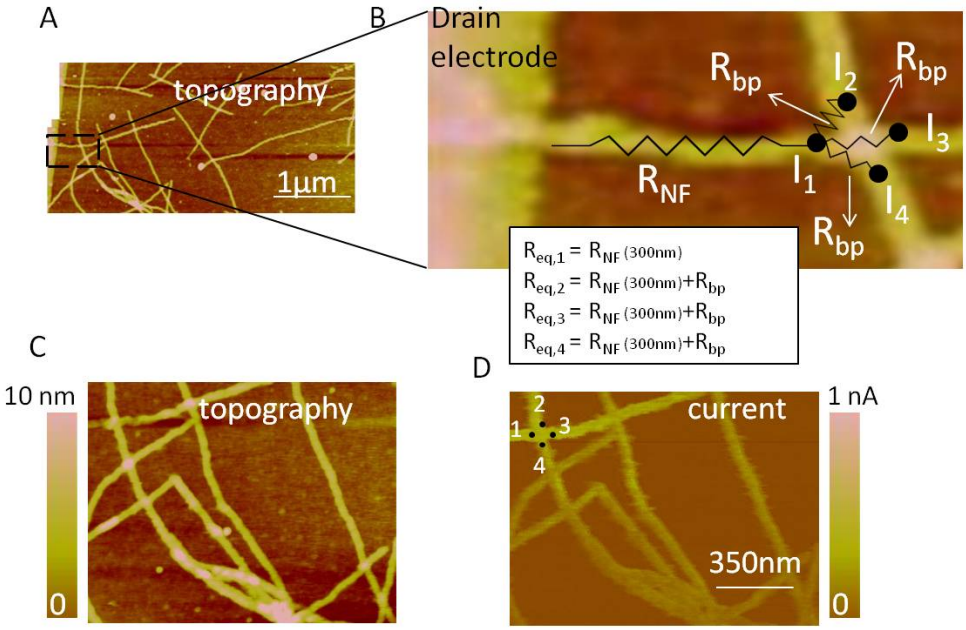

Figure 7- 6 Evaluation of the electrical resistance of the bridging point of two NFs. A: topography image of some NFs touching the drain electrode. B: zoom of A, the equivalent electrical circuit is shown. C and D: topography and current images of a part of A from which the four current values are extracted (V_G = -4 V and V_D = 2 V).

To get more confidence in this result, the analysis has been repeated many times on other samples, Figure 7- 7 and Table 1. The literal expressions for $R_{eq,i}$ have been obtained from the careful reading of

the large scale topography images (left column Figure 7- 7). On these images, no bias voltage is applied because the metal-metal contact (tip - drain electrode) would cause instabilities. The current values are extracted from the current maps.

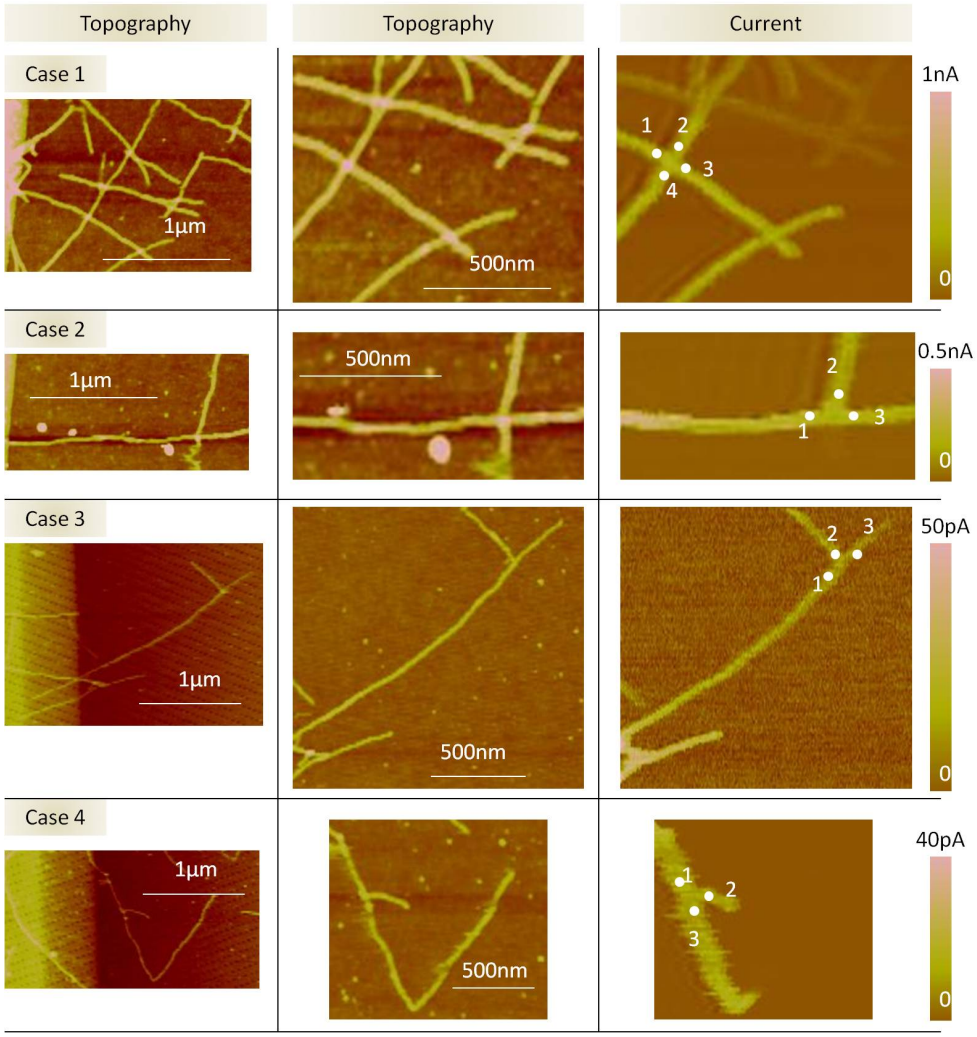

Figure 7- 7 Four additional case studies to evaluate $R_{NF}(l)$ and R_{bp}. Left column is a large scale image including the drain electrode on the left extremity. Middle and right columns are a zoomed region of the left column. See Table 1 for numerical analysis.

Case	Height of bridging point	Bias	R_{eq}	I	$V_D = R_{eq,1}I_1 = R_{eq,2}I_2 = R_{eq,3}I_3 = R_{eq,4}I_4$
1	7.8 nm	V_D = 2 V V_G = -4 V	$R_{eq,1} = R_{NF}$(600nm) $R_{eq,2} = R_{NF}$(600nm) + R_{bp} $R_{eq,3} = R_{NF}$(600nm) + R_{bp} $R_{eq,4} = R_{NF}$(600nm) + R_{bp}	I_1 = 380 pA I_2 = 350 pA I_3 = 350 pA I_4 = 380 pA	R_{NF}(600nm) = 5.3 GΩ R_{bp} = 0.4 GΩ
2	7.4 nm	V_D = 2 V V_G = -6 V	$R_{eq,1} = R_{NF}$(1.5µm) $R_{eq,2} = R_{NF}$(1.5µm) + R_{bp} $R_{eq,3} = R_{NF}$(1.5µm) + R_{bp}	I_1 = 221 pA I_2 = 205 pA I_3 = 220 pA	R_{NF}(1.5µm) = 9.0 GΩ R_{bp} = 0.7 GΩ
3	4.1 nm	V_D = 2 V V_G = -1 V	$R_{eq,1} = R_{NF}$(1.6µm) $R_{eq,2} = R_{NF}$(1.6µm) + R_{bp} $R_{eq,3} = R_{NF}$(1.6µm) + R_{bp}	I_1 = 18 pA I_2 = 17 pA I_3 = 18 pA	R_{NF}(1.6µm) = 111.1 GΩ R_{bp} = 6.5 GΩ
4	4.2 nm	V_D = 4 V V_G = 0 V	$R_{eq,1} = R_{NF}$(500nm) $R_{eq,2} = R_{NF}$(500nm) + R_{bp} $R_{eq,3} = R_{NF}$(500nm) + R_{bp}	I_1 = 13 pA I_2 = 12 pA I_3 = 12 pA	R_{NF}(500nm) = 307.6 GΩ R_{bp} = 25.6 GΩ
Fig.6	6.9 nm	V_D = 2 V V_G = -4 V	$R_{eq,1} = R_{NF}$(300nm) $R_{eq,2} = R_{NF}$(300nm) + R_{bp} $R_{eq,3} = R_{NF}$(300nm) + R_{bp} $R_{eq,4} = R_{NF}$(300nm) + R_{bp}	I_1 = 430 pA I_2 = 420 pA I_3 = 430 pA I_4 = 395 pA	R_{NF}(300nm) = 4.6 GΩ R_{bp} = 0.4 GΩ

Table 1 Bias conditions, expressions for equivalent electrical resistance, measured currents and calculated R_{NF}, R_{bp} values for the configurations of Figure 7- 7. Case of Figure 7- 6 is rewritten for convenience.

We note that as expected for p-type semiconductors $R_{NF}(l)$ and R_{bp} are reduced at negative V_G. Table 1 confirms the observation made in Figure 7- 6 and allows us to write the following equation

$$R_{bp} < 0.1\, R_{NF} \quad (3)$$

It means that the electrical resistance associated with the bridging of two or more individual NFs can be neglected with respect to the intrinsic resistance of the NFs. As complementary proof, we will measure, later in this chapter, the mobility in one single nanofiber and obtain a value which is very close to the mobility in a web of nanofibers meaning that the bridging points do not limit the charge transport and that equation (3) is valid. This point will be further discussed in chapter VIII.

7.2.4. Structure of bridging points

Based on relation (3) and on the thicknesses of NFs bridging points, some information on how the NFs intersect can be deduced. Because of its higher resolution and softer contact than CAFM, tapping mode AFM has been extensively used to measure the thicknesses of NFs bridging points. Two kinds of intersections are observed: (1) the big majority of them have four arms (noted here as X intersection) with a thickness comprised between 6.5 and 8 nm (see first two cases and last case of Table 1); (2) the rest have three arms (noted here as T intersection) with a thickness of 4 nm (see cases 3 and 4 of Table 1). For the X intersection, since the intersection height is higher than 4 nm (height of one single NF) it

means that the two NFs stack on each other and that the 8 nm X intersections correspond to a NFs superposition without interpenetration of the two NFs like illustrated on Figure 7- 8**.** In this configuration, their poor electrically conducting alkyl side chains touch each other leading to a high transport barrier for a hole going from NF1 to NF2 (or vice versa). This is in contradiction with relation (3). Many papers in the literature have discussed the importance of tie-molecules for conduction in conjugated polymers[16, 17, 18]. The tie-molecules are molecular segments which start in one crystalline domain and are connected to another crystalline domain. The edges of the P34T NFs are expected to contain a lot of these loose polymer stands. The first reason is that the polydispersity of the NFs is not 1 but 2.1 and therefore there is a large variation in the length of the polymer chains, the longest ones being the tie-molecules. A second argument for the presence of tie-molecules comes from a paper of Zhang et. al.[19] They monitored the width of P3HT nanofibers as a function of the weight average molecular weight M_w. They found a linear trend for $M_w < 10$ kg mol^{-1} which means that the width of one NF is proportional to the length of the polymer chain. On the other hand, for $M_w > 10$ kg mol^{-1}, they observed a constant width (at around 30 nm like our NFs) independent of M_w which means that the polymer chains are folded inside the NFs or that some chains extend out of the NFs. The $M_w$of our NFs is largely above the threshold value of 10 kg mol^{-1} and it suggests that our NFs are composed of folded polymer chains and tie-molecules. Thus when the NFs are stacked on each other, the loose polymer strands can connect two different polymer chains and create conduction pathways, see Figure 7- 8. In this way, the charge transport between both NFs is fast and the relation (3) is verified. For the 6.5 nm X intersections, there is presumably an interpenetrating distance of about 1.5 nm which means that the highest polymer chain of the bottom NF is facing the lowest polymer chain of the top NF and holes can easily hop from one NF to the other without having to travel the alkyl side chains, thus the transfer is fast.

For the T intersections, the situation is much different. Here, the two NFs are at the same level and, as shown on Figure 7- 8, all the polymer backbones are facing each other leading to a fast hole transport between the NFs. However, we still expect tie-molecules to be present and to reinforce the conduction mechanism.

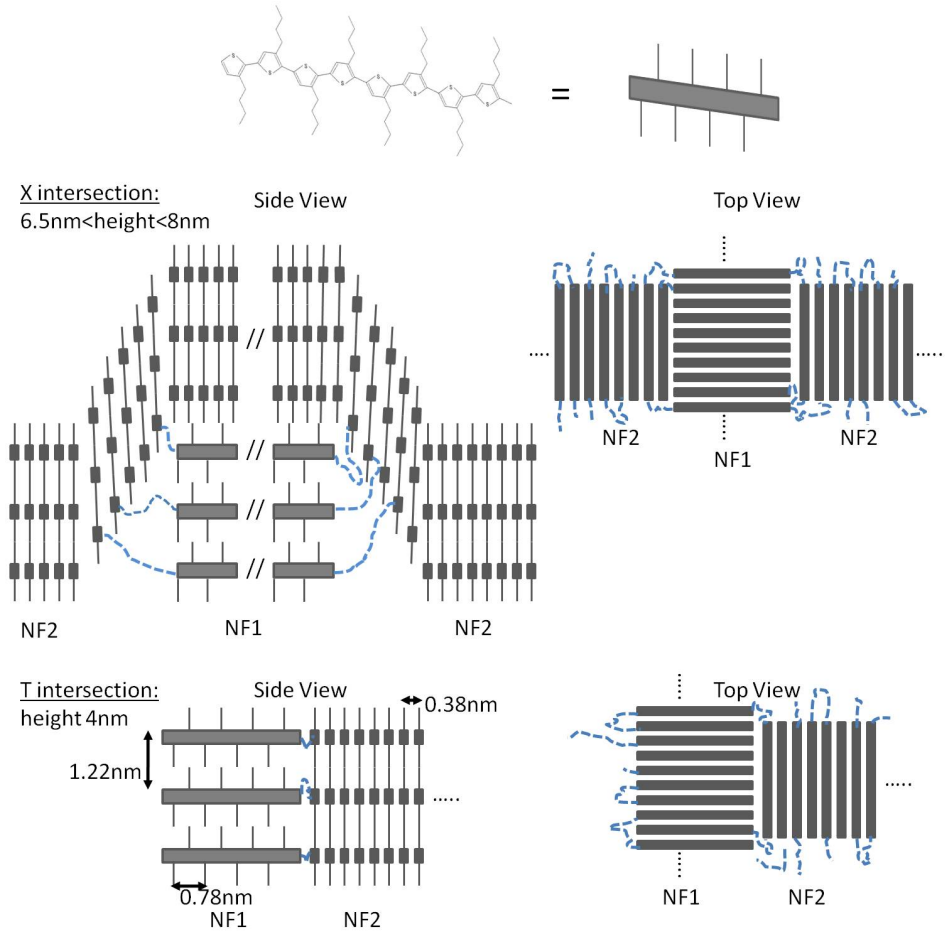

Figure 7- 8 Schematics showing the structure of NFs bridging points for a X intersection (intersection with four arms) and a T intersection (intersection with three arms). Blue dashed line refers to tie-molecules.

7.3. Mobility in one single NF

In this section, we aim at measuring charge transport within one isolated nanofiber. In Figure 7- 9, we define the mobility along the NF length as longitudinal mobility, μ_L, and the mobility along the NF height as transversal mobility, μ_T.

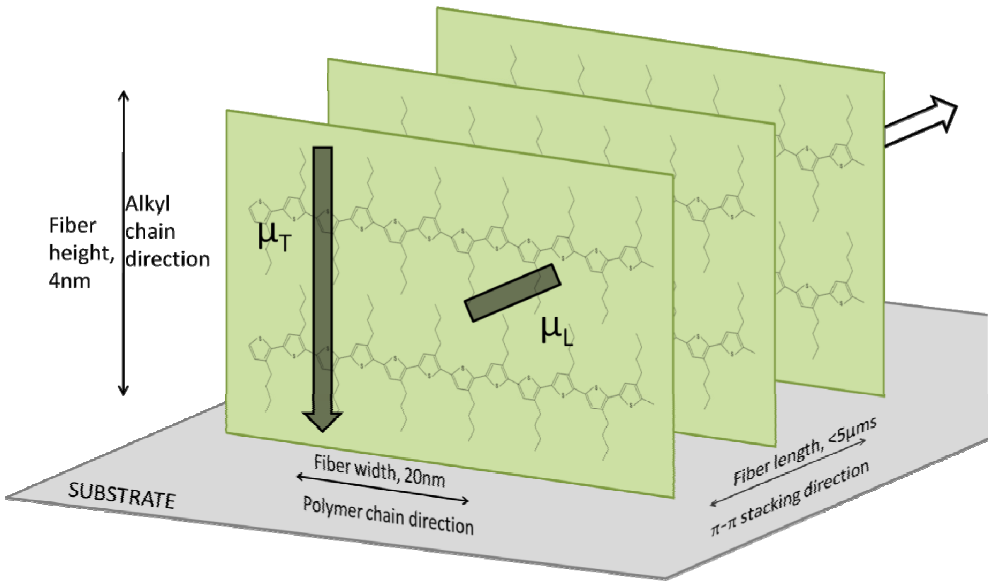

Figure 7- 9 Schematic of the P34T nanofiber and the two investigated charge transport directions. The longitudinal and transversal mobilities within one NF are probed.

7.3.1. Longitudinal mobility, μ_L

In order to assess the longitudinal mobility, we have tried three different techniques each having their own drawbacks and advantages, Table 2.

	Photolithography	**e-beam lithography**	**CAFM transistor**
Source/Drain Contacts	Bottom/Bottom	Top/Top	Bottom/Top
Main Advantage	Mature technique: process is established	Place the electrodes where desired	One mobile electrode
Main Drawback	How to position the NFs on the electrodes?	No available depositing metal with right work function and adhesion properties	Delicate and laborious technique: tip quality, scanner stability, cables connections, no shortcut …
Successful?	No	No	Yes

Table 2 Summary of the three techniques used to measure the longitudinal mobility

7.3.1.1. Photolithography

Photolithography is the standard technique to fabricate micro electrodes. We have used it in the etching mode[20] with a negative photoresist[21]. A scheme in Figure 7- 10 depicts the essential steps involved in the process. We have managed to realize FET structures with channel length in the vicinity of 2.5 µm but unfortunately we were unable to perform any I/V measurements on the nanofibers. The reason is that the deposition of NFs on the substrate is completely random and having only one NF bridging the two electrodes was impossible. Either we had a web of NFs between the electrodes, either we had no NFs at all. Then, we had to go for another solution.

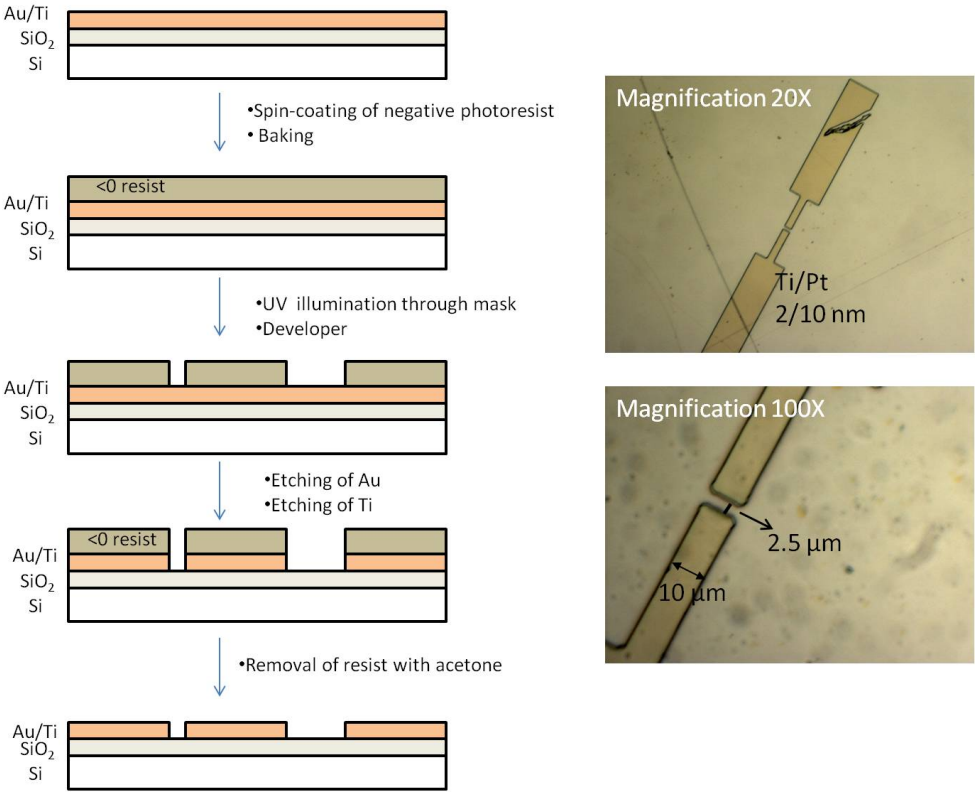

Figure 7- 10 Left: Photolithography process (case of etching with negative photoresist). See technical details section for more information. Right: pictures of some electrodes made of Pt on an adhesion Ti layer.

7.3.1.2. E-beam lithography

E-beam lithography is very similar to photolithography. The difference being that the resist is not light exposed but electron beam exposed giving a much better lateral resolution. We used it in the lift-off

mode with a positive resist (PMMA) in such a way that the operator can choose the nanofiber on which the electrodes will be deposited, see Figure 7- 11.

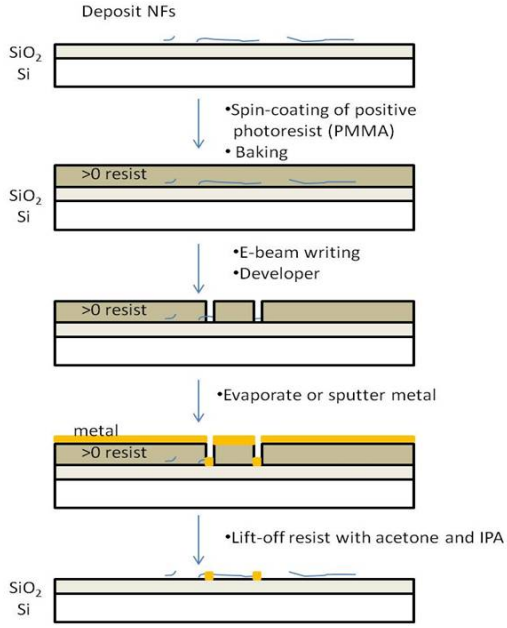

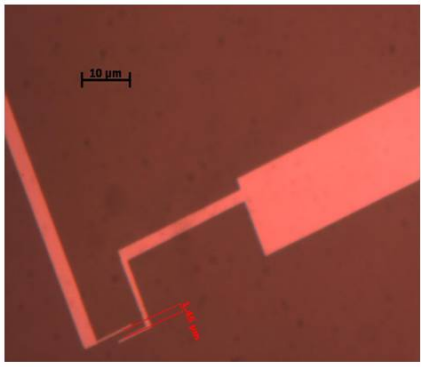

Figure 7- 11 Left: e-beam lithography process. Right: Ag electrodes (50 nm thick) on SiO_2 fabricated using e-beam lithography. The gap between the two electrodes is 1.45 µm. If needed, the complete sample preparation recipe can be asked at Bart Ruttens or my-self.

In collaboration with Bart Ruttens (University Hasselt, IMO), many samples with different processing conditions were fabricated. The critical step was the choice of the metal which must stick on SiO_2 (then noble metals like Au and Pt are excluded) and must have a high work function (>5 eV) for easy holes injection and collection in P3ATs (then Al and Ca are excluded). Therefore, we have tried Ag: one of our best samples is shown in Figure 7- 11. Unfortunately, due to a lack of time and the difficulty for the metal, no I/V measurements could have been performed. Then, we had to go for another solution.

7.3.1.3. CAFM-based transistor

Using the CAFM transistor, we have managed to measure μ_L. Figure 7- 12 shows the strategy followed. In a first step, the target NF has to be imaged up to the electrode. This is done in A without voltage bias to avoid any instabilities which would be caused by the metal-metal contact. Then, once the target NF is identified the tip is positioned at the desired location and V_G is swept to give the transfer characteristic in B. V_D is chosen small enough such that the transistor operates in the linear regime. Before extracting μ_L, two important points can be discussed. It can be seen in B that the transfer characteristic does not suffer from contact resistance effects. If it was the case, then the absolute slope on the linear scale, $\left|\frac{\partial I_D}{\partial V_G}\right|$, would decrease at high negative V_G which is not the case in Figure 7- 12. Another transistor

parameter commonly reported is the threshold voltage V_T, defined as the intersection of the transfer characteristic with zero current. From Figure 7- 12, we obtain a value of -2 V $\pm$ 1 V which has to be corrected to -4 V $\pm$ 1 V[22]. These results are close to zero as expected for an ideal transistor. Based on this good matching, we can conclude that the NFs do not suffer from oxygen and water contamination (as expected from our home-made glove box) which are known to move V_T toward positive V_G and that the NFs are hole and electron traps free which are known to move V_T towards negative and positive V_G respectively[8].

Finally, the mobility is obtained by fitting $\mu_L = \frac{L}{WC_0V_D} . \frac{\partial I_D}{\partial V_G}$ from the slope of the transfer characteristic. The measurement was repeated on about ten different isolated NFs and led to a mean value of μ_L =0.07$\pm$0.03 cm^{2}V^{-1}s^{-1}. Using the equation $v = \mu . E$ between the electric field E and the speed v, it is possible to calculate that the time for a hole to move between two adjacent polymer chains stacked in the length of the NF is about 0.1 ns.

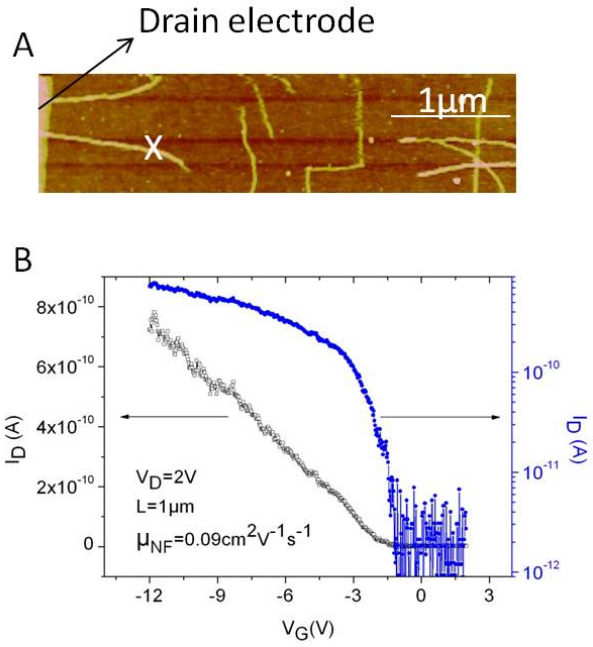

Figure 7- 12 Mobility measurement on one single P34T NF. A: topography map showing one isolated NF connected to the drain electrode at the left extremity. B: transfer characteristic from which the mobility is fitted on the point labeled X on A.

There have been several papers reporting that the longitudinal mobility on films of NFs[23] and web of NFs[2] is not influenced by the alkyl side chain length. The same question arises for one single NF. To our knowledge, there are no reports on isolated P34T NF and only two reports on P3HT NF: one from Merlo et. al[3] (0.06 cm^{2}V^{-1}s^{-1}) and one very recent by Shimomura et. al[4] (0.05 cm^{2}V^{-1}s^{-1}). We see that our mobility

value for P34T (0.07 $cm^2 V^{-1} s^{-1}$) is very comparable to these P3HT values. This is a suggestion that μ_L is alkyl chain length independent for one single NF.

In chapter III, we have measured the mobility for a web of P34T NFs using the standard macroscopic techniques (channel length: 40 µm and channel width: 10 mm) in such a way that the extracted mobility is influenced by the transport within individual NFs but also by the bridging of NFs. We found a web mobility $\mu_{WEB} = 0.059 \pm 0.007$ $cm^2 V^{-1} s^{-1}$ (for a surface coverage of 9%), remarkably close to literature values 0.04 ± 0.02 $cm^2 V^{-1} s^{-1}$ [2,3,4] and, more importantly, comparable to our measurement on one single NF $\mu_L = 0.07 \pm 0.03$ $cm^2 V^{-1} s^{-1}$. This is a second proof (the first being the equation (3) obtained in paragraph 7.2.3.) that transport at the intersection of several NFs does not reduce or limit the charge transport process in a NFs network.

7.3.2. Transversal mobility, μ_T

To investigate charge transport along the height of one NF, we used the sandwich geometry depicted in Figure 7- 13. The NFs were drop-cast and gently N_2 flushed on a conducting substrate. We have chosen Pt for its low roughness (< 1 nm) and the fact that its work function (~ 5.6 eV) is close to the highest occupied molecular orbital of P34T (~ 5.3 eV). Since the NFs are deposited on a metal and the NFs surface coverage is low, measurements in the imaging mode (mapping at constant voltage) would lead to metal-metal contacts and consequently to shortcut currents which are orders of magnitude out of range, making the amplifier saturated and the images unstable. Consequently, measurements are forbidden in the imaging mode and restricted to the spectroscopic mode. In order to get reproducible and non-destructive measurements, we follow an appropriate strategy. Firstly, we acquire several successive topography maps at zero bias until the images are very stable. Secondly, we zoom in successively several times until the tip can be positioned on the target NF. Thirdly, the I/V characteristic is recorded. Finally, after zooming out, the same area is imaged and compared with the image before the I/V sweep to check that the NF is not destroyed by the measurement. To check the tip cleanliness, which is critical when investigating soft materials, I/V sweeps on the Pt electrode were regularly done in a short voltage range (+/- 100 mV to limit the current). Tips with a linear I/V response (ohmic behavior) were considered as good and used for the NFs while tips with other responses were disregarded.

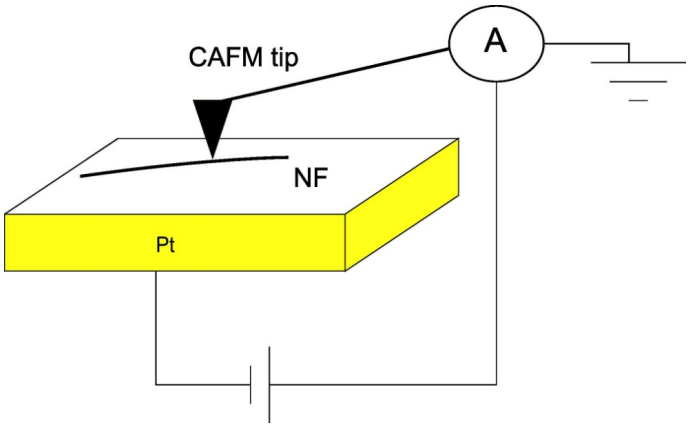

Figure 7- 13 Sandwich structure for measuring transversal mobility, μ_T

A typical I/V curve obtained on a single P3BT (=P34T) NF is shown in Figure 7- 14. Due to the high work function of tip and bottom electrode, we can rule out electron current and consider our device as hole only. Diode characteristics on conjugated polymer are usually associated with space-charge limited current (SCLC) transport[24] and fitted by the Mott-Gurney law[25,26]: $J_{planar} = \frac{9}{8}\epsilon_r\epsilon_0\mu_{T,V}\frac{V^2}{h^3}$ where J is the current density, ϵ_r (=3) is the relative dielectric permittivity of the active layer, ε_0 is the permittivity of free space, V is the applied voltage, and h is the NF height. Usually, a Poole-Frenkel form is used to take into account the field dependence of the mobility $\mu_{T,V}(V) = \mu_T e^{0.89\gamma(V/h)^{0.5}}$ (4) where μ_T is the zero field mobility, γ is proportional to the field dependence of the mobility. These equations are valid for devices with two plane electrodes where the field lines are perpendicular to the electrodes. For CAFM measurements, the geometry is much different at the tip sample contact and it leads to a current density significantly higher close to the tip. Reid et. al[27] have shown that the use of the standard above equations on CAFM data causes a mobility overestimation by up to three orders of magnitude depending on the ratio of the tip contact diameter, d , to the sample thickness, h. They propose the following correction: $\frac{J_{CAFM}}{J_{planar}} = \frac{8}{9}\alpha\delta(\frac{h}{d})^{1.6\pm0.1}$ (5) where α= 8.2 and $\delta = 7.8 \pm 1$. In our case, h = 4 nm and d= 4 nm which gives a correction factor of about 57.

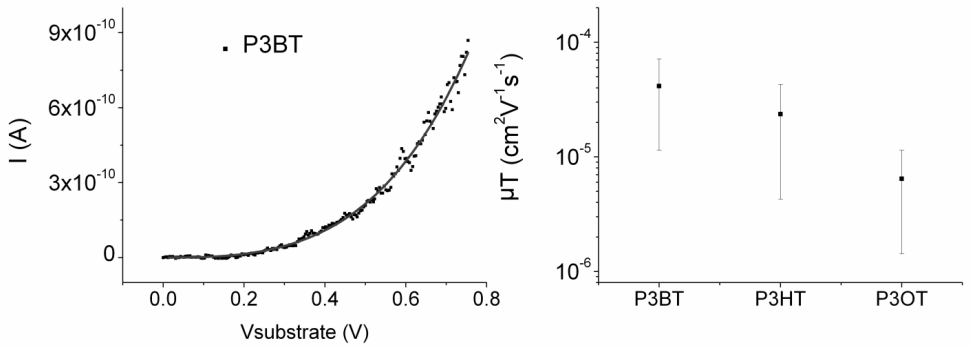

Figure 7- 14 Typical transversal I/V curve obtained on single P3BT NF (dots: experimental points, line: fit to equation (5)) and the transversal mobility for P3BT (=P34T), P3HT (=P36T) and P3OT (=P38T) NFs.

We have performed measurements on isolated NFs of P3BT, P3HT and P3OT (at least ten independent NFs of each) and fitted the I/V curves to equation (5). However, the classic way to prove indisputably the SCLC character of the transport is to check that the current scales as $\propto {}^{1}/_{L^{1.4}}$ (or $\propto {}^{1}/_{L^{3}}$for the planar device). Unfortunately, we cannot tune our sample thickness since the NF's height is fixed. Irrespective of the polymer, we find a typical value for γ of $\sim$ 1X10^{-4} m$^{1/2}$V$^{-1/2}$ which is of the same order of magnitude as for reported values on conjugated polymers studied with CAFM[27,28]. On the other hand, we have found a remarkable dependence for μ_T with the alkyl side chain length as observed on Figure 7-14. As explained elsewhere, the NFs thickness is found to be alkyl chain length independent and therefore is not responsible for the variability of μ_T. The transversal mobility μ_T is found to decrease with the number of carbon atoms on the side chain. This suggests that longer alkyl chains reduce the efficiency of charge hopping from polymer chain to polymer chain. This statement is only valid if the NFs are oriented with the alkyl chain direction perpendicular to the substrate like depicted in Figure 7- 9. A detailed structural characterization of the NFs concluded that all of the polymer NFs strongly orient with the alkyl chain direction perpendicular to the substrate[5]. Moreover, the passivation of SiO_2 with HMDS is known to promote the same orientation. Then, we argue that the big majority of NFs segments orient like in Figure 7- 9 even if we cannot rule out that locally on some spots the NFs are slightly twisted or turned. To our opinion, a better accuracy than one order of magnitude on μ_T seems difficult to reach because important factors like the contact force and contact diameter which have shown to play a crucial role[29] are hard to control or evaluate. In particular, the contact force has tendency to increase while scanning the sample probably due to tip voltage induced contact forces.

7.3.3. Charge carrier anisotropy in one NF

To our knowledge, charge transport investigation along the NF height is reported here for the first time. It is interesting to see that μ_L is three to four orders of magnitude higher than μ_T , see Table 3, even if the applied field is much bigger for the transversal configuration[30] which is known to increase the mobility. This was expected since it is known that the fiber direction is a fast charge transport direction (through the π-orbital's overlap) while the alkyl side chain direction is much slower. Another difference

between μ_L and μ_T is that, while μ_L has been suggested in a previous section to be alkyl side chain length independent, it has been clearly measured that μ_T decreases as the number of carbon atoms on the side chain is increased.

	μ_L	μ_T
Value ($cm^2 V^{-1} s^{-1}$)	10^{-2}	$10^{-6} – 10^{-5}$
Effect of side chain length	No	Yes
Implication for devices	μ_L and J_{max} known ➔Interesting for design	$\mu_T \neq 0$ ➔Presence of transversal current

Table 3 Some salient points about longitudinal and transversal mobilities on isolated nanofibers.

From a technological point of view, we consider that the knowledge of μ_L and J_{max} is interesting for applications engineers to decide whether the NFs can be used or not as interconnecting wires in molecular electronics. It is also valuable to point out that, even if small, μ_T is not zero and therefore this has to be taken into account when designing devices architectures where transversal current in NFs is undesired.

7.4. Technical details

All the CAFM measurements were performed in the home-made glovebox with oxygen concentration lower than 50 ppm and water concentration lower than 10 ppm.

CAFM Transistor and longitudinal mobility: We used the OFETs substrates described in chapter II (HMDS treated SiO_2 dielectric) with thin drain and source electrodes (10 nm Pt layer on top of a 2 nm Ti adhesion layer) to reduce NFs disruption or damage. Only P34T nanofibers were measured (see chapter I for material parameters). The P34T NFs were drop cast on the substrate and then the remaining solvent (o-chlorotoluene) was gently N_2 flushed.

Signal to noise ratio was optimized with a scan rate around 0.25 Hz. CAFM is done in contact mode with a low contact force (~0.3 nN, deduced from force-curve measurements) to avoid any degradation of the soft polymer NFs. Assuming Young's modulus of ~1 GPa for P34T[31], a tip radius of 25 nm (typical for CAFM tip) and using the Hertz mechanic model[32], we find a contact radius of ~2 nm. When taking current measurements, two verifications were routinely done. Suppose that we measure a stable positive current map for a positive drain voltage, V_D, and negative gate voltage, V_G. Firstly, we check that the current becomes zero when turning V_D to zero and keeping V_G negative. If not, it means the measured current is a leakage current reaching the gate electrode and the sample is disregarded. Secondly, we check that the current increases (decreases) when decreasing (increasing) V_G and keeping V_D constant. If not, it means the gate electrode is not well contacted.

Transversal mobility: Measurements were performed on P34T, P36T and P38T nanofibers with the same material parameters as in chapter I except for P36T (regioregularity: 94%, polydispersity: 1.95, number-average molecular weight 23.6 kg mol^{-1}).

Photolithography: 1/spin-coating photoresist futurex NR7-1000P at 3000 rpm for 40 s. 2/baking 150 °C for 60 s. 3/ UV exposition for 36 s. 4/ baking 100 °C for 60 s. 5/development for 10 s in RD6. 6/ Rinse in deionized water plus drying with N_2 gun. 7/ Etching of unprotected Au by HNO_3:HCl (1:3) for 5-10 s. 8/ rinse in deionized water. 9/Etching of Ti by H_2SO_4:H_2O_2 (50:1) at 120 °C for 5-10 s. 10/ rinse in deionized water. 11/ Removal of resine with acetone. For some samples, Au was replaced by Pt. Etching of Pt by HNO_3:HCl:H_20 (1:3:4) at 95 °C for 1 min.

---

[1] J.A. Merlo et al., *J. Phys. Chem. B* **2004**, 108, 19169-19179.
[2] S. Samitsu et al., *Macromolecules* **2010**, 43, 7891-7894.
[3] J.A. Merlo et al., *J. Polym. Sci., Part B: Polym. Phys*. **2003**, 41, 2674.
[4] T. Shimomura et al., *Phys. Rev. B* **2011**, 83, 115314.
[5] W.D. Oosterbaan et al., *J. Mater. Chem.* **2009**, 19, 5424-5435.
[6] L.H. Jimison et al., *Adv. Mater.* **2009**, 21, 1568-1572.
[7] A. Salleo, *Materials Today* **2007**, 10, 3, 38-45.
[8] J.-C. Bolsée, J.V. Manca, *Synth. Met.* **2011**, 161, 789-793.
[9] C. Tanase et al., *Org. Elec.* **2003**, 4, 33-37.
[10] A. Salleo et al., *Phys. Rev. B* **2004**, 70, 115311.
[11] M.A. Laughton and D.F. Warne, Electrical engineer 's reference book, 16th edition.
[12] Using the Hertz model, tip broadening can be written as $x = 2\sqrt{h(2R-h)}$. With $h = 4$ nm (NF height) and $R = 25$ nm (tip radius), we find $x = 25$ nm. Since true NF width is $\sim$20 nm, we obtain a geometric width of 45 nm with CAFM.
[13] T.W. Kellie et al., *J. Vac. Sci. Technol. B* **2000**, 18(2), 632-635.
[14] G.A. O'Brien et al., *J. Mater. Chem.* **2006**, 16, 3237-3241.
[15] L. Burgi et al., *J. Appl. Phys.* **2003**, 94, 9, 6129-6137.
[16] M. Brinkmann et al., *Adv. Mater*. **2006,** 18, 860-863.
[17] M. Brinkmann et al., *Macromolecules*, **2009,** 42, 1125-1130.
[18] M.J. Lee et al., *Adv. Funct. Mater.* **2011,** 21, 932-940.
[19] R. Zhang et al., *J. Am. Chem. Soc.* **2006**, 128, 3480-3481.
[20] In the etching mode, the resist is placed on top of the metal and an etching liquid (most often an acid) etches the unprotected metal from the top; This is in opposition with the lift-off mode where the resist is placed under the metal and the resist (and the metal on it) is lifted off by acetone.
[21] A photoresist is a polymer dissolved in a solvent which contains a photoactive molecule making it sensitive to UV light. There are two classes of photoresist: positive and negative. UV illuminated zones of positive resist are soluble in developer. For negative resist, UV illuminated zone are insoluble while non illuminated parts are soluble in the developer.
[22] For a standard p-type transistor, the source and drain voltages are zero and negative. For our measurements, the source and drain voltages are zero and positive (2 V in Figure 7- 12). In order to compare properly the data, we have to shift all our voltage by subtracting 2 V: our source and drain voltage are negative (-2 V) and zero. Consequently, the transfer characteristics of Figure 7- 12 have to be shifted to the left (negative values) by 2 V and V_T = -4 V $\pm$ 1 V.
[23] W.D. Oosterbaan et al., *Adv. Funct. Mater*. **2010**, 20, 792.
[24] P.W.M. Blom et al., *Appl. Phys. Lett.* **1996**, 68, 23.
[25] M.A. Lampert et al., Current injection in solids (Academic, New York, **1970**).
[26] N.F. Mott et al., Electronic processes in ionic crystals, Oxford university press, London, **1948**.
[27] O.G. Reid et al., *Nano letters* **2008**, 8, 6, 1602-1609.

[28] H.-N. Lin et al., *Appl. Phys. Lett.* **2002**, 81, 14, 2572.
[29] W. Frammelsberger et al., *Appl. Surf. Sci.* **2007**, 253, 3615-3626.
[30] For longitudinal configuration: E$\sim 10^6$ V m^{-1}. For transversal configuration: E$\sim 10^8$ V m^{-1}
[31] S. Miyauchi et al., *J. Appl. Polym. Sci.* **2002**, 85 (7), 1429-1433.
[32] According to the Hertz model, the contact radius r is given by $r^3 = 3FR/4E$ with 1/E= $(1-\nu_1^2)/E_1 + (1-\nu_2^2)/E_2$ where F is the load, R is the tip radius and E is the Young's modulus. With $E_1 = 195$ GPa,$\nu_1 = 0.38$ for $PtIr_5$ and $E_1 = 1$ GPa, $\nu_2 = 0.35$ for polymer, r is found to be around 2 nm.

Measuring everything is utopian, then scientists start reasoning

Chapter VIII: Microstructure-charge transport relationship in P3*A*Ts

In this chapter, we compile all the charge transport measurements performed in this thesis on poly(3-alkylthiophene)s (P3*A*T)s at the macroscopic and nano scales. Going from one single nanofiber (NF) to semicrystalline thin films, we try to draw a picture of charge transport in P3*A*Ts at different length scales. The different morphological factors influencing the in-plane mobility will be highlighted.

Exactly like we did in the introduction of chapter III, we can separate the investigated samples in two model systems:

1. **Films or webs of nanofibers (model system 1)**. The layers are prepared from nanofiber dispersions as explained in chapter I. Each P3*A*T has its own solvent, see Table 2 in chapter I. By changing the dispersion concentration, we have studied webs and films of nanofibers. For these films, the crystallization occurs mainly before deposition.
   ➔**no influence of dielectric surface, deposition technique and alkyl side chain length.**
2. **Chlorobenzene processed films (model system 2)**. The layers are prepared from molecularly dissolved polymer solutions (in this case we use chlorobenzene (CB) as the good dissolving solvent for P3*A*Ts). For these films, the crystallization occurs during the film deposition.
   ➔**influence of dielectric surface, deposition technique and alkyl side chain length.**

It has become clear in chapter III that samples obtained from nanofiber dispersions are insensitive to the surface dielectric, deposition technique and to the length of the alkyl side chain (for convenience Figure 3-10 is reproduced in Figure 8- 1).

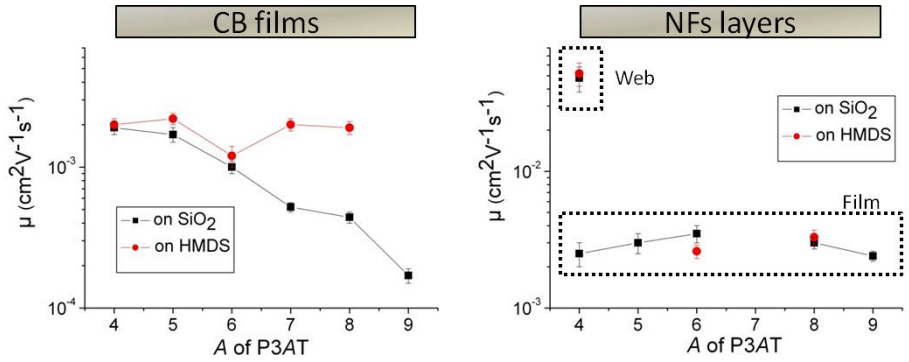

Figure 8- 1 Layers prepared from CB solutions are sensitive to surface dielectric, deposition technique and side chain length while layers from NF dispersions are not sensitive to surface dielectric, deposition technique and side chain length, *A*.

The reason is that, since the nanofibers crystallize in the dispersion (hence before film formation), when they are deposited on the substrate their orientation is hardly influenced by the type of dielectric, technique of deposition (spin-coating or drop casting) or the length of alkyl side chains. The situation is completely different for samples obtained from chlorobenzene solution. The chlorobenzene processed films are sensitive to the type of surface dielectric and the length of side chains, the reason being that the crystallization occurs during (and not before) the film deposition and then the orientation of the polymer chains can be influenced by external factors such as the dielectric surface and side chain length. In other words, casting from NF dispersions offers an accurate control on the in-plane mobility. This point is very important as it is known from literature that many factors influence the mobility (see introduction chapter III).

8.1. Models for samples from nanofiber dispersions (model system 1)

8.1.1. Model for one single nanofiber

In chapter VII, we succeeded in measuring the longitudinal mobility in one single P34T nanofiber: $\mu_L = 0.07 \pm 0.03$ cm^2 V^{-1} s^{-1}. The question is to know what can be deduced from this value on the internal structure of one NF.

From device modeling and low temperature measurements of chapter IV, we have extracted for a web of P34T NFs that the mobility in crystalline regions μ_0 is 1.35 cm^2 V^{-1} s^{-1}. This result is supported by Wang et al.[1] who found a similar value for P3HT (=P36T) spin-coated thin films (around 1 cm^{2}V^{-1}s^{-1}, see Table 1). Thus, there is more than one order of magnitude difference between the nanofiber mobility and the crystalline mobility extracted from device modeling. Moreover, using the acoustic deformation potential theory[2], calculations for a perfect P3HT single crystal led to a mobility ($\mu_{crys} = 31$ cm^2 V^{-1} s^{-1})[3] which is almost three orders of magnitude higher than the nanofiber mobility. How can we understand the differences between the mobilities obtained from measurements, device modeling and theoretical calculations (all compiled in Table 1)?

To address this question, comparison with PBTTT[4], one of the best-performing conjugated polymers, might be useful. When deposited on self-assembled monolayers such as octyltrichlorosilane (OTS) and heated into the liquid crystalline regime, PBTTT thin films reach mobilities[5, 6] up to 0.7-1 $cm^2 V^{-1} s^{-1}$ which is largely better than the best-performing P3HT thin films (see Table 1). In order to understand the origin for the mobilities difference between PBTTT and P3HT thin films, Wang et al.[1] have thoroughly investigated their charge transport properties using the mobility edge model. They concluded that the difference of performance between PBTTT and P3HT thin films is not due to a lower trap density for PBTTT film (both films have the same trap distribution and trap concentration) but instead the difference is due to a much higher crystalline mobility for PBTTT films. They obtained, see Table 1 again, from device modeling that the crystalline mobility μ_0 for PBTTT is comparable to the calculated value for a perfect PBTTT crystal μ_{crys} while for P3HT there is more than one order of magnitude difference between μ_0 and μ_{crys}. It means that crystallites present in thin films of PBTTT are similar to perfect crystals; this is due to the high rigidity of the polymer backbone and the dense side-chain interdigitation which allow for a perfect 3D ordering[1]. On the other hand, the side chain density in P3HT is too high to permit interdigitation which prevents 3D ordering. Therefore, perfect P3HT crystals are not likely to occur in real P3HT thin films but they are expected to contain sliding and tilting defects. For instance, density functional theory calculations on crystal structure of P3HT have suggested that a likely structural disorder is one in which one of the polymer backbones within a lamella runs in the direction opposite to the majority[7].

	μ from measurements [$cm^2 V^{-1} s^{-1}$]	μ_0 from device modeling [$cm^2 V^{-1} s^{-1}$]	μ_{crys} from calculations in perfect crystal [$cm^2 V^{-1} s^{-1}$]
P3HT	0.07-0.1[8]	1.35[9] ~ 1.2[1]	31[3]
PBTTT	0.7-1[5, 6]	~ 20[1]	16[3]

Table 1 Mobilities from measurements, device modeling and theoretical calculations for two of the best performing conjugated polymers: P3HT and PBTTT.

The message from the above discussion is that P3HT layers do not contain perfectly ordered crystals but rather what we will call pseudo-crystals (or pseudo-crystallites) with a mobility μ_0 around 1.3 $cm^2 V^{-1} s^{-1}$ as read in Table 1. This value is still one order of magnitude higher than the mobility of one NF. This comparison suggests that one NF cannot be seen as one single crystallite but instead could be a superposition along its length of pseudo-crystals separated by disordered regions, called intra-fiber grain boundaries, containing a lot of defects like chain disruptions (see Figure 8- 2).

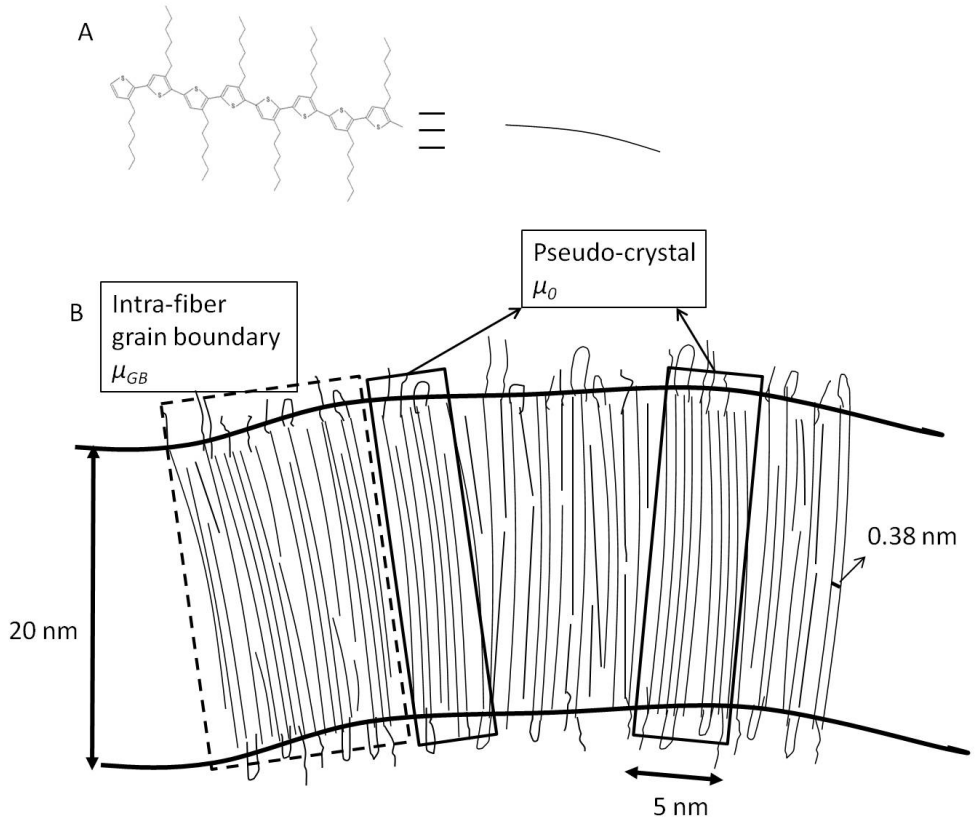

Figure 8- 2 A: Top view of a polymer chain is symbolized by a curve. B: Top view model of one NF (see Figure 1-8) being the superposition of pseudo-crystals separated by disordered intra-fiber grain boundaries. As discussed below, NFs are composed of folded chains and loose polymer chains.

The transport through one NF (unit length L_{NF}) is a serial combination of transport through crystalline domains of length L_{crys} (mobility μ_0) and intra-fiber grain boundaries (mobility μ_{GB}) of length L_{GB}:

$$\frac{1}{\mu_L} = \frac{1}{\mu_0} \cdot \frac{L_{crys}}{L_{NF}} + \frac{1}{\mu_{GB}} \cdot \frac{L_{GB}}{L_{NF}} \quad (1)$$

$$L_{NF} = L_{crys} + L_{GB}$$

What can we deduce on μ_{GB} from this equation? Manipulating equation (1), we obtain:

$$\mu_{GB} = \frac{\mu_0 \mu_L L_{GB}}{\mu_0 L_{NF} - \mu_L L_{crys}} \quad (2)$$

We define $a = L_{crys}/L_{NF}$ as the fraction of one NF made up of the pseudo-crystallites and $1 - a = L_{GB}/L_{NF}$ as the fraction of one NF made up of the intra-fiber grain boundaries. Injecting the mobility values ($\mu_0 = 1.3$ cm^2 V^{-1} s^{-1}, $\mu_L = 0.07$ cm^2 V^{-1} s^{-1}), we get:

$$\mu_{GB} = \frac{0.091 - 0.091a}{1.3 - 0.07a} \quad (3)$$

The characteristic length of one crystalline domain has been suggested to be around 5 nm[10] by XRD experiments. Therefore, we take $L_{crys} \sim$ 5 nm as a good approximation for the typical size of one pseudo-crystal. The size of the intra-fiber grain boundaries is more difficult to evaluate. We can reasonably expect that the grain boundaries are at least 1 nm long since it only corresponds to two to three defects rich polymer chains (they are separated by 0.38 nm, see Figure 8- 2). It implies that a is 83% (5 nm/6 nm) at maximum. Injecting this value in equation (3) gives the following minimum value $\mu_{GB} = 0.012$ cm^2 V^{-1} s^{-1}. On the other hand, finding a maximum value for L_{GB} seems impossible. Therefore, we cannot put maximum border on μ_{GB} (excepted that it must be lower than μ_L) and we have the following range for the mobility of intra-fiber grain boundaries: 0.012 cm^2 V^{-1} s^{-1} $< \mu_{GB} <$ 0.07 cm^2 V^{-1} s^{-1}.

In summary, we retain from this section that one P34T nanofiber might be represented as a serial superposition of pseudo-crystals with mobilities around 1.3 cm^2 V^{-1} s^{-1} and intra-fiber grain boundaries with mobilities higher than 0.012 cm^2 V^{-1} s^{-1}. It is expected that the same conclusion applies for other P3ATs since it was suggested in section 7.3.1.3. that mobilities in single nanofibers are not alkyl chain length dependent and since a similar value of μ_0 for P34T and P36T (see Table 1) was found.

8.1.2. Model for a web of nanofibers at low surface coverage

In chapter III, the mobility of a web of P34T nanofibers with a surface coverage of 9% was calculated to be $\mu_{WEB} = 0.059 \pm 0.007$ cm^2 V^{-1} s^{-1} which is very comparable to one fiber mobility $\mu_L = 0.07 \pm 0.03$ cm^2 V^{-1} s^{-1} measured in chapter VII. This equality was confirmed in chapter VII where we found that the electrical resistance associated with the bridging of two NFs is negligible, $R_{bp} < 0.1\, R_{NF}$. As discussed in section 7.2.4. and Figure 7-8, NFs intersect in different ways:

T intersection (height 4 nm). The intersection height is therefore the same as the height of one NF. As seen on Figure 7-8, the two NFs face each other leading to fast holes transport.

X intersection (6.5 nm <height <=8 nm). For this kind of intersections, we expect that the NFs are stacked on each others. We argue that the crossing NFs are electrically connected via tie-molecules originating from the polymer backbone. Tie-molecules are loose polymer chains starting from one NF and finishing on another NF, see Figure 8- 3. Many papers in the literature have already reported on the importance of tie-molecules for transport in conjugated polymers[11, 12, 13]. We expect the web of NFs to contain a lot of these tie-molecules because the polydispersity of the polymer chains that make up the NFs is higher than 2 (see chapter I) and thus there is a large variation in the length of the polymer chains, the longest ones being the tie-molecules. A second argument for the presence of tie-molecules comes from a paper of Zhang et. al[14]. They monitored the width of P3HT nanofibers as a function of the weight average molecular weight, M_w. They found a linear trend for 0 kg mol^{-1} < M_w< 10 kg mol^{-1}, which means

that the width of one NF is the length of the polymer chain, followed by a constant NF width (around 30 nm) for 10 kg mol^{-1}< M_w< 20 kg mol^{-1} which means that the polymer chains are folded inside the NFs. Our NFs have a weight average molecular weight $M_w = M_n.PD$ = 44.65 kg mol^{-1} thus situated in the plateau domain indicating that our NFs are composed of folded polymer backbones and loose polymer chains, see Figure 8- 2.

In conclusion, electrically speaking a web of nanofibers at low surface coverage behaves like a nanofiber: $\mu_{WEB} = \mu_L$.

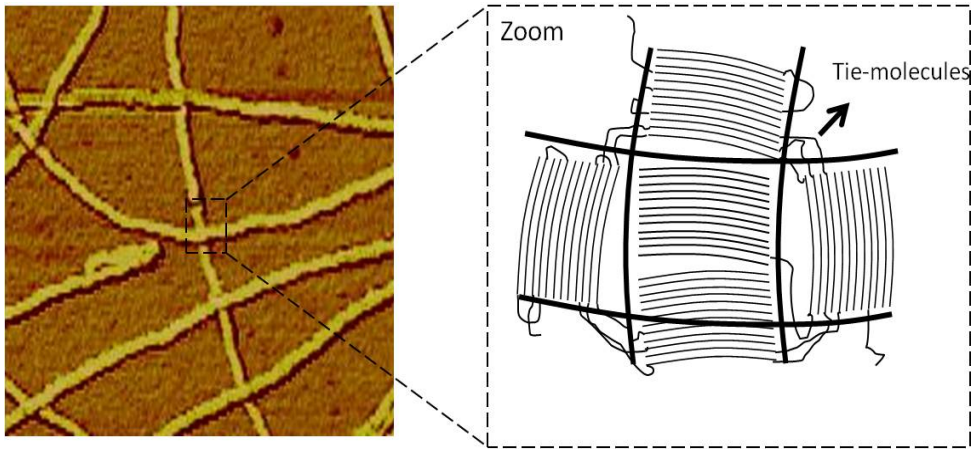

Figure 8- 3 Model for a web of nanofibers: crossing nanofibers are electrically connected by tie-molecules.

8.1.3. Model for a film of nanofibers

We continue exploring the samples casted from nanofiber dispersions. In this section, we discuss the changes occurring in a web of P34T NFs when the surface coverage *SC* is increased until a film of P34T NFs is formed. In chapter III, we found out that a systematic mobility drop occurred when the surface coverage of the web of NFs was progressively increased until a film was formed. This was also perfectly correlated with an increase of the subtreshold swing *SS*, an increase of the offset current and a shift towards positive gate voltage of the onset and threshold voltages. In chapter III, we have explained in details that all these observations are indicative of a larger concentration of holes and electrons trapping in the polymer layer when the *SC* is increased. In chapter VII, we have performed similar measurements on one single nanofiber with the CAFM-transistor. For clarity the subthreshold swing and mobility versus surface coverage curves are reproduced in Figure 8- 4A where the data for one NF are added at zero *SC*. The question is to understand what the origin for these traps is. To answer this question, we have performed low temperature measurements in chapter IV. In the framework of the mobility edge model and using a trap distribution containing one shallow distribution, we found out that the trap distributions are very similar for a web of NFs at low *SC* ($E_{tail} = 50$ meV, $N_{tail} = 6.5$ X 10^{13} cm^{-2}) and a film of NFs ($E_{tail} = 55$ meV, $N_{tail} = 4$ X 10^{13} cm^{-2}). This result is in contradiction with our conclusion that the concentrations of holes and electrons traps are higher at large *SC*. But, as shown by

Chang et al.[15] and as discussed in the end of chapter IV, the subthreshold voltage behavior is better explained by the inclusion of a deep trap states distribution. Unfortunately, our data are not accurate enough (due to the use of a DC source in place of a pulsed source) to fit properly a bimodal (shallow and deep) trap distribution. Therefore, we argue that a film of NFs must contain a larger deep trap distribution than the web of NFs. This is schematically depicted in Figure 8- 4B.

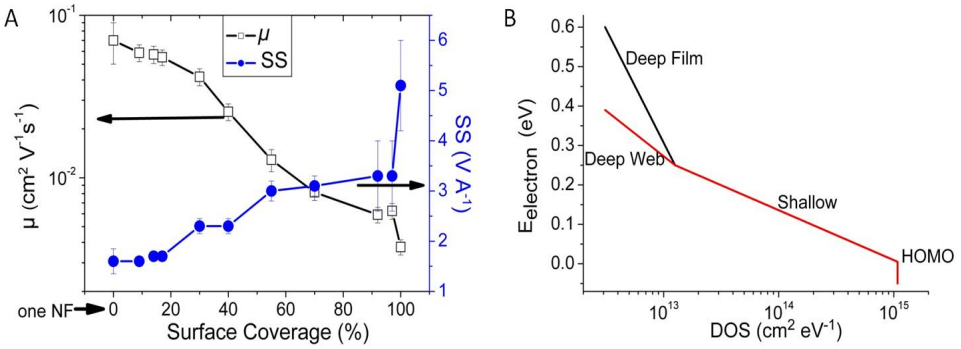

Figure 8- 4 A: The subthreshold swing is increased while the mobility is reduced when the surface coverage is increased. B: Representation of trap states: film and web of NFs have a common shallow distribution while the deep distribution is larger for the film explaining the larger subthreshold swing for the film of NFs than for the web.

Now, we discuss the morphological origin for these traps. First of all, a noteworthy observation is that working with AFM images on webs of NFs offers the crucial opportunity to probe directly the buried interface at which conduction occurs. This is not the case with ordinary thin films (typical thickness is a few tens of nm) for which AFM images do not allow to visualize the holes transporting interface.

This being said, we recall that the field-effect mobility is a two-dimensional variable and consequently is influenced by the transport along NFs but also between NFs. We have seen in section 8.1.2. that crossing NFs do not reduce the charge mobilities but we observe on the AFM phase images at high *SC* of Figure 3-12 (and Figure 3-1) that it might happen that NFs are lying almost parallel to each others with a black region existing in-between. From phase images, which are sensitive to the crystallinity degree of the materials, it can be interpreted as amorphous disordered regions or more simply voids. The amorphous polymer would come from the small portion of molecularly dissolved polymer which is initially present in the nanofiber dispersions. We call these regions between parallel lying nanofibers “inter-fiber grain boundaries” in opposition with the “intra-fiber grain boundaries”. We suggest that the amorphous material in these regions causes the higher density of deep trapping at high surface coverage and the subsequent difficulty for holes to move from one nanofiber to another nanofiber when they do not cross. We argue that the tie-molecules from the surrounding NFs are not long enough to connect through the inter-fiber grain boundary, see Figure 8- 5 right. The result is that charge transport through these grain boundaries is very slow which causes the mobility drop observed in Figure 8- 4A. Finally, we note that this section was done on P34T. However, we observe in Figure 3-1 that the AFM images of all P3ATs NFs show adjacent nanofibers being parallel to each others. Therefore, it is

expected that all the P3*A*Ts NFs films suffer from the inter-fiber grain boundaries (which is supported by Figure 3-2 where the mobility for NFs films was *A* independent).

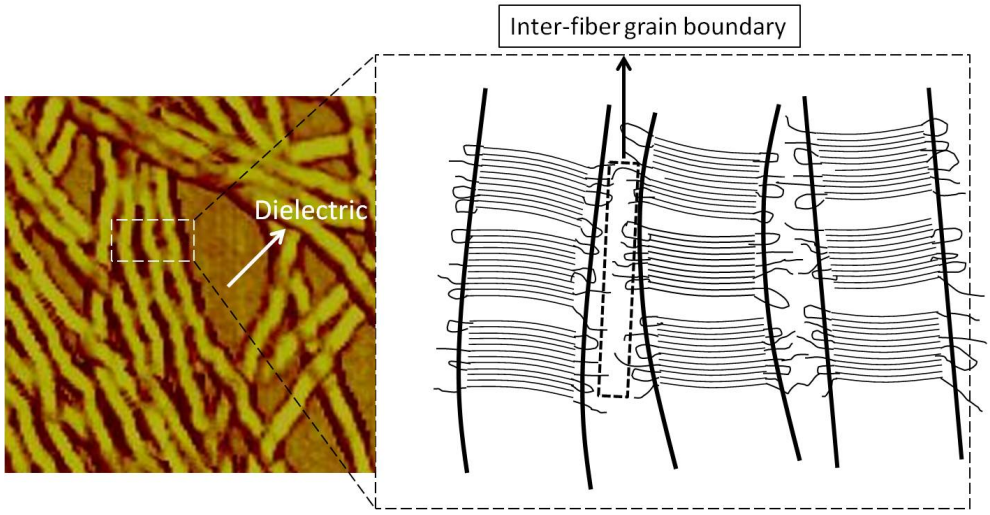

Figure 8- 5 Model for a film of NFs. Inter-fiber grain boundaries present in the regions between two parallel nanofibers are suggested to be the origin of deep traps limiting the charge transport.

8.2. Model for samples from molecularly dissolved solutions (model system 2)

Now, we discuss the charge transport in chlorobenzene (CB) processed P3*A*Ts thin films (see Figure 3-1). From UV-Vis spectroscopy and TEM diffraction pattern, it has been proven that the films are semicrystalline: crystallites are immersed in an amorphous matrix[16]. The crystallites crystallize in the same basic packing as the nanofibers (see Figure 1-8). As explained in chapter III, the crystallites have a strong preference for one of two orientations with respect to the substrate: "face-on" and "edge-on" orientations as depicted in Figure 8- 6B. We have seen in Figure 3-1 that the AFM phase images at the buried and air interfaces are very similar: they are almost featureless; in best cases some short and narrow nanofibers appear. For convenience, the zoomed image for the P39T buried interface is reproduced in Figure 8- 6C. AFM phase mode is sensitive to sample mechanical response and therefore allows to distinguish regions with different degrees of crystallinity. From these images, the length scale of a crystalline domain is estimated to be around 10-20 nm. In Figure 8- 6D, we propose a simple qualitative model for the charge transport in these films. Contrary to what happens for the layers casted from the nanofiber dispersions, we have no information about the relative orientation of two adjacent crystallites. We define β as the in-plane angle between two adjacent grains. Since there are no preferential in-plane orientations between the grains, we assume that large and small β exist (see Figure 8- 6D). Our picture shows also that there is a large variation for the average thiophene tilt angle: $<\alpha>$ is 0° for face-on oriented crystallites and 90° for edge-on oriented ones. As widely and commonly reported

in the literature, transport along the alky side chains is very slow (and this is supporte by the low transversal mobility, 10^{-5}-10^{-6} $cm^2\ V^{-1}\ s^{-1}$, in one single nanofiber measured in chapter VII), therefore transport in the "face-on" grains is very slow. On the other hand, it is commonly known that transport along the π-π stacking direction is fast (as confirmed by the high longitudinal mobility, 7 X 10^{-2} $cm^2\ V^{-1}\ s^{-1}$, in one isolated NF measured in chapter VII), consequently transport in the "edge-on" grains is very efficient. It means that the best performing film will be the one containing the higher proportion of edge-on grains.

In chapter III, we found out for all P3ATs CB processed thin films that there is a huge difference between the mobilities at the air interface (10^{-1} $cm^2\ V^{-1}\ s^{-1}$) and the mobilities at the buried interface (10^{-4}-10^{-3} $cm^2\ V^{-1}\ s^{-1}$). We also measured a higher average thiophene tilt angle $<\alpha>$ at the air interfaces (64.5° - 69°) than at the buried interface (55° - 59.5°). Since the average thiophene tilt angle is a weighted average between the face-on (0°) and edge-on (90°) grains, it means that the polymer interface formed at the air contains a larger percentage of edge-on grains than the polymer interface formed on the SiO_2 dielectric. This is the reason for the three orders of magnitude difference between the mobilities at both interfaces.

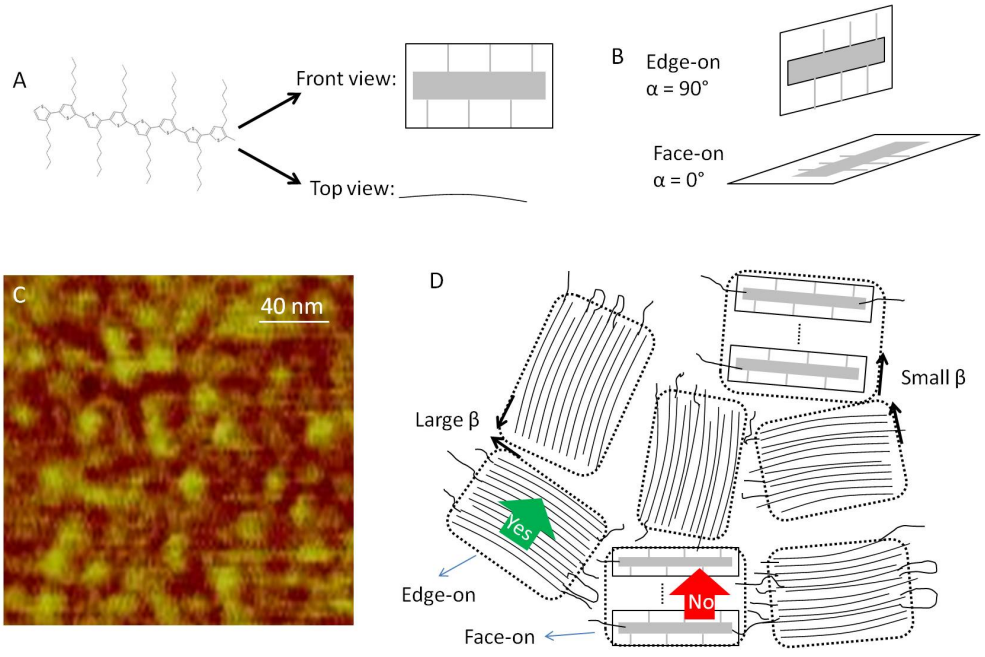

Figure 8- 6 A: Top and front views of a P3HT polymer chain. B: The two preferential crystallites orientations: edge-on and face-on. C: Zoomed AFM phase image on buried face P39T CB film (see Figure 3-1). D: Top view schematic of thin films from chlorobenzene solutions: crystallites are edge-on (fast transport) or face-on (slow transport) oriented. Relative orientation between the grains β is completely random. Note: for clarity, amorphous zones between the crystallites are not represented.

8.3. Conclusion

In this final section, we compile the measurements obtained on the two model systems: those from the nanofiber dispersions (model system 1) and those from molecularly dissolved solutions (i.e. chlorobenzene processed films) (model system 2). Both model systems have their own advantages. Considering one nanofiber like a basic building block, model system 1 allows us to probe charge transport at several length scales: from one isolated NF to a films of NFs via a web of NFs. Polymer layers casted from model system 2 offer the advantage of being very sensitive to the surface on which they are dried (see Figure 8- 7). The polymer chains are dissolved in the solution and therefore they can individually orientate during the film formation. This is not the case for layers formed from nanofiber dispersions. Since they are already crystallized and packed in nanofibers in the dispersion (hence before film formation), the individual chains cannot move independently from each others. In other words, it is more efficient to modify the orientation of individual polymer chains than the orientation of long (typically one µm) nanofibers. Moreover, another difference between both systems is that the grain misorientation angle β approaches zero for one NF (see Figure 8- 2) while β has a larger variation for CB films (see Figure 8- 6). In other words, both model systems offer polymeric layers with two completely different microstructures: a large variation of β and $<\alpha>$ for system 2 and a controlled variation for system 1 (see Table 2). As we will see, comparison between these two model systems will allow us to discuss what are the factors governing the field-effect transport in P3*A*Ts layers.

Figure 8- 7 shows the mobilities obtained throughout the thesis for the two model systems as a function of the alkyl chain length *A* and the surface on which the polymer is casted. We see that the lowest and highest mobilities are achieved for the CB processed films: from 10^{-4} cm^2 V^{-1} s^{-1} for interfaces casted on bare SiO_2 to 10^{-1} cm^2 V^{-1} s^{-1} for all P3*A*Ts polymers casted at the air interface. A strong message of Figure 8- 7 is that the mobility at the air-polymer interface in CB processed films is higher than the longitudinal mobility in one single nanofiber.

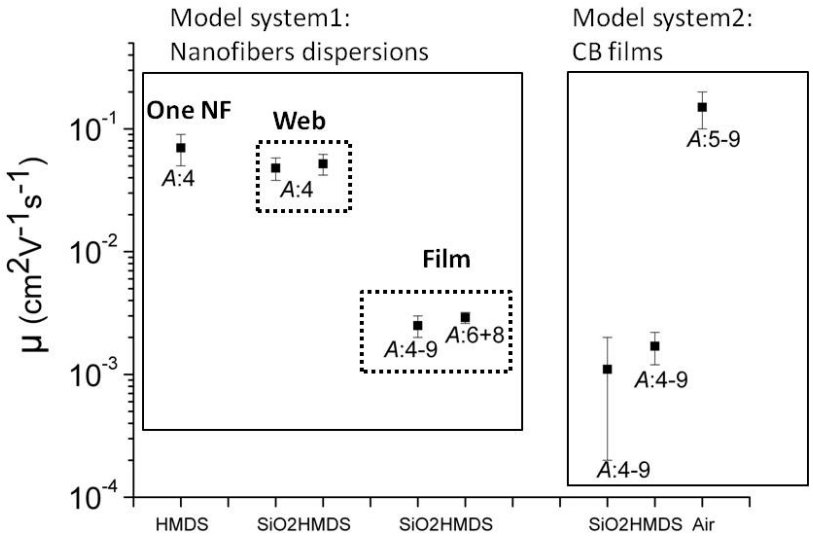

Figure 8- 7 Field-effect mobilities for the two model systems as a function of the dielectric surface and alkyl side chain length. Note: for the web of NFs, the surface coverage is about 17%.

We wrote in the previous section that the average thiophene tilt angle <*α*> explains well the three orders of magnitude difference between both interfaces. It is very interesting to plot the field-effect mobility versus the average thiophene tilt angle obtained by NEXAFS (see Figure 8- 8). The trend is remarkable: the mobility is larger if the average thiophene tilt angle is increased. We remind that a high tilt angle means that the polymer chains at the interface are in average strongly edge-on oriented (see Figure 8- 6). It suggests that a crucial factor governing in-plane charge transport is the orientation of the polymer chains at the dielectric interface. The ability of air to promote edge-on orientation is due to the fact that air is superhydrophobic. The inset of Figure 8- 8 shows the mobilities for CB P3*A*Ts thin films in function of the water contact angle on which the polymer is dried. Since films are processed in the glovebox, air is N_2 with a water contact angle of 180°. A similar relation between the field-effect mobility of P3HT layers and the polarity of the gate dielectric on which the layers are deposited was already reported[17,18,19].

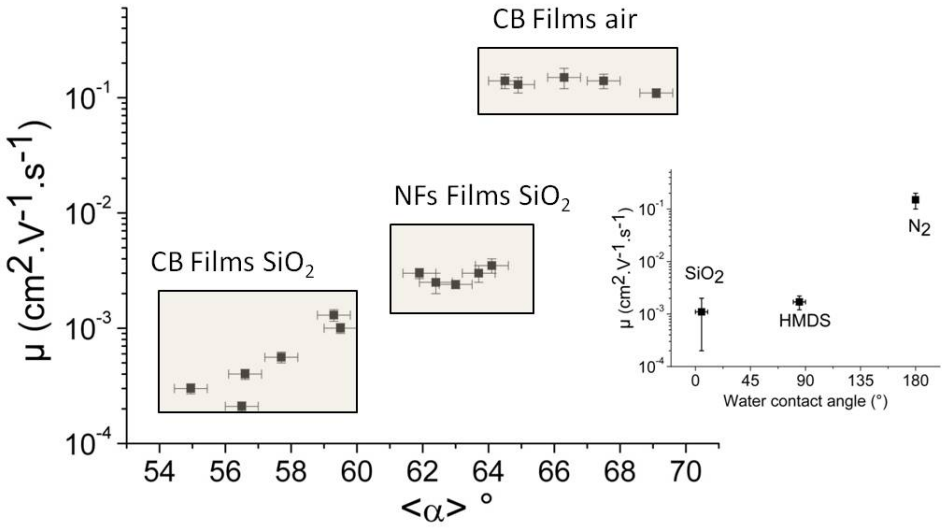

Figure 8- 8 Correlation between the field-effect mobility and the average thiophene tilt angle. Inset shows the mobility versus water contact angle (see Figure 3-8) of the surface on which P3ATs films are casted.

In Figure 8- 8, the average angle for the film of NFs at the SiO_2-polymer interface is displayed. Average angle at the air-polymer interfaces were also measured with NEXAFS. They are not included in Figure 8-8 because the mobilities at these interfaces were not investigated. However, Table 2 shows the average tilt angles for both model systems at both interfaces and the ratio between them. We observe that the ratio between air-polymer and SiO2-polymer interfaces is higher for the CB films (1.17) than for the NFs films (1.03). This observation reinforces the idea that, being self-assembled in dispersions, the chains in the NFs are less attracted by the hydrophobic air than the molecules dissolved in chlorobenzene. Experimentally, it was impossible to measure $<\alpha>$ for one NF or for a web of NFs. However, we expect that $<\alpha>$ for one NF at the SiO_2-polymer interface is comprised between the values reported in Table 2 for NFs films. Indeed, the height of one NF (4 nm) is much smaller than of a film (a few tens of nm) and therefore the orientation at the SiO_2 interface might be influenced by the air interface. Then, $<\alpha>$ for one NF should be around 64°.

	$<\alpha>$ SiO_2-polymer interface	$<\alpha>$ Air-polymer interface	$<\alpha>_{air}/<\alpha>_{SiO_2}$	β
Model system 1: NFs films	61.9° - 64.1°	61.9° - 67.7°	1.03	Small
Model system 2: CB films	55° - 59.5°	64.5° - 69°	1.17	Large

Table 2 Variations of average thiophene tilt angle $<\alpha>$ and grain misorientation angle β are larger for model system 2 than for model system 1.

Now, the last question we address is: What can we deduce from the observation made in Figure 8- 7 that μ at the air-polymer interface is higher than in one NF. A first major difference between the microstructures of one NF and of a CB film is the density of grain boundaries (compare Figure 8- 2 and Figure 8- 6). Then we can conclude that the density of grain boundaries is not a crucial factor determining in-plane charge transport. A second difference concerns the average grain misorientation angle β (see Table 2). It is evident that for one NF β approaches the ideal value of 0° (see Figure 8- 2) while it is very large for CB films (see Figure 8- 6). Based on the observation that μ is larger for air-polymer interfaces than for one NF, it is tempting to conclude that β has zero influence on μ. A second argument which supports this conclusion is: if β had a little bit of influence on the mobility, then we would not observe a three orders of magnitude difference between both interfaces of CB films which have similar β. Then, we conclude that the crucial factor governing in-plane charge transport in P3ATs is the average thiophene tilt angle $<\alpha>$ at the dielectric interface and not the relative misorientation of the grains β nor the density of grain boundaries. However, $<\alpha>$ is certainly not the only predictive parameter for the field-effect mobility. Indeed, NEXAFS is unable to distinguish amorphous from crystalline domains and moreover NEXAFS has a poor lateral resolution so that the output angle $<\alpha>$ is an average. Therefore, it is evident that all the morphological details of complex semi-crystalline polymer films cannot be captured by just one angle. For instance, the abrupt transition by one order of magnitude on Figure 8- 8 at 64.5° is a strong indication that another microstructural parameter influences the mobility.

---

[1] C. Wang et al., *Adv. Mater.* **2010**, 22, 697-701.
[2] N. Karl , in Organic Electronic Materials, edited by R. Farchioni and G. Grosso (Springer, Berlin, **2001**).
[3] J.E. Northrup, *Phys. Rev. B* **2007**, 76, 245202.
[4] M. Heeney et al., *J. Am. Chem. Soc.* **2005**, 127, 1078.
[5] I. McCulloch et al., *Nat. Mater.* **2006**, 5, 328.
[6] B.H. Hamadani et al., *Appl. Phys. Lett.* **2007**, 91, 243512.
[7] W. Xie et al., *Phys. Rev. B* **2011**, 83, 184117.
[8] This is a value frequently reported in the literature, for instance: a) H. Sirringhaus et al., *Nature* **1999**, 40, 685. b) In chapter III of this thesis: for all P3ATs films at the air interface. c) In chapter VII of this thesis: for one P34T nanofiber.
[9] Value for P34T from chapter IV.
[10] T. Shimomura et al., *Phys. Rev. B* **2011**, 83, 115314.
[11] M. Brinkmann et al., *Adv. Mater*. **2006,** 18, 860-863.
[12] M. Brinkmann et al., *Macromolecules* **2009,** 42, 1125-1130.
[13] M.J. Lee et al., *Adv. Funct. Mater.* **2011,** 21, 932-940.
[14] R. Zhang et al., *J. Am. Chem. Soc*. **2006**, 128, 3480-3481.
[15] J.-F. Chang et al., *Phys. Rev. B* **2007**, 76, 205204.
[16] W.D. Oosterbaan et al., *Adv. Funct. Mater*. **2010**, 20, 792-802.
[17] J. Veres et al., *Chem. Mater.* **2004**, 16, 4543.
[18] S. Grecu et al., *Org. Elec.* **2006**, 7, 276.
[19] K. Komatsu et al., *Jpn. J. Appl. Phys.* **2008**, 47, 3196.

Doubt is not a pleasant condition, but certainty is absurd
- Voltaire -

Chapter IX: Summary and outlook

9.1. Summary

The scope of this work was to study the transport of electrical charges (in this case holes in opposition with electrons) in one of the most promising family of organic semiconductors, poly(3-alkylthiophene)s (P3*A*T)s. For this purpose, two kinds of P3*A*Ts layers were investigated: polymer layers (in the form of one nanofiber, a web of NFs and a film of NFs) obtained from nanofiber dispersions (model system 1) and polymer films from molecularly dissolved solution with chlorobenzene as the good dissolving solvent (model system 2).

The key point of our study was that we have performed a multi scale approach: a macroscopic study (from chapter II to chapter IV) and a nanoscale study (from chapter V to chapter VII). Thanks to this multi scale approach, we were able to characterize the electrical mobilities for a broad variety of samples: from one single nanofiber to semi-crystalline thin films. In the following, the most important points achieved in the thesis are presented.

Macroscopic approach (chapters II to IV):

In the macroscopic approach, charge transport in polymer layers was investigated with a standard field-effect transistor (FET) structure. The working principle, device architecture and standard fitting techniques were presented in **chapter II**. Special attention was also paid to the transient effects occurring in a working OFETs. A correction technique to get rid of the detrimental leakage current was developed and proved to be necessary when monitoring the current decay at short time stress. In the second part of chapter II, we also pointed out the detrimental effects of holes and electrons trapping when operating OFETs. We concluded this section by giving a few guidelines in order to reduce these undesired effects as much as possible.

Chapter III showed the importance of the molecular orientation at the interface (obtained with NEXAFS spectroscopy). In particular, a strong correlation between the average thiophene tilt angle and the field-effect mobility was obtained: the more the molecules are edge-on oriented, the better is the holes transport. For instance, we measured a very high mobility $\mu \sim 0.15$ $cm^2 V^{-1} s^{-1}$ for the polymer which was formed at the air interface, the reason being that air is superhydrophobic and consequently promotes edge-on orientation. In the second part of the chapter, we demonstrated that films from model system 2 are very sensitive to the surface dielectric, deposition technique and the alkyl side chain length. Since the polymer chains are completely dissolved in the solution (chlorobenzene is used as the good dissolving solvent for P3*A*Ts), the chains can individually orientate themselves during the film formation and consequently be attracted by hydrophobic surfaces. On the other hand, no influence was found for the layers casted from nanofiber dispersions (model system 1). In this case, the polymer chains are self-

assembled in nanofibers in the solvent (hence before film drying) and consequently the chains cannot orientate individually. In the last part of the chapter, we focus on the differences occurring (in term of mobility, subthreshold voltage, offset current) between a web and a film of NFs (model system 1). We found out that holes and electrons traps impede charge transport when the surface coverage of the NFs is increased. We have suggested that the micro structural origin of the holes and electrons trap comes from the amorphous polymers situated in the regions between two adjacent parallel nanofibers.

Low temperature charge transport measurements between 80 and 380 K were reported in **chapter IV**. All samples exhibited a positive mobility-temperature coefficient ($\partial\mu/\partial T > 0$) and a positive mobility-gate voltage (in absolute value) coefficient ($\partial\mu/\partial|V_G| > 0$), especially at low temperature. The data were analyzed in the framework of the mobility edge model. We have found out that web and film of NFs have a common shallow trap states distribution but we have suggested that the webs have a narrower deep trap states distribution than the film.

Nanoscale approach (chapters V to VII):

The nanoscale approach starts with **chapter V** where we present the SPM (scanning probe microscopy) equipment necessary to investigate organic semiconductors at the nanoscale. Arguments and motivation for the construction of a home-made glovebox are given, followed by a detailed description of the working of the glovebox. Other practical issues like the computation of the leak rate and the estimation of the necessary purging time to reach a defined level of nitrogen are discussed. In the end, we dispose of a glovebox capable of reaching the following contamination levels: [O_2] <50 ppm and [H_2O] <10 ppm.

Chapter VI focuses on Kelvin Probe Force Microscopy (KPFM), a technique capable of measuring surface voltage at the nanoscale (spatial resolution around 100 nm, voltage resolution around a few mV). A complete description of the working principle and measurements on several test samples (voltage difference on external electrodes, solar cell, work function gradient on one sample) introduced the chapter. Then, we tried to visualize holes trapping at the intersection of two NFs and the voltage profile on nanofibers when deposited in a FET structure. Unfortunately, due to the poor lateral resolution and the detrimental dielectric voltage, we were unable to measure properly the nanofibers voltage. We could only detect whether the nanofibers were in the ON state (conducting) or in the OFF state (insulating). Suggestions for the continuation of this work are formulated in the outlook section.

Last but not least, all the results acquired with conductive AFM (CAFM) are presented in **chapter VII**. Probably, one of our most important achievements was the development and characterization of a field-effect transistor where one of the electrodes is the mobile CAFM tip. It enables one to resolve the current distribution within a web of nanofibers and to measure the maximum current density J_{max} inside one nanofiber $J_{max} = 20$ kA cm^{-2}. With the CAFM-transistor, we concluded that the electrical resistance associated with the bridging of two nanofibers is negligible due to a combination of two factors: presence of tie-molecules and interpenetration of the nanofibers. Finally, we focused on the holes transport in one single isolated nanofiber. The longitudinal mobility which is the mobility in the direction of one NF, was measured with the CAFM-transistor, $\mu_L = 0.07$ cm^2 V^{-1} s^{-1} while the transversal

mobility which is the mobility along the height of one NF, was measured in a sandwich configuration, $\mu_T \sim 10^{-5}$-10^{-6} $cm^2 V^{-1} s^{-1}$. Moreover, a decreasing μ_T with increasing side chain length was observed which suggests that longer alkyl chain reduces the efficiency of charge hopping from polymer chain to polymer chain. In the end, we obtain a charge carrier anisotropy in one single nanofiber of four orders of magnitude.

Charge transport model (chapter VIII):

Finally, chapter VIII can be viewed as a summary chapter. Starting from the charge transport data obtained on P3*A*Ts from the macroscopic and nanoscale approaches and from model systems 1 and 2, we propose several simple transport models. Combining the results from both model systems, we conclude with a discussion on the interplay between morphological factors and in-plane charge transport in P3*A*Ts.

9.2. Outlook

Here, we propose some future investigations that could be performed:

Nanofibers alignment:

In order to use the nanofibers in future applications (solar cells, OLEDs, gas sensors, interconnects), it is highly desirable to be able to align the nanofibers parallel to each others. A reported solution in the literature[1] is to apply an AC electric field during the film deposition or on the already dried film to induce an alignment axis. We have tried this technique without any valuable results so far. A second reported technique[2, 3] is called nanorubbing: it consists in rubbing the deposited film with a sharp mechanical tool. We have tried to rub a P3HT film with an AFM tip in contact mode. The top part of Figure 9- 1 is rubbed while the bottom is not. The nanorubbing effect is clearly seen but no evidence of bulk structural improvement has been proved with techniques like transmission electron microscopy or polarized UV/Vis. Maybe a suggestion would be to pattern nanoscale grooves on the substrate before depositing the nanofibers. In this way, the nanofibers would reside inside the grooves and be aligned.

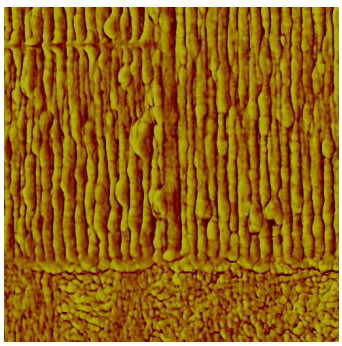

Figure 9- 1 P3HT film nanorubbed with an AFM tip in contact mode

KPFM on nanofibers:

In the section "Visualizing charge transport on nanofibers in OFETs" of chapter VI, we have emphasized on the difficulty of quantifying the voltage profile along nanofibers when biased. At the end of the section, we have suggested a correction technique to remove the undesired effect of the dielectric voltage. It is clear as well that further investigation is required to understand properly the photovoltage observed with KPFM when illuminating the nanofibers + PCBM system. Similar studies have already been done on carbon nanotube + PCBM system[4]. Probably, the knowledge of the KPFM tip work function would be very beneficial and would allow to quantify the voltage shift occurring when the sample is illuminated. Such tip work function calibration is possible with HOPG (highly oriented pyrolytic graphite) samples[5].

Optical characterizations of nanofibers:

At the beginning of the thesis, it was planned to characterize optically the nanofibers. Unfortunately, time and energy were consumed for other techniques and no optical analysis was done. In particular, Fourier Transform Photocurrent Spectroscopy (FTPS) and Photothermal Deflection Spectroscopy (PDS) are highly sensitive optical techniques which can reveal the absorption spectrum in the sub-bandgap region and the electronic density of states. Then, the idea would be to use this optically measured density of states to better interpret the low temperature charge transport measurements where at this moment the shape of the employed density of states is subject to discussion.

Molecular mechanics calculations:

In this thesis, charge transport in conjugated polymers was investigated experimentally. A comparison of our results with molecular mechanics calculations could be very beneficial. In particular, it would be interesting to know if the maximum current, transversal and longitudinal mobility obtained on single P34T NF (see chapter VII) can be predicted or confirmed by theoretical calculations. In collaboration with the University of Mons[6], some molecular mechanics calculations have been performed in order to better understand the crucial relation between field-effect mobilities μ and the average thiophene tilt angle $<\alpha>$. These first results are promising and open the road for further comparisons.

Low T OFET measurement on one NF:

Last but not least: low temperature OFETs measurement on one single nanofiber. This would be the ultimate electrical characterization on the nanofibers samples. The open question is: how does the field-effect mobility of one NF behaves at low T? Is the mobility-temperature coefficient positive ($\partial\mu/\partial T > 0$) or negative ($\partial\mu/\partial T < 0$)? A positive coefficient is typical for organic semiconductors (what we observed in chapter IV) and comes from thermally activated localized transport while a negative coefficient is an indication of band like transport like for inorganic semiconductors. Recently, a negative coefficient has been reported for a solution-processed organic semiconductor (a pentacene derivative)[7].

However, from a technical point of view, this experiment is very challenging. Firstly, the detected current would be very small, especially at low temperature, requiring reliable and stable sub-nA current unit. Secondly, proper contact on one single nanofiber is a recurrent issue. In chapter VII, we have assessed room temperature charge transport in one single nanofiber with the conductive AFM but clearly this solution is not adjustable to low temperature. Probably, e-beam lithography, discussed in chapter VII, is the best candidate to realize reliable contacts on one nanofiber which can withstand low temperature constraints. Thirdly, as already explained in chapter IV, it is highly recommended to use pulsed bias (in place of DC bias) in order to minimize the undesired effects of bias stress which traps holes in the active layer leading to a left shift of the transfer curves.

[1] M. Mas-Torrent et al., *Nanotechnology* **2004**, 15, S265-S269.
[2] G. Derue et al., *Org. Elec.* **2008**, 9, 821-828.
[3] H. Heil et al., *J. Appl. Phys*. **2003**, 93, 3, 1636.
[4] L. Liu et al., *Appl. Phys. Lett.* **2010**, 96, 083302.
[5] C. Kim et al., *J. Kor. Phys. Soc.* **2007**, 47, S417-S421.
[6] W.D. Oosterbaan et al., to be submitted, see Publication list.
[7] T. Sakanoue and H. Sirringhaus, *Nature Materials* **2010**, 9, 736-740.

Curriculum vitae

Jean-Christophe Bolsée

June 2nd 1979	Born in Liège, Belgium
1991-1997	General School Certificate Collège du Sartay, Embourg, Liège
1997-2002	Civil engineer diploma (orientation: physics), ULG Final project : « Heat transfer modelization in a metallic double-wall punched roof" Work realized in collaboration with Arcelor Mittal's research center and ULG.
2002-2006	Test engineer in Centre spatial de Liège ➢ High vacuum, low temperature optical and mechanical tests on ESA Planck Satellite reflectors (primary & secondary) ➢ Development of an optical co-phasing demonstrators
June 2006-2008	Electrical reliability engineer at IMO-IMOMEC ➢ Investigation on reliability and stability of ZnS powder based electroluminescent lamp (Agfa) ➢ Resistivity measurement of metal oxide coating on steel substrate (Flamac) ➢ Mobility measurements in polymer semiconductors (OFETs, starting point of the thesis…)
2008-2011	Phd at Hasselt University, Instituut voor Materiaal Onderzoek (IMO) (FWO-project nanofibers R-1226)

Acknowledgements

Ah Enfin…Here starts the “no rules” part of the thesis: no need to check the spelling, no need to be consequent, no need to be comprehensive, no need to use official, formal and indirect English and most of all I can do something I have ever wanted since I am in IMO: mix French, English and Dutch. Alors allons-y. Let’s start. Laten we beginnen.

First, I want to thank the financial support by het Fonds Wetenschappelijk Onderzoek (FWO, project nanofibers R-1226).

Je pense que tout a commencé quand Jean Manca est entré dans mon bureau et m’a demandé rechtstreeks « Jean-christophe, ben je geïnteresseerd om een thesis te maken ? » A l’époque, aout-septembre 2007, je travaillais en tant qu’ingénieur pour Ward DeCeuninck dans le service « Electrical reliability » et j’avais 28 ans. J’ai beaucoup réfléchi à la proposition : le négatif étant de redevenir, d’un point de vue social, « étudiant » pour quatre ans (même si le travail de recherche n’a rien de celui d’un étudiant), le positif étant de travailler dans un domaine qui m’intéressait déjà beaucoup : l’électronique organique. Natuurlijk ik heb “Ja” gezegd en dit verhaal is begonnen. Jean, Dank u voor de opportuniteit om onderzoek te maken in jouw groep. Je hebt zeker en vast een andere richting gegeven aan mijn professionele leven.

Some colleagues have really influenced this work. Chronologically, the first is Martin Breselge: he taught me the basics for OFETs measurements: how to use the wafer prober, how to interpret the data, how to connect the gate electrode. I remember that he used to take a white sheet of paper, to write the OFETs equation from scratch and to complain that they were all full of empirical parameters and that the mobility is function of almost everything and that the theory for Silicon is much more clean and elegant. I write these lines even if he will never read them. A la même époque, dans une pièce étroite de la cave de l’institut, toi, Olivier, régnais en maître sur le microscope atomique. Je commençais ma thèse et tu allais partir. Je me souviens parfaitement de la période - janvier-février 2008 - où tu étais en partance pour Mons et où j’essayais d’extraire le maximum de ton expertise en AFM. Comment aligner le Laser ? Comment détecter les artefacts ? Comment calibrer le piezo ? C’étaient des chouettes journées coincées dans cette cave minuscule à discuter d’autre chose que de sciences (ou pseudo sciences) : rugby, théâtre, petite vie liégeoise (avec l’accent de Seraing). Ah c’est sûr, partager la même langue ça change tout. Bon maintenant j’attends avec impatience de voir ton monologue de « La Chute » de Camus. Last but not least : Wibren. Zonder twijfel, uw impact op deze thesis is de grootste. Eerst heb jij de nanovezels geprepareerd. Zonder nanovezels, geen metingen, zo simpel is het. Maar uw impact gaat verder. Alle jouw advies tijdens de phd-meeting, jouw correcties, suggesties en opmerkingen op mijn manuscript zijn en waren en groot bron van inspiratie. Ik houd echt van jouw perfectionisme en nauwkeurigheid. Hoewel keer heb ik jouw e-mail gelezen, gelezen en hergelezen zoals een syllabus. « Wat bedoelt hij daar?» « En hier?» «Ah ja goede idee …» « Ik ga dat proberen…» «Ah ja waroom niet…». Dank u Wibren.

Mais IMO c'est aussi beaucoup de collègues avec lesquels on cohabite sans collaboration proche. There are the colleagues from the ONE group : Abay, Donato, Fortunato, Emilie, Hans, Pieter, Bert, Tine, Koen (yooo), Wouter, Wim, Jeroen[2], and sorry for the ones I forget. Sabine jij was een super bureau collega. Ik hield van babbelen over alles en niks, over Fien (Ik moet altijd nadenken voor de juiste uitspraak: het is [FINE] en niet [FIEN] lol) en Arthur. Jij was altijd klaar om computer probleem op te lossen of praktijk problemen in verband met de werkzitting te praten. Ik wens u en Wim de beste. Gopala, you are a very sympathic guy. Chatting with you in the glovebox was always fun. I hope we will see once again in the future. The same for Sathya, the day and night AFM user. You are a very good AFM operator: very accurate, careful and perseverant. Speaking with you about the life and culture in India was always very interesting and full of wisdom. Keep this way Sathya. The Next AFM responsible will be Wouter. We zijn amper twee keer samen op fiets geweest maar genoeg om zich te herinneren. Spreken over fietsen (en natuurlijk over Phil) met u is een beetje zoals spreken over schilderij met Van Gogh. Een super Kenner. Hey man, call me when you want next year for a trip together in the Cauberg. Anyway we will see each other next year in Liège for the first stage of the tour de France and a victory of ….too easy to be said ;o). Jeroen is ook een lid van de nieuwe generatie. Dank u voor jouw super vriendelijkheid, hulp bij computer probleem (bvb mapple die heel nuttig was voor hoofdstuk 4) of voor min arme Engelse. Vincent, 1000 merci pour ta curiosité concernant mon travail et ton aide indispensable avec cette *** de machine qu'est le wire bonder. Je suis venu plusieurs fois en peu de temps t'enquiquiner pour le wire bonder et tu n'as jamais refusé de m'aider. Merci, cela a sauvé mes mesures à basse température. I spent almost one year travelling morning and evening with Paulius. Stay one hour and half in a car with the same person everyday could be terrific, but it was not. We had nice moments solving Rubbik's cube, speaking about papers for APL to your grandmothers…Hey, Have you seen that my phd is over while the bridge is not finished? When do you defend yours? Ik wil ook Johnny bedanken. Eerst voor de continu technische assistentie (bvb de constructie van de glovebox) maar vooral voor de vriendschap tijdens de jaren. De verdeling van onze ervaring wat betreft onze eerst marathon. Ook onze jogging in Bokrijk of langs het kanaal waren mooie momenten. We zien elkaar volgende jaar in Dwars door Hasselt en Grand jogging de Verviers enzovoort.

Finalement, je termine en beauté par mon Amour Marie-Ève. Merci pour ton soutien et amour au quotidien. Je pense que cette thèse s'est passée sans trop de problèmes et que j'ai rarement ramené des sacs à nœuds à démêler à la maison, mais néanmoins tu étais là quand il le fallait. Sans ciment pas de maison. Et puis ne pas oublier le raton Arthur pour son soutien « biberonesque » pendant l'écriture finale du texte.

Abbreviations

AFM: Atomic Force Microscopy

AM: Amplitude Modulation

AO: Atomic Orbital

CAFM: Conductive Atomic Force Microscopy

CB: Chlorobenzene

CB: Conduction Band

CPD: Contact Potential Difference

CS_2: Carbon disulfide

DOS: Density of States

FET: Field-Effect Transistor

FM: Frequency Modulation

FWHM: Full Width at Half Maximum

Ge: Germanium

GPC: Gel Permeation Chromatography

ITO: Indium Tin Oxide

HMDS: Hexamethyldisilazane

HF: Hydrofluoric Acid

HOMO: Highest Occupied Molecular Orbital

KPFM: Kelvin Probe Force Microscopy

LUMO: Lowest Unoccupied Molecular Orbital

MDMO-PPV: Poly(2-methoxy-5-(3'-7'dimethyloctyloxy)-p-phenylenevinylene)

ME: Mobility Edge (for charge transport model)

MO: Molecular Orbital

MTR: Multiple Trapping and Release (for charge transport model)

NEXAFS: Near-Edge X-ray Absorption Fine Structure

NF: Nanofiber

OFET: Organic Field-Effect Transistor

OLED: Organic Light-Emitting Diode

OTS: Octyltrichlorosilane

P3*A*T: Poly(3-alkylthiophene)

P3BT: Poly(3-butylthiophene)

P3HT: Poly(3-hexylthiophene)

P3OT: Poly(3-octyllthiophene)

PBTTT: Poly(2,5-bis(3-alkylthiophen-2-yl)thieno[3,2-b]thiophene)

PCB: Printed Circuit Board

PCBM: (6,6)-phenyl C_{61}-butyric acid methyl ester

PEDOT-PSS: Polystyrenesulfonate doped poly(3,4-ethylenedioxythiophene)

PET: Polyethylene Terephthalate

PPV: Poly(p-phenylene vinylene)

$PtIr_5$: Platinum Iridium

RMS: Root Mean Square

Rpm: Revolutions Per Minute

SAM: Self-Assembled Monolayer

SC: Surface Coverage

SCLC: Space Charge Limited Current

Si: Silicon

SiO_2: Silicon Dioxide

SP: Surface Potential

SPM: Scanning Probe Microscopy

TC: Transfer Characteristic

TM: Tapping Mode

TEM: Transmission Electron Microscopy

UV-Vis: Ultraviolet-Visible

VB: Valence Band

VRH: Variable Range Hopping

XRD: X-ray Diffraction

Nomenclature

a	[m]	Unit cell parameter
A	[1]	Number of carbon atoms on the alkyl side chain
b	[m]	Unit cell parameter
c	[m]	Unit cell parameter
C	[F]	Tip-sample capacitance (for KPFM)
C_0	[F m^{-2}]	Capacitance per unit area
$D_{deep}(E)$	[$cm^{-2}eV^{-1}$]	Distribution of deep trap states in mobility edge model
$D_{tail}(E)$	[$cm^{-2}eV^{-1}$]	Distribution of tail trap states in mobility edge model
e	[C]	Electron charge
E	[V m^{-1}]	Electric field
E	[eV]	Electron energy
E^*	[eV]	Electron energy separating deep and tail distributions
E_F	[eV]	Fermi energy
E_{deep}	[eV]	Width of the deep exponential trap distribution
E_{tail}	[eV]	Width of the tail exponential trap distribution
F	[N]	Electrostatic force
F_{DC}	[N]	Electrostatic force DC component
F_ω	[N]	Electrostatic force at ω
$F_{2\omega}$	[N]	Electrostatic force at 2ω
h	[m]	Nanofiber height
$I_{channel}(x)$	[A]	Current in the channel
I_D	[A]	Drain current
I_{leak}	[A]	Measured leakage current
I_{leak}^{drain}	[A]	Leakage current at the drain electrode
I_{leak}^{source}	[A]	Leakage current at the source electrode
I_{meas}	[A]	Measured current
I_{OFF}	[A]	Current in OFF state
I_{ON}	[A]	Current in ON state
$J_{leak}^{channel}$	[A m^{-1}]	Leakage current per unit length through the channel
J_{max}	[A m^{-2}]	Maximum current density in one nanofiber
k_B	[J K^{-1}]	Boltzmann's constant
L	[m]	Channel length
L_{crys}	[m]	Length of a pseudo-crystal in one nanofiber

L_{GB}	[m]	Length of an intra-fiber grain boundary
L_{NF}	[m]	Nanofiber length
M_n	[kg mol^{-1}]	Number-average molecular weight
M_w	[kg mol^{-1}]	Weight -average molecular weight
N_{tail}	[cm^{-2}]	Total concentration of trap states in mobility edge model
N_{VB}	[cm^{-2}eV^{-1}]	Density of states in the band
n	[1]	Number of moles
n	[cm^{-2}]	Charge carrier concentration
n_{free}	[cm^{-2}]	Concentration of free charges in mobility edge model
n_{total}	[cm^{-2}]	Total concentration of charge
n_{trap}	[cm^{-2}]	Trapped electron concentration in chapter 2
n_{trap}	[cm^{-2}]	Concentration of trapped charges in mobility edge model
$[O_2]$	[1]	Oxygen concentration
P	[N m^{-2}]	Pressure
p_{trap}	[cm^{-2}]	Trapped hole concentration
PD	[1]	Polydispersity
R	[J mol^{-1} K^{-1}]	Gas constant
R_{bp}	[Ω]	Bridging point resistance
R_C	[Ω]	Contact resistance
$R_{Channel}$	[Ω]	Channel resistance
R_{eq}	[Ω]	Equivalent resistance
R_{NF}	[Ω]	Nanofiber resistance
R_{tot}	[Ω]	Total resistance
RR	[%]	Regioregularity
SC	[%]	Surface coverage
SS	[V A^{-1}]	Subthreshold swing
T	[K]	Absolute temperature
T_g	[K]	Glass transition temperature
v	[m s^{-1}]	Speed
V_{AC}	[V]	Alternating current potential (for KPFM)
V_D	[V]	Drain voltage
V_{DC}	[V]	Direct current potential (for KPFM)
V_G	[V]	Gate voltage
V_{onset}	[V]	Onset voltage
V_T	[V]	Threshold voltage
Vol, V	[m^3]	Glovebox volume
W	[m]	Channel width

α	[$m^3\ s^{-1}$]	Nitrogen flow rate
$<\alpha>$	[°]	Average thiophene tilt angle
β	[°]	Grain misorientation angle
ε	[$F\ m^{-1}$]	Permittivity of a material
ε_0	[$F\ m^{-1}$]	Permittivity of vacuum
ε_r	[1]	Relative permittivity of a material
ϕ	[eV]	Work function
μ	[$cm^2\ V^{-1}\ s^{-1}$]	Mobility
μ_0	[$cm^2\ V^{-1}\ s^{-1}$]	Band mobility in mobility edge model
μ_0	[$cm^2\ V^{-1}\ s^{-1}$]	Mobility of a pseudo-crystal in one nanofiber
μ_{crys}	[$cm^2\ V^{-1}\ s^{-1}$]	Theoretical mobility in a perfect crystal
μ_{eff}	[$cm^2\ V^{-1}\ s^{-1}$]	Effective mobility
μ_{GB}	[$cm^2\ V^{-1}\ s^{-1}$]	Mobility in intra-fiber grain boundary
μ_L	[$cm^2\ V^{-1}\ s^{-1}$]	Longitudinal mobility in one nanofiber
μ_n	[$cm^2\ V^{-1}\ s^{-1}$]	Electron mobility
μ_p	[$cm^2\ V^{-1}\ s^{-1}$]	Hole mobility
μ_T	[$cm^2\ V^{-1}\ s^{-1}$]	Transversal mobility in one nanofiber
μ_{WEB}	[$cm^2\ V^{-1}\ s^{-1}$]	Mobility of a web of nanofibers
ν_{ij}	[1]	Hopping transition rate
ξ	[m]	Crystal size (Scherrer length)
ρ	[Ω m]	Resistivity of a material
ω	[s^{-1}]	Resonant frequency